Development of Ash Deposition Prediction Models through the CFD Methods and the Ash Deposition Indice

XIN YANG

A thesis submitted to the University of Sheffield in partial fulfilment of the requirement for the degree of Doctor of Philosophy

Department of Mechanical Engineering
University of Sheffield
Novermber 2016

Declaration

The candidate confirms that the work submitted is his own, except where work which has formed part of jointly authored publications has been included. The contribution of the candidate and the other authors to this work has been explicitly indicated below. The candidate confirms that appropriate credit has been given within the thesis where reference has been made to the work of others.

The work performed in Chapter 4 and Chapter 6 of this thesis has been published in *Fuel* and *Proceedings of the Combustion Institute*, respectively, and the work performed in Chapter 5 of this thesis is accepted for publication in *Fuel*.

I performed all the calculations, developed the ash deposition models and drafted the papers. My supervisors, Prof Lin Ma, Prof Derek Ingham and Prof Mohammed Pourkashanian provided helpful guidance on my research, helped to revise the paper drafts and supported the publication process. Prof Alan Williams helped the proofreading of my first paper published in *Fuel*, Dr Nanda Srinivasan helped to provide the experimental data and the proofreading for my second paper published in *Proceedings of the Combustion Institute*. Also, Prof Hao Zhou helped to provide the experimental information and proofreading for my third paper published in *Fuel*.

All the co-authors have permitted the inclusion of the published papers in the thesis.

Acknowledgements

Foremost, I would like to express my gratitude to my supervisors, Prof Mohamed Pourkashanian, Prof Derek B. Ingham, and Prof Lin Ma for their guidance and support. I thank Prof Mohamed Pourkashanian for offering me the opportunity to undertake this PhD research and his full support on my research. I thank Prof Derek B. Ingham for his suggestions and inspiring me on my research with your patience and profound knowledge. I thank Prof Lin Ma for his advice on guiding my research directions and finding solutions for the difficulties in my research. All of my supervisors have taught me how to undertake research in a scientific and rigorous way. Further, I would like to acknowledge the helps from Dr Janos Szuhanszki, Dr Kris Milkowski, Mr Paul Crosby, Dr Bill Nimmo for the helpful discussions on the deposition probe. I would like to thank Dr Jun Yang for his helpful discussions on my early research. Finally, but not least, I would like to acknowledge other members in our research group for all their assistance throughout my PhD studies.

I wish to thank Prof Alan Williams, from the University of Leeds, Dr Nanda Srinivasan, from the Electric Power Research Institute USA, Prof Hao Zhou, from the Zhejiang University for all their help in my research. Further, I would like to acknowledge Prof James Williamson from Imperial College, London, Prof Roman Weber and Dr A.M. Beckmann from Clausthal University of Technology, and Dr Jaspal Saini from Electric Power Research Institute USA.

I give my gratitude to the financial support from the China Scholarship Council, the University of Sheffield and the University of Leeds for funding my PhD research. I would like to take this opportunity to thank my family and Miss Huimin Wang for all their support and consideration at my hard times.

Publications and presentations from this thesis

Publications in scientific journals

Yang X., Ingham D., Ma L., Williams A., Pourkashanian M. Predicting ash deposition behaviour for co-combustion of palm kernel with coal based on CFD modelling of particle impaction and sticking. Fuel 2016;165:41-9.

Yang X., Ingham D., Ma L., Srinivasan N., Pourkashanian M. Ash deposition propensity of coals/blends combustion in boilers: a modelling analysis based on multi-slagging routes. Proceedings of the Combustion Institute 2017;36(3):3341-50.

Yang X., Ingham D., Ma L., Zhou H., Pourkashanian M. Understanding the ash deposition formation in Zhundong lignite combustion through dynamic CFD modelling analysis. Fuel 2017;194:533-43.

Oral presentations at conferences

Yang X., Ingham D., Ma L., Srinivasan N., Pourkashanian M. Ash deposition propensity of coals/blends combustion in boilers: a modelling analysis based on multi-slagging routes. The 36th International Symposium on Combustion, Seoul, KOREA. 31 July-5 August 2016.

Yang X., Ingham D., Ma L., Zhou H., Pourkashanian M. Understanding the ash deposition formation in a pilot scale furnace: a dynamic CFD modelling analysis. The 11th European Conference on Coal Research and its Applications, Sheffield, UK. 5-7 September 2016.

Abstract

Pulverised coal-fired power generation technologies are important for meeting the electricity consumption worldwide, especially for the developing countries. Changing fuels (coal blending, co-combustion, new fuels, etc.) is common practice in the power stations, which may result in the change of ash deposition behaviours. Ash deposition issues can reduce the heat transfer and have a negative effect on the long-term operation of the combustion systems. Therefore, prediction of ash deposition behaviours is significant for the efficient operation of boilers. In this thesis, new ash deposition prediction models based on particle impaction and sticking behaviours, ash melting behaviour and multi-slagging routes have been developed in order to understand ash deposit formation and predict the slagging propensities through using Computational Fluid Dynamics (CFD) methods and ash deposition indices.

Regarding the CFD methods, an ash deposition model has been proposed to predict the ash deposit formation on an uncooled probe for the co-combustion of South African coal and palm kernel expeller in an entrained flow reactor. A new revised particle impaction sub-model has been developed in order to minimize the numerical related errors without excessive meshing. The molten fraction model obtained from the chemical equilibrium calculations was employed to predict the particle sticking behaviour. The simulation results show that the revised particle impaction model is suitable to accurately resolve particle impaction without using a prohibitive meshing size. Particle impaction and sticking properties dictate the ash deposit formation.

In addition, a CFD-based dynamic ash deposition model has been developed to predict the slagging formation on a cooled probe under high furnace temperatures

of Zhundong lignite (rich in alkali and alkaline earth metal elements) combustion in a pilot-scale furnace. The developed model is based on the inertia impaction, the thermophoresis and the direct alkali vapour condensation and incorporates the influence of the heat transfer rate. The results show that particle deposition from the inertia impaction and the thermophoresis dictates ash deposit formation under high furnace temperatures. The deposition caused by the direct alkali vapour condensation is less significant. As deposition time increases, particle impaction efficiency decreases and sticking efficiency increases due to the thermophoresis and the local temperature conditions. In addition, the ash deposition characteristics are influenced under different furnace temperatures, due to the changes in the particle impaction and sticking behaviours.

Further, a new method for building the ash deposition indice has been proposed to predict the slagging propensities of coals/blends combustion in utility boilers. The method is based on the initial slagging routes and the sintered/slagging route. Two types of initial slagging routes are considered, namely (i) pyrite-induced initial slagging on the furnace wall, and (ii) fouling caused by the alkaline/alkali components condensing in the convection section. In addition, the sintered/slagging route is considered by the liquids temperature, which represents the melting potential of the main ash composition and is calculated using the chemical equilibrium methods. The partial least square regression (PLSR) technique, coupled with a cross validation method, is employed to obtain the correlation for the ash deposition indice. The results obtained show that the developed indice yields a higher success rate in classifying the overall slagging potential in boilers than some of the typical slagging indices. In addition, both SiO_2 and Al_2O_3 can reduce the slagging potential, but the drop in slagging propensity is more significant by adding Al_2O_3 compared to SiO_2.

Contents

List of figures

List of tables

Nomenclature

Abbreviations

AAEM	alkali and alkaline earth metal
ACIRL	Australian Coal Industries Research Laboratories
AFTs	ash fusion temperatures
CCD	charge coupled device
CCS	carbon capture and storage
CCSEM	computer controlled scanning electron microscopy
CFA	chemical fractionation analysis
CFD	computational fluid dynamics
DNS	direct numerical simulation
DPM	discrete phase model
DRW	discrete random walk
EDM	eddy dissipation model
EFR	entrained flow reactor
FEGT	furnace exit gas temperature
FGT	flue gas temperature
FT	flow temperature
GHG	greenhouse gas
GRE	energy-based growth rate
HT	hemisphere temperature
HT-XRD	high temperature X-ray diffraction
IDT	initial deformation temperature
IGCC	integrated gasification combined-cycle
JKR	Johnson–Kendall–Roberts
LT	liquidus temperature
NSI	numerical slagging indice

PKE	palm kernel expeller
PLSR	partial least square regression
RANS	Reynolds Averaged Navier–Stokes
RTE	radiative transfer equation
SAC	South African coal
SS	sintering strength
ST	soften temperature
TGA/DTA	thermal-gravimetric and differential thermal analysis
WSGGM	weighted-sum-of-gray-gases model
XRD	X-ray diffraction
ZD	Zhundong

Roman alphabet

a	absorption coefficient
A	pre-exponential factor, 1/s
$A_{arrival}$	flow flux of the arrival ash particles, kg/(s-m^2)
A_g	specific internal surface area of the char particle, m^2/kg
C_D	drag coefficient
C_L	time scale constant
c_p	specific heat capacity, J/K
c_s	volume concentration
C_{th}	thermophoretic coefficient, kg-m^2/s^2
d_c	diameter of the deposition probe, m
D_h	hydraulic diameter of the flow channel, m
D_m	ratio of the maximum deformation in the particle diameter to the actual particle diameter
D_s	diffusion coefficient, m^2/s
$D_v(T)$	vapour diffusivity at flue gas temperature, m^2/s
E_p	Young's modulus of the particle, kg/(m-s^2)
E_s	Young's modulus of the surface, kg/(m-s^2)
E_x	excess energy , which is the excess rebounding energy

$\overrightarrow{F}$	body force, kg-m/s^2
f	fraction of the heat absorbed by the particles
F_i	impaction correction factor
f^*	predicted value of the centered and normalized dependent variable
$\overrightarrow{F_{th}}$	thermophoretic force, kg-m/s^2
$f_{w,0}$	mass fraction of the initial moisture in the particle
$f_{v,0}$	mass fraction of the initial volatiles in the particle
h	height of the ash sample, m
h_e	the total enthalpy, J/kg
h_{fg}	latent heat, J/kg
h_{oil}	heat transfer coefficient of the cooling oil, W/(m^2-K)
H_r	heat of reaction released by the surface reaction, J/kg
I_d	slagging indice
$I_{coarse,i}$	impaction efficiency from a reasonably coarse mesh,
$I_{fine,i}$	predicted particle impaction efficiency from a well resolved boundary layer,
I_{rad}	radiation intensity, W/sr
$I_{real,i}$	real impaction efficiency
I_v	vapour condensation mass flux, kg/(m^2-s)
K	heat transfer coefficient, W/(m^2-K)
L_{steel}	height, m
MF_i	mass fraction of each particle stream
m	mass, kg
n	refractive index
O_{IP}	overall effect of the interception parameter on the impaction efficiency
p	fluid pressure, Pa
Pr	Prandtl number
p_v	partial pressure of the alkali vapour, Pa
$p_{v,s}$	saturation vapour pressure, Pa
Q_p	latent heat or the heat of reaction, J/s

q_{total}	total heat flux to the wall, W/(m^2)
R	ideal gas constant, 8.314 J/(mol-K)
R_c	overall reaction rate, kg/s
R_{dep}	deposition rate, kg/(m^2-s)
Re_t	Reynolds number (based on deposition tube diameter)
R_i	interception parameter
R_N	viscosity-based slagging indice
(R_{total})	total thermal resistance coefficient, (m^2-k)/W
$\overrightarrow{s'}$	scattering direction vector
s	path length, m
Sc	Schmidt number
Sh	Sherwood number
S_m	momentum source term, N/m^3
$S_{PRESS,h}$	residual sum of squares according to the cross-validation method
S_s	species source term, kg/(m^3-s)
$S_{SS,h}$	residual sum of squares according to all data sets
St	particle Stokes number
S_T	energy source term, W/m^3
T	temperature, K
Tcv	temperature of critical viscosity, K
Ts	initial sintering temperature, K
$\widetilde{u}$	instantaneous gas velocity, m/s
$\overline{u}$	time-mean gas velocity, m/s
u'	fluctuating gas velocity, m/s
V_{liq}	the volume of the liquid phase
V_{solid}	the volume of the solid phase
V_{cr}	critical velocity, m/s
We	particle Weber number
X	volatile fraction

Greek alphabet

α	combustion model
α_c	static contact angle of the particle, (°)
β	viscosity, Pa·s
δ_s	volume fraction of solid phase in the slag
ε_0	initial deposit porosity
$\varepsilon_{deposit}$	deposit porosity
ε_p	emissivity of the particles
ε_t	dissipation rate, J/(kg-s)
η_{ic}	impaction efficiency
η_o	overall impaction efficiency
η_{stick}	sticking efficiency
η_{eff}	effectiveness factor
θ_R	radiation temperature, K
k_i	intrinsic reactivity, kg/s
k	kinetic rate, kg/s
K	effective stiffness parameter
$k_{deposit}$	thermal conductivity of the deposit, W/(m-k)
k_{tke}	turbulent kinetic energy, J/kg
k_{steel}	thermal conductivity of the stainless steel, W/(m-k)
μ	dynamic viscosity, Pa-s
ν_p	Poisson's ratio of the particle
ν_s	Poisson's ratio of the surface
ρ	density, kg/m^3
σ	Stefan–Boltzmann constant, 5.67×10^8 W/(m^2-K^4)
σ_s	scattering coefficient
ς	normally distributed random number
τ	life time of the fluid eddy that the particle is traversing, s
τ_g	fluid thermal conductivity, W/(m-k)
τ_p	particle thermal conductivity, W/(m-k)

$\varnothing$	Thiele modulus
Ω'	solid angle, (^{o})

Subscripts

deposit	deposit properties
g	gas
l	liquid
max	maximum
min	minimum
o	oxidizing atmosphere
p	particle
r	reducing atmosphere
s	slag

Mathematical Symbols

$\nabla \bullet ()$	divergence of a vector field
$\nabla()$	gradient of a scalar field
$\sum_{i=1}^{n}()$	summation operator for the summation of a sequence
$\|\|()\|\|$	matrix norm
$()^{T}$	transpose of a matrix
$\prod_{i=1}^{n}()$	product operator for the product of a sequence

Chapter 1: Introduction

Summary

This chapter introduces the motivation for this research. The status of energy consumption and the coal-fired power generation technologies are discussed in Section 1.1. Ash related problems (including slagging and fouling), which are significant operational constraints in the power plants, are presented in Section 1.2. The formation mechanisms of the ash deposition and its prediction methods are introduced in Sections 1.3 and 1.4. Finally, the aims, novelty and the scope of this thesis are outlined in Section 1.5.

1.1 The role of coal in energy

1.1.1 Energy consumption

Energy is a significant foundation of human resources and social development, and it is the lifeblood of the economy, which promotes the rapid development of human history. In general, as the world population and the world economy continue to expand, there is no doubt that the demand for world energy will continue to increase. Figure 1-1 shows how the world energy usage has been increasing in the last decades, from the BP Statistical Review of World Energy 2016 [1]. Also, The BP Energy Outlook projects that the global energy consumption will rise by 41% by 2035 [2].

According to the Statistical Review shown in Figure 1-1, fossil fuels accounted for 86.0% of the world primary energy consumption by fuel in 2015, and in the UK, they accounted for 81.8%. Fossil fuels, which include coal, natural gas and

oil, are widely employed because of their world-wide availability and high energy density, especially in generating electricity. However, the fractional sum of non-carbon-emitting sources of energies (including the renewable energies, the hydroelectricity and the nuclear energy) only accounted for 14.0% of the world primary energy consumption in 2015. Despite the significant growth in the use of renewable energy, the fraction has remained almost constant during the past two decades as shown in Figure 1-2 [1, 3]. This is because the security, stability and capacity of supply are important issues that need to be considered for the utilisation of these non-carbon-emitting sources of energies [4].

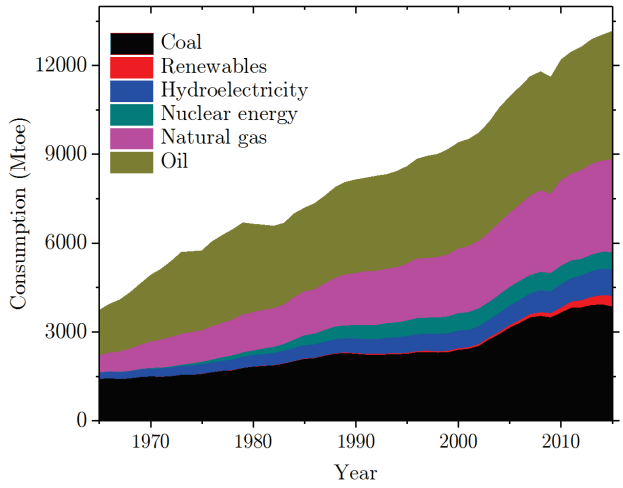

Figure 1-1 World energy usage based on different types of fuel (Million tonnes oil equivalent, Mtoe) [1].

In terms of coal, its share accounted for approximately 29.2% of the total global primary energy in 2015, as shown in Figure 1-2. Also, it should be noted that the global coal consumption decreased by 1.8% in 2015 compared to the 10-year average annual growth rate of 2.9% [1]. This is mainly attributed to the flattening of the Chinese consumption and the reducing consumption in the North America (-12.1%) and Europe & Eurasia (-2.7%) [1]. However, the coal consumption in India showed the world's largest increase from 388.7 Mtoe in 2014 to 407.2 Mtoe in 2015, along with the increased economic and social development in India. In

addition, it should be noted that China, India and the US play the major roles in the world's coal consumption, which accounted for approximately 50.0%, 10.6% and 10.3% of the total world's coal consumption, respectively.

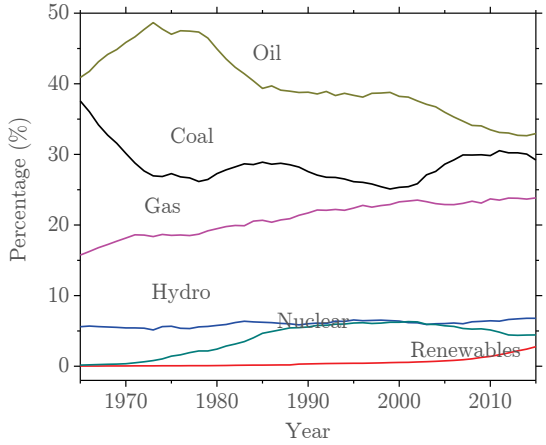

Figure 1-2 Variation in the share of the global primary energy over the last few decades [1].

According to the International Energy Outlook 2016 by the US Energy Information Administration, coal will remain the second largest energy source in the world until 2030 [5]. The World Energy Outlook 2016, by the International Energy Agency, estimates that the world coal demand increases to 5915 Mtce in 2040 under the new policies scenario, which increases by approximately 4.1% of the world coal demand in 2014 [6]. The new policies scenario takes account of the broad policy commitments and plans announced by countries, including national pledges to reduce greenhouse gas (GHG) emissions and plans to phase out fossil-energy subsidies [6, 7]. Therefore, it is irreversible that coal will still be one of the major energy sources worldwide in the near future, especially for the developing countries, although there are the shale revolution in North America and the climate and environmental issues. It should be noted that, currently, Carbon Capture and Storage (CCS) technologies, including the post-combustion carbon capture technology, oxy-combustion and the integrated gasification

combined-cycle (IGCC), are under development worldwide in order to utilise coal in a decarbonising manner [3].

1.1.2 Electricity generation

Coal utilisation mainly consists of two aspects, thermal coal (also referred to as steam coal) and coking coal (also referred to as metallurgical coal). Thermal coal is primarily used for the electricity generation and the production of steam and direct heat; coking coal is primarily used to produce coal coke in steel production [5]. According to International Energy Outlook 2016, 59% of the world coal consumption was used for electricity generation in 2012 [5]. The coal share of the electricity generation was 75% for China and 72% for India in 2012 [5]. Therefore, coal-fired power generation plays a significant role in electricity generation worldwide, especially in developing countries.

Coal-fired power generation technologies mainly include: the grate combustion, the fluidised bed combustion and the pulverised fuel combustion. In the grate firing, air flows upwards though grates and the fuel bed, and the solid fuel is combusted on the grates. The grate combustion requires only minor fuel handling and coal with high moisture and ash content and a varying particle size can be used [8]. However, the utilisation of the grate combustion is limited by its small scale and low energy conversion efficiency of about 20-22% [8]. In terms of the fluidised bed combustion, the solid fuel is suspended by upward-blowing jets of air during the combustion process. This results in a turbulent mixing of gas and solid fuel, which enhances the chemical reactions and heat transfer [8]. An advantage of the fluidised bed combustion is the fuel flexibility. In terms of the pulverised fuel combustion, the solid fuel is finely grounded and pneumatically injected into a furnace through burners. The combustion temperature in pulverised fuel combustion is some 500-600 K higher than that in the fluidised bed combustion [9]. In addition, the particle size is much smaller in the pulverised

fuel combustion (<100μm) than that in the fluidised bed combustion (<2000μm) [9]. Pulverised coal combustion technology has enabled the large-scale electricity production for industries and utilities worldwide. The energy conversion efficiency in a subcritical pulverised coal power plant can reach about 40% when the high quality coal is fired and the efficiency is even possible to reach up to higher than 50% for supercritical/ultra-supercritical steam conditions [8]. Currently, pulverized coal combustion is the most common technology in the world to generate power, accounting for over 90% of the coal-fired capacity [8, 10].

1.2 Ash deposition issues

Ash deposition issues are common problems in the operation of coal-fired boilers. Slagging and fouling, caused by the ash deposition, are the main reasons for boiler unscheduled shutdowns [11]. Generally, ash deposition can be divided into two classes: slagging, which is located in boilers section which has a higher temperature for more melt formation; fouling, which is, however, located on the convective surface that has a lower temperature. The ash deposition not only impedes the efficient heat transfer in the super-heat exchangers and then reduces the overall thermal efficiency of the boiler, but also could harm the stable operation caused by serious slagging [11]. Additionally, the boiler may fall into corrosion risk due to a further consequence of the deposition. All these scenarios result in the reduced boiler efficiency, the reduced availability and the high maintenance costs [12]. On the other hand, the ash deposition properties of the fired solid fuels are important determinants for the boiler design. Slagging is a major factor in determining the size of the boiler furnaces for a given output of steam; fouling dictates the spacing and the location of the tube banks of superheaters and reheaters in the convection section of boilers [9]. In addition, both slagging and fouling determine the placing and operation of the sootblowers in order to maintain the long-term efficient boiler operation. The chemical and

physical properties of the fly ash leaving the furnace are a major determinant in deciding the emission-control systems. Therefore, ash deposition characteristics play a significant role in deciding the fuel selection, the boiler design and the furnace operation [9].

Figure 1-3 shows images of the ash deposits found in boilers [11]. Slagging deposits generate in the hottest sections (radiation sections) and therefore, slagging deposits are partially or completely molten and they have a high sintering degree and dense structure, which results in difficulties in cleaning by sootblowers [11]. However, fouling deposits generate in boilerss where convection is the dominant heat transfer process, rather than radiation [11]. Due to the difference of the flue gas temperature (FGT) in the convection section, fouling deposits can be further divided into the high temperature fouling and the low temperature fouling. High temperature fouling is defined by the partially fused and sintered deposits found in the FGT ranged from 900 ^{o}C to 1300 ^{o}C; the low temperature fouling is defined by the loose and slightly sintered deposits found in the FGT ranging from 300 ^{o}C to 900 ^{o}C [8]. In addition, deposits have a layered structure due to the change of the deposit surface conditions, especially those found in the slagging deposits and the high temperature fouling. For the slagging deposits, the initial layer, which is enriched with Fe species, is caused by the pyrite particle due to its large density and low melting temperature [13, 14]. Also, the small particles and the vapour condensation can be significant factors in determining the formation of the initial ash deposition layer. As a result, the surface temperature of the deposit increases to a point that can facilitate the melting and enhance the sintering to form a slag/sintered layer.

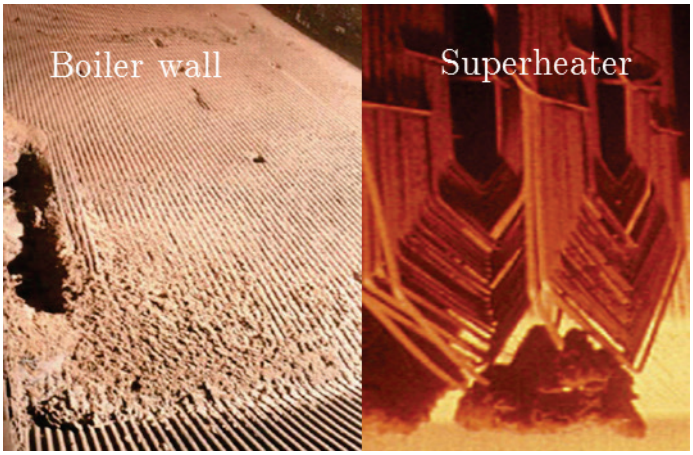

Figure 1-3 Images of deposits found on the boiler wall and the superheater [11].

1.3 Ash deposit formation

1.3.1 Inorganic constituents of coal

Understanding the inorganic constituents of coal is the basis in understanding and predicting the ash deposition behaviours since the inorganic constituents dictate the ash properties (ash fusion, ash sintering and ash viscosity). The inorganic constituents in coal are commonly given as oxides of the relevant metals by employing a standard bulk chemical ash analysis [15]. These inorganic constituents are in the forms of the crystalline and the amorphous phases. Depending on the association of minerals with fuel, the inorganic constituents can be divided into three groups [15, 16]: (i) the discrete mineral particles, (ii) the organically-bound cations, and (iii) the water-soluble salts. The discrete mineral particles can be further divided into (i) the excluded minerals, which are individual mineral grains and (ii) the included minerals, which are inherent in the organic matrix, but not chemically bound with the fuel matrix. Excluded minerals are formed in coal from the extraneous sources during the geologic process or during mining [17]. The main excluded minerals contain silicates (which consist of quartz, kaolinite, illite, muscovite, montmorillonite, etc.), and carbonates (which consist of siderite, calcite, dolomite and ankerite). The

organically-bound inorganics are metals (mainly alkali/alkaline cations) and non-metals (sulphur, phosphorous and chlorine) bound with the organic functional groups (such as chelates and carboxylic acids). The most common metals of the water-soluble salts are alkali/alkaline.

These inorganic constituents experience different chemical and physical transformations during coal combustion, as shown in Figure 1-4 [18]. The excluded minerals may experience a slightly lower temperature than the flame temperature, particle fragmentation, chemical reactions and fusion. Also, the excluded minerals dictate the characteristics of the resultant ash residue [9, 14, 18]. Excluded pyrite plays a significant role in the initial selective slagging on the water wall in the furnace [13]. The included minerals may experience a high flame temperature and a reducing environment and they may undergo a degree of coalescence due to the association with other mineral matter in the coal particles [18]. The coalescence of dissimilar minerals can form the low melting temperature eutectics, such as Fe-Al-Si and Ca-Al-Si eutectic systems, which aggravate the slagging issues [18]. The inorganic constituents in both the organically-bound inorganics and the water-soluble salts may be released into the gas phases and generate the alkali/alkaline vapours, which can cause the fouling issues. On the other hand, the clay minerals are possible to capture the alkali/alkaline metals to reduce their release into the gas phases [19, 20].

Silicates are the most abundant minerals in coal, which account for between 60 and 90 percent of the total minerals in coal [9]. The excluded silicates may undergo phase transformation from the crystalline to the amorphous and form the bottom ash, but they are difficult to generate the melting phase due to their high fusion temperature. On the other hand, the included silicates are possible to react with the basic components related minerals (Fe, Ca, Mg, Na etc.) to generate the low melting point eutectics.

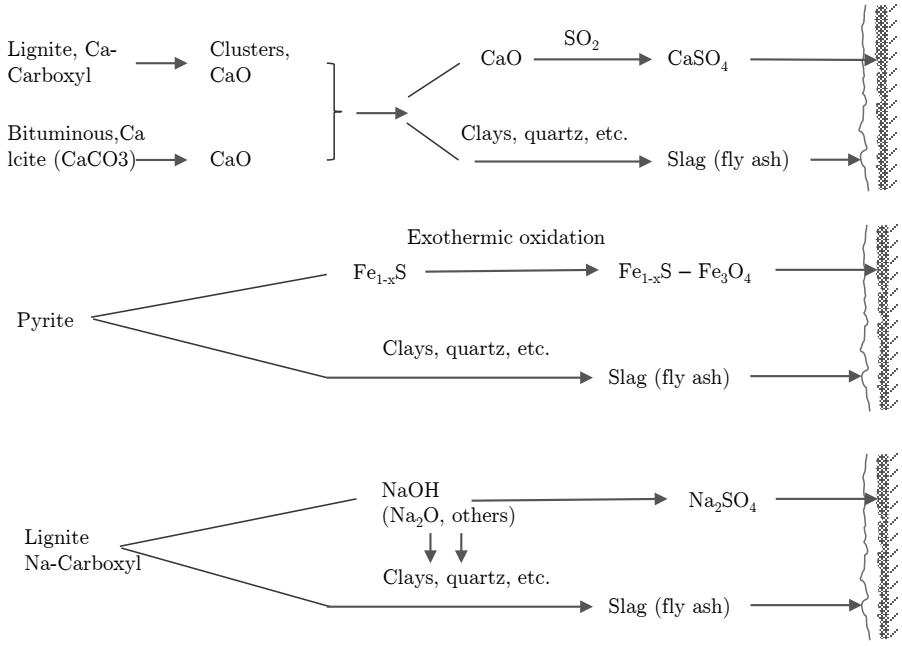

Figure 1-4 The behaviour of the major basic elements in combustion systems [21].

Fe occurs primarily as pyrite for US and UK coals [22]. However, Fe is more likely to occur as siderite and clay minerals for the coals from Australia, South Africa, India and Indonesia [22]. It was found that pyrite (especially the extraneous pyrite) plays a major role in forming the initial slagging layer when burning US coals in boilers [13, 23]. This is because it is easier for pyrite to arrive at the furnace wall surface due to its high density and spherical shape [24, 25]. In addition, pyrite could generate molten phases under lower temperature and under a reducing atmosphere [13, 23]. In terms of siderite, it is possible to react with the silicates to generate the low melting point eutectics, which results in a higher slagging propensity [22].

Alkaline metals (Ca and Mg) occur primarily as (i) calcite and dolomite for bituminous coals, and as (ii) the organically-bound cations for low rank coals [21]. A systematic change from organically bound calcium to calcite is observed with increasing the coal rank [21, 26]. The ash deposition caused by the Ca

constituents can be attributed to (i) the CaO fume, which can react with SO_2 in the gas phase to generate the $CaSO_4$ and form the initial ash deposition layer, and (ii) the Ca-Al-Si eutectics with a low melting point, which can increase the sticking possibility of the ash deposition process.

Alkali metals (Na and Mg) occur primarily as halite, illite, and the organically-bound cations [21, 27]. The organically-bound Na is more likely to occur in lower rank coals [21]. Chlorine content can indicate the fraction of Na content as halite [27]. It is regarded that the halite and the organically-bound Na are more likely to be released into the gas phase and form the alkali vapours, which may either condense on the deposit surface or be partly captured by the silicates [21]. The illite is likely to remain within the silicates and form molten slag phases [21].

1.3.2 Ash properties

1.3.2.1 Ash fusion

Ash fusion is the melting behaviour of coal ash under high temperatures. It is often characterised by the ash fusion temperatures (AFTs) which include the initial deformation temperature (IDT), soften temperature (ST), hemisphere temperature (HT) and flow temperature (FT), as shown in Figure 1-5. The IDT is taken to be when the rounding of the tip of an ash cone, where the ash first melts and may become sticky; the ST is the temperature at which the height of the ash cone equals the width of the ash cone; the HT is when the cone height is half of the cone width; FT is when the ash cone's shape has disappeared and the ash starts to flow [28]. It is regarded that AFTs can indicate the mineral transformation behaviours in boilers. Therefore, using AFTs is a simple method to predict the ash deposition propensities in boilers [28-31]: IDT can indicate the temperature where the slight deposition occurs; ST is the indication of serious slagging on the furnace wall and fouling on the superheater surface; FT shows

the slag with a liquid behaviour. Generally, it is regarded that the higher is the ST, the more difficult is it for the coal to form the ash deposition in boilers.

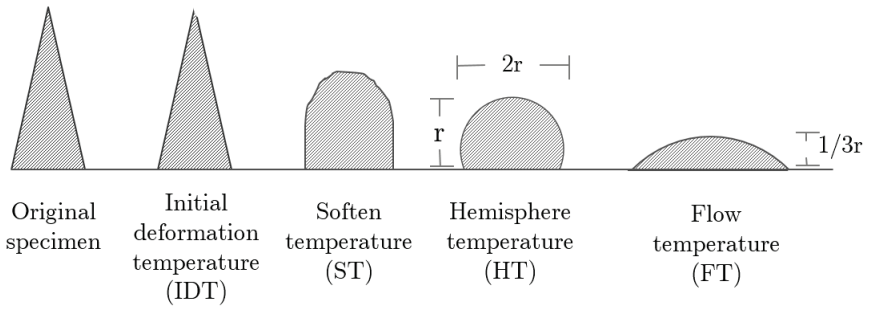

Figure 1-5 Sketch map for the ash fusion temperature test [32].

1.3.2.2 Ash sintering

Ash sintering is commonly employed to describe particle-to-particle agglomeration behaviour under heat treatment, including the strength development and the densification, and the shrinkage of coal ash [33]. Therefore, the ash sintering is significant to understand the strength development of deposits formed in boilers. Since coal ash particles are partly melting and have a viscoelastic state during combustion, it is generally regarded that the diffusion mechanism during coal ash sintering is the viscous flow [34].

It is important to explain the differences between ash sintering and ash fusion. From the aspect of the definition, ash sintering represents the bonding or welding of adjacent particles under the influence of excess surface tension. However, ash fusion represents the melt formation during the mineral transformation. Ash sintering can occur without ash fusion, although ash sintering can be significantly promoted by the ash fusion. Ash sintering and ash fusion often work together to make deposits with a high strength, which increase the difficulty to remove the deposits by sootblowers in boilers.

In addition to investigating the strength development caused by ash sintering, there is a great interest in investigating the onset of the initial sintering. It is

regarded that the IDT can somewhat represent the onset of the initial sintering [28]. However, it is found that there exist large discrepancies in measuring IDT, and this may be as large as 400 °C between the same coal samples [12, 28]. Therefore, using the IDT is inaccurate in identifying the onset of the initial sintering. According to the Frenkel sintering theory, sintering commences with a deformation of the particles and particle-to particle bounding, which can lead to the closure of pores and the contraction of the sintered sample [9, 12, 35]. This can further result in a decrease in both the porosity and the dimension of the sintered sample, and in an increase in the strength of the sintered sample. For coal ash sample, it is often regarded that the initial sintering is attributed to the onset of melt formation [36-38]. In order to accurately measure the onset of the initial sintering, many methods have been developed to investigate the initial sintering temperature (Ts). These methods attempt to measure the physical properties of the coal ash samples that undergo a sudden change, as shown in Figure 1-6. These physical properties include the electrical conductance, the resistance, the compression strength, the rate of displacement of ash pellets, and the pressure drop passing through the ash pellets.

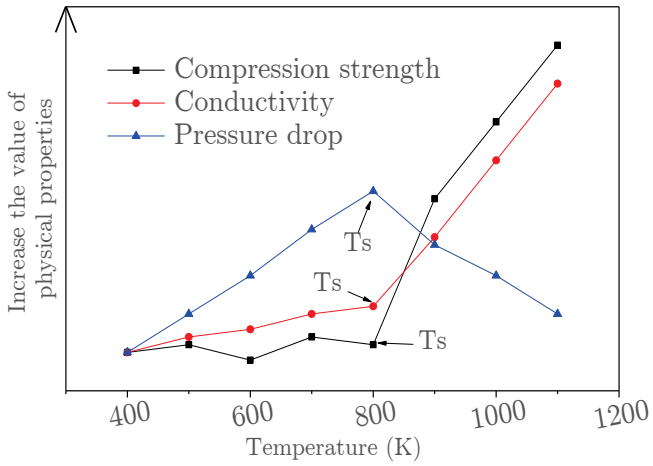

Figure 1-6 Schematic diagram to measure initial sintering temperature (Ts) of coal ashes using the different techniques.

It should be noted that the initial sintering temperature is very significant for fluidized bed combustion/gasification since their operation temperature is close to the initial sintering temperature and much lower than the soften temperature. Therefore, it is regarded that the initial sintering temperature can be employed to estimate the ash deposition propensity and help determine the operation temperature for the fluidized bed combustion/gasification. Currently, it is very interesting to investigate the influence of the ash composition, the gas atmosphere and the pressure on the initial sintering temperature [37-43].

1.3.2.3 Ash viscosity

Ash viscosity is one of the most significant parameters of coal ash under high temperature, which can be employed to determine the operation of the wet-bottom combustor/gasifier and to predict the ash deposition propensity. Generally, the viscosity of coal ash decreases with increasing the temperature. The temperature of the critical viscosity (Tcv) represents the temperature where the viscosity of the coal ash changes on cooling from that of a Newtonian fluid to that of a Bingham p1astic [44], which also corresponds to the temperature where the viscosity abruptly increases on cooling [45], as shown in Figure 1-7. For a wet-bottom combustor/gasifier, there is a suitable viscosity range (ash viscosity cannot be either too high or too low) to operate the reactor in a cost-effective manner [45]. However, for a pulverised coal combustor, it is often regarded that coal ash with lower viscosity may represent a higher slagging propensity. Furthermore, viscosity is a significant parameter to determine the sticking efficiency of the particles after they impact the deposit surface. In terms of the elastic-plastic deformations of the impacting particles and deposit surface, the viscosity of a droplet dictates the extent to which the droplet is deformed on collision, and therefore the contact area of the droplet with the deposit surface is established [46]. The larger the contact area developed during impact, the larger

is the probability that the droplet will stick [46]. Assuming that the droplet does not breakup, the final contact area is expected to decrease with an increase in the viscosity [46].

The viscosity of coal ash under high temperatures is dictated by the coal ash composition. According to the influence of the ash composition on the viscosity, coal ash composition can be divided into three groups [47]: (i) glass formers (e.g. SiO_2); (ii) amphoteric oxides (e.g. Al_2O_3); (iii) modifier oxides (alkali/alkaline oxides and FeO, etc.). It is often regarded that the viscosity is increased with increasing the concentration of glass formers; the viscosity is decreased with increasing the concentration of glass formers; however, the viscosity can be either increased or decreased with increasing the concentration of amphoteric oxides. For coal ash, the viscosity is increased with increasing the concentration of Al_2O_3 because there exist modifier oxides (alkali/alkaline oxides and FeO, etc.) [45].

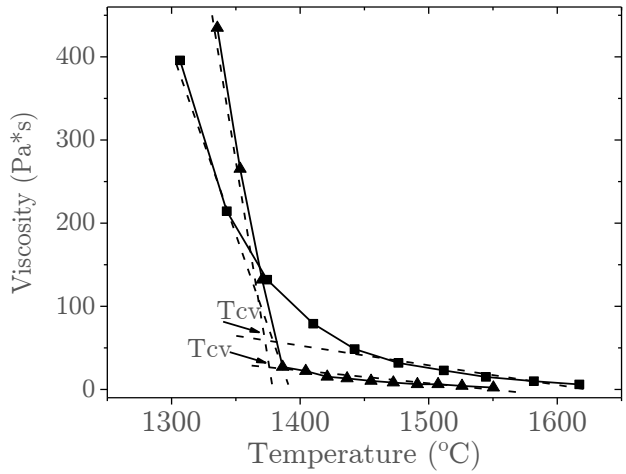

Figure 1-7 Viscosity of coal ash as a function of temperature, Tcv (temperature of the critical viscosity) [48].

Many prediction models have been developed based on the ash composition in order to estimate the viscosity of coal ash since it is very expensive and difficult to experimentally measure the viscosity [45]. Generally, as shown in Table 1-1, these viscosity prediction models can be divided into two groups, (i) models for

completely molten silicates, which are mainly based on the ash composition of the coal ash, and (ii) models for liquid-solid mixtures, which are based on the composition of the liquid phase and the solid phase by using thermodynamic methods. It should be noted that these viscosity prediction models are suitable for silicate as the major ash composition, however they maybe not suitable for solid fuel ash with a high amount of alkali/alkaline metals [49]. Furthermore, it is noted that the viscosity prediction models for completely molten silicates are often employed to estimate the viscosity of the impacting ash particles in CFD based ash deposition models [25, 50]. However, it maybe not suitable to employ these viscosity models for completely molten silicates to estimate the viscosity of the impacting ash particles. This is because the impacting ash particles are probably not completely molten, but liquid-solid mixtures. This is because that their particle temperatures are much lower than the melting point.

Table 1-1[1] Some typical viscosity prediction models of coal ash [45, 51-55].

Viscosity model		Equations	
completely molten	Urbain-model, Kalmanovitch-model	$\beta = C_1 T exp(\frac{10^3 C_2}{T})$	(1-1)
	Watt & Fereday-model	$\log(\beta) = \frac{C_3 \bullet 10^7}{(T-423)^2} + C_4$	(1-2)
liquid-solid mixtures	Einstein-model	$\frac{\beta_s}{\beta_l} = 1 + 2.5 V_{solid}$	(1-3)
	Roscoe-model	$\frac{\beta_s}{\beta_l} = (1 - V_{solid})^{-5/2}$	(1-4)
	Song-model	$\begin{cases} \frac{\beta_s}{\beta_l} = 1 + 1.158 V_{solid} & if\ V_{solid} < 10\% \\ \ln\left(\frac{\beta_s}{\beta_l}\right) = C_5 \bullet \ln\left(1 + \frac{V_{solid}}{0.77}\right) & if\ 10\% \le V_{solid} \le 40\% \end{cases}$	(1-5)

[1] β represents the viscosity, β_s and β_l represents the viscosity of the slag and the liquid phase in the slag, respectively, T represents the temperature (K), C_1, C_2, C_3, C_4 and C_5 represent the coefficients based on the ash composition, and δ_s represents the volume fraction of solid phase in the slag.

1.3.3 Ash deposit formation

Pulverised coal particles are injected with the entrained air from the burner into the flame region of the boiler [12]. The particles heat up (at a rate 10^5-10^6 K/s) and the moisture is evaporated, which is caused by the radiation and mixing with hot gases [12, 56]. After the evaporation, the light gases and tars release (devolatilisation) and these organic species react with oxygen (volatile combustion), followed by the char combustion [57]. Simultaneously, the ionically or organically bound inorganic species (e.g. alkali/alkaline metals, Cl, S, and P) are released into the gas phase and generate the inorganic vapours at the stages of both the devolatilisation and the char combustion [12]. It should be noted that a part of the inorganic vapours may be captured by the SiO_2 and Al_2O_3. The remaining uncaptured inorganic vapours condense on other ash particles and directly condense on the cool deposition surface. The homogeneous nucleation of the inorganic vapours gives rise to the fume particles (aerosols or sub-micron ash particles) [58]. The remaining unvaporised inorganic species undergo a series of overlapping physical and chemical processes (e.g. phase transformations, fragmentation, melting and coalescence), which results in the formation of the larger fly ash compared to the sub-micro ash particles [12, 58]. Therefore, fly ash particles often has a bi-modal particle size distribution [12, 58].

Fly ash particles must be transported to the deposition surfaces in order to generate the ash deposition. Generally, there may be at least five mechanisms of ash particles transferring to the deposition surfaces, namely inertia impaction, thermophoresis, condensation, diffusion and chemical reactions, as shown in Figure 1-8 [59-61]. Inertia impaction and thermophoresis involve the solid particles, whereas the condensation and chemical reactions affect the gas phase. Diffusion can have an effect on the transport of the solid and gaseous phases near the heating surface but have a stronger effect on the movement of the sub-

micrometre particles [59]. On the other hand, deposits formed by diffusion and thermophoresis are evenly distributed around the tube, while the deposit formed, due to inertial impaction, will be formed only on the upstream tube side with a mountain-like-shaped upstream deposit [59].

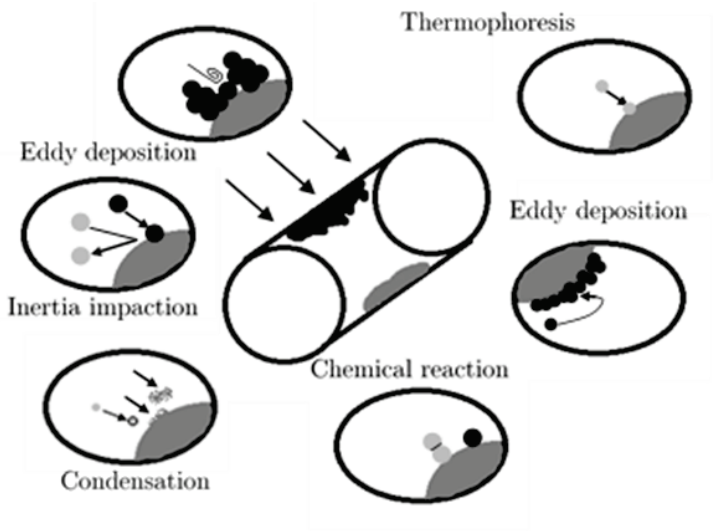

Figure 1-8 Mechanisms of the deposit transport onto the deposit surface [59-61].

The inertial impaction is regarded as the dominant mechanism for the ash deposit formation within boilers [24, 61, 62], especially under conditions with a high deposit surface temperature. The particles impact on the surface only when they have sufficient inertia to traverse the gas stream lines [24]. The impaction efficiency (defined as the possibility of the particle to impact on the surface) is dictated by the particle properties (size and density), gas flow properties (viscosity and velocity), and the target geometry (tube diameter and shape). Generally, the particle Stokes number (defined as the ratio of the characteristic time of a particle to a characteristic time of the flow or of an obstacle) can be employed to describe the particle impaction efficiency. When the particle Stokes number is small, the particle impaction efficiency is very small and close to zero; with a further increase in Stokes number, the particle impaction efficiency sharply increases and eventually approaches unity. In the burner region, where the

temperature is very high, there is little or no condensation of the vapour species, and therefore it is assumed that the inertial impaction is the major pathway [11, 25]. Additionally, the deposition of large fly ash particles is mainly determined by the inertial impaction.

Thermophoresis is a significant mechanism for small particles due to a temperature gradient [59]. The thermophoretic force results from the collision of fluid molecules with higher average kinetic energy on the hot side of the suspended particles to the molecules with lower average kinetic energy on the cold side of the particles [59]. The thermophoretic force acts in the opposite direction of the temperature gradient. Further, thermophoresis is quite significant, especially at the initial deposition stage and this is due to the low deposit surface temperature. With the deposit growth, due to an increase in the deposit surface temperature, the influence of the thermophoresis on the arrival rate of the small particles is decreased.

Condensation is the mechanism by which alkali/alkaline vapours are collected on the deposit surfaces [24]. The condensation rate is dictated by the amount of the metal vapourised species in the coal and the temperature condition in the furnace. Generally, coal with higher concentration of the metal vapourised species is easier to give rise to the condensation and high furnace temperature can enhance the vaporisation ability of the metal species in the coal [24, 59, 63]. This process is key during the initial stages of the deposit formation on the fouling surfaces where temperatures are too low to form the melt. It has been identified that there are three different methods of condensation [24, 59]: (i) The direct heterogeneous condensation of vapour on the deposition surfaces by traverse the boundary layer; (ii) The homogeneous nucleation of vapours resulting in the formation of fume particles and these particles are possible to be deposited on the surface by the thermophoresis; (iii) The vapours condense on other particles in the boundary

layer. Therefore, condensation can be an important fouling mechanism for low rank coals with a high potential for generating large amount of condensable species.

Diffusion is the mechanism of the transport of vapours and small particles towards a solid surface by a local concentration gradient [24, 59]. In the case of Fick's diffusion, molecules move towards a solid surface due to a concentration gradient. On the other hand, it is possible that eddy diffusion drives the small particles to impact at the deposit surface by the turbulent eddies [24].

Chemical reactions involve the heterogeneous reactions of the gas phases with the deposit. The main significant chemical reactions are alkali/alkaline absorption, oxidation and sulphation [24, 59, 64]. They not only increase the mass of the deposit, but also may produce an increase in the strength due to the recrystallization and solidification processes [24, 59].

It should be noted that the latter four mechanisms are regarded as near wall effects and they are less significant compared to the inertial impaction [65-67]. However, thermophoresis is important for small particles at the early stage of the deposit formation when the deposition surface temperature is much lower than the gas temperature in the mainstream. Also, condensation is important for fouling formation in the convection section of boilers.

After being transported to the deposition surfaces, fly ash particles either rebound from the surfaces or stick to the surfaces depending on the sticking efficiency. The sticking efficiency includes the stickiness of both the ash particles and deposition surfaces. The stickiness is determined by the temperature, viscosity, melt fraction, surface tension and kinetic energy. Also, the properties are employed as the threshold criterion for ash particles to be sticky. After the ash particles deposit on the surfaces, the deposits could detach from the surfaces or

build-up on the surfaces. The mechanism of detachment describes the stability of the sticking particles at the surface.

Currently, low-NOx emission reduction methods are often employed in boilers to control the NOx emission level by using low NOx burners. It is regarded that low-NOx burners may increase the furnace slagging because the new design can lead to an increase in local reducing conditions and flame impingement on the rear wall [12, 68]. However, some researchers have found that the retrofitting of low NOx burners may not lead to a detrimental effect on boiler slagging [68]. This is because low NOx burners can reduce the heat flux in the burner belt and the peak flame temperature, which may reduce the slagging problems [68]. Therefore, these two combined effects dictate whether or not the low-NOx burners can aggravate the slagging issue in boilers. The other consideration for the new boiler design is the supercritical and ultra-supercritical steam cycle boilers, which have higher thermal efficiency than subcritical steam cycle boilers. The former boilers have higher surface temperature of the superheaters than the latter boilers (100-200 ^{o}C higher), which may result in a higher melting and sintering behaviour of ash deposition on the superheaters [69].

1.4 Prediction of ash deposit formation

Ash deposition is a significant factor in determining the operation and performance of the combustion processes. This is because the ash deposition not only causes heat transfer inhibition, but also could trigger the unscheduled shutdown of the combustion systems [11, 25]. Therefore, it is necessary to study and predict the ash deposition characteristics when the new fuels are applied, in order to maintain the long-term efficient operation of boilers and reduce the maintenance costs.

The ash deposit formation is very complicated for solid fuel combustion in drop tube furnaces and boilers. The ash deposition is determined according to the temperature-time history of fuel particles, which involves several processes (fuel combustion, heat transfer, particle transportation, particle impaction and sticking, deposit growth, etc.) [11, 65]. CFD is an important simulation technology in resolving the solid fuel combustion in boilers and typically a commercial CFD code (Ansys Fluent) can be employed to deal with these problems [4]. Ansys Fluent employs the finite volume method to discretize the fluid domain enclosed by the combustor into a huge number of cells and solves the transport equations for the mass, momentum and energy balances [4]. The continuum gas phase is solved in an Eulerian frame while the motion of the discrete phase of the coal particles is predicted in the form of a Larganian frame [4, 70]. At the same time, the in-house developed ash deposition models can be incorporated into the software using the User Defined Functions and Memories. On the other hand, for engineering purposes, there is a demand to develop a relative simple and practical method that can quickly and easily predict the ash deposition propensities for engineers without much CFD knowledge. Therefore, it is still significant to develop a reliable ash deposition indice which is useful to understand the ash deposition propensity of the new fuels or fuel blending for boilers.

1.5 Thesis structure

1.5.1 Research aims and novelty

The research aims of this research are as follow:

- To develop ash deposition models through CFD methods to study the particle impaction and sticking behaviour. Therefore, an in-depth understanding and more accurate prediction of the ash deposit formation

process can be obtained. In order to resolve the inaccurate prediction of particle impaction efficiency when a coarse mesh is employed, a sub-model for the particle impaction is to be proposed in the ash deposition model. In addition, a dynamic ash deposition model is to be developed based on the multiple ash deposition mechanisms and incorporating the influence of the heat transfer rate in order to predict the time-dependent ash deposition behaviour.

- To develop a novel approach for building an ash deposition indice in order to improve the prediction of the overall slagging propensity for real boilers. The method is based on the multi-slagging routes in boilers and the ash deposition indice could provide a relative simple and practical strategy to predict the ash deposition propensity through the ash chemistry aspect.

The novelty of this research is as follows:

- A steady state CFD model that simulates particle impaction and sticking has been developed for predicting the ash deposition characteristics on an uncooled deposition probe and the CFD model is validated by the co-combustion of South African coal and palm kernel expeller in an entrained flow reactor. A new revised particle impaction model has been developed and accomplished, using an impaction correction factor, in order to minimize the numerical related errors without excessive meshing.
- A dynamic CFD model, which is based on the inertia impaction, the thermophoresis and the direct alkali vapour condensation and incorporates the influence of the heat transfer rate, has been developed for predicting the ash deposit formation on a cooled deposition probe and the CFD model is validated for the Zhundong lignite in a pilot scale coal-fired furnace.

- A new method to develop the ash deposition indice, which is based on the initial slagging routes and the sintered/slagging route, has been developed and used for predicting the ash deposition propensities of coal combustion in utility boilers supported by the data collected from power stations. The partial least square regression (PLSR) technique, coupled with a cross validation method, is employed to obtain the correlation for the ash deposition indice.

1.5.2 Scope and limitation of the thesis

The first part of the research work in this thesis is mainly focus on predicting the ash deposit formation on an uncooled deposition probe for the co-combustion of South African coal and palm kernel expeller through a steady CFD model. The revised particle impaction model is suitable to deal with the inaccurate particle impaction in a cross flow. The particle sticking model has been developed for the palm kernel expeller. For other types of biomass, calcium, potassium, or silicon may be the major ash components rather than phosphorus, which can lead to the change of the ash chemistry and the particle sticking model. Therefore, the particle sticking model needs further development for the ash deposition model.

The second part of the research work in this thesis is mainly concerned with predicting the time-dependent ash deposit formation process on a cooled deposition probe for lignite combustion through a dynamic CFD model. The depositing particles are assumed to be completely ash particles due to the ash deposition probe is not close to the flame region and therefore the combustion process is not considered in the present model. However, when coal particles are not fully combusted, CFD model needs to include the combustion model to predict the ash deposition behaviour. In addition, this study has employed the typical porosity sub-model and the experimental data to predict the deposit porosity and thermal conductivity. However, it is still needed to validate the

porosity and thermal conductivity prediction model for other fuels. This is because these two deposit properties may be influenced by the ash chemistry when the solid fuels are changed.

The third part of the research work in this thesis takes into consideration developing a method to build an ash deposition indice for real boilers based on multi-slagging routes. Iron and sulphur in US coals are assumed in the form of pyrite. This kind of assumption is suitable for US coals. However, siderite may be the dominant iron-bearing mineral for many other coals, such as South African and Australian coals. In addition, the ash deposition indice is developed through the ash chemistry and the combustion conditions in boilers are not considered. However, the combustion conditions may vary for different boilers, which may affect the slagging propensities. Therefore, it is better to employ the direct mineral information of coal and incorporate the combustion condition in boilers to further develop the model and build an ash deposition indice.

1.5.3 Outline of the thesis

- In Chapter 1, a general introduction to the motivation for the ash deposition prediction is presented. In Chapter 2, a detailed literature review on the ash deposition prediction models is presented, which involves CFD methods and the ash deposition indice.

- In Chapter 3, the experimental facilities and data, which are used in the subsequent chapters, are described.

- Chapter 4 presents the numerical results and discussion on the steady CFD prediction of ash deposition behaviours on an uncooled deposition probe. Also, a detailed introduction of the ash deposition model, which is determined by the revised particle impaction model and particle sticking model, is presented.

- In Chapter 5, the numerical results and discussion on the dynamic CFD-based ash deposition prediction on a cooled deposition probe are presented. A detailed introduction of the ash deposition model, which takes account of the inertia impaction, the thermophoresis and the direct alkali vapour condensation, is presented.

- Chapter 6 presents the numerical results and discussion on the prediction of overall slagging propensities in boilers through the developed ash deposition indice. The developed indice is compared with some of the typical ash deposition indices. In addition, using the ratio SiO_2/Al_2O_3 to predict the melting behaviours and slagging potential is discussed. A detailed introduction of the mathematical model, in order to develop the ash deposition indice, is presented.
- In Chapter 7, the key findings and conclusions are presented and some suggestions for the possible future prospects of this thesis are discussed.

Chapter 2: Literature review

Summary

This chapter reviews key aspects of the prediction methods of ash deposition. The main strategies and challenges in predicting the ash deposition by using the CFD methods and the ash deposition indices are presented. In addition, the current research status of these prediction models is introduced.

2.1 Overview of ash deposition prediction

The predicting ash deposition behaviour is significant in order to optimise the operation of boiler parameters and maintain a long-term operation of boilers when new fuels or coal blends are to be burnt in boilers. Also, an in-depth understanding of the major deposition pathways during the ash deposit formation for a known easy slagging coal is important to provide guidelines for the efficient utilisation of the easy slagging coal. Many methods have been developed to predict and understand the ash deposition behaviour for solid fuel combustions. Generally, they can be divided into two major groups: (i) CFD methods, which predict ash deposition behaviour through calculating the temperature-time history of coal particles in combustors (including particle combustion, particle transportation, particle impaction and particle sticking and rebounding); (ii) ash deposition indices, which are commonly based on the fuel properties (ash fusion, ash sintering, ash viscosity, inorganic constituents, ash content, etc.) to predict the ash deposition behaviour in combustors.

2.2 CFD methods

CFD methods solve the temperature-time history of fuel particles in order to predict the ash deposit formation through determining the arrival rate of particle impacting the deposition surfaces and the sticking efficiency of these arrival particles [11]. Therefore, CFD predictions of ash deposit formation involve [65] calculating the particle trajectories and particle impaction and sticking processes, in addition to solving typical combustion behaviour, such as the gas flow, energy conservation and heat transfer, and combustion (devolatilisation, char combustion, volatile combustion, etc.).

2.2.1 Governing equations

Coal combustion is typically modelled as a dilute two-phase reacting flow [71], which has the following characteristics [72]: (i) the gas phase is the continuous phase and the coal particles are the discrete phase; (ii) the concentration of the discrete phase is dilute which means that fluid-flow in coal combustion belongs to the particle-laden flow.

The Euler and Lagrange methods are often employed to deal with flow field of the gas phase and the solid phase, respectively [71]. Further, the interaction between the gas phase and the solid phase is calculated using the particle-source-in-cell method [70, 71].

The conservative forms of the governing equations of the gas phase are summarised as follows [73]: continuity equation (Equation (2-1)), momentum (Equations (2-2)), energy equation (Equation (2-3)), and species equation (Equation (2-4)).

$$\frac{\partial \rho}{\partial t} + \nabla \bullet (\rho \boldsymbol{u}_i) = 0 \tag{2-1}$$

$$\frac{\partial \rho \boldsymbol{u}_i}{\partial t} + \boldsymbol{\nabla} \bullet \left(\rho \boldsymbol{u}_i \boldsymbol{u}_j\right) = \boldsymbol{\nabla} \bullet (\mu \boldsymbol{\nabla} \boldsymbol{u}_i) - \frac{\partial p}{\partial x_i} + S_{mi} \tag{2-2}$$

$$\frac{\partial \rho h}{\partial t} + \boldsymbol{\nabla} \bullet (\rho \boldsymbol{u} h_e) = \boldsymbol{\nabla} \bullet \left(\frac{\mu}{Pr} \boldsymbol{\nabla} h_e\right) + S_T \tag{2-3}$$

$$\frac{\partial \rho c_s}{\partial t} + \boldsymbol{\nabla} \bullet (\rho c_s \boldsymbol{u}) = \boldsymbol{\nabla} \bullet (D_s \boldsymbol{\nabla} (\rho c_s)) + S_s \tag{2-4}$$

where S_m, S_T and S_s are the momentum, energy and species source terms respectively, D_s is the diffusion coefficient, ρ is the fliud density, c_s is the volume concentration, $\boldsymbol{u}$ is the velocity vector, h_e is the total enthalpy, Pr is Prandtl number, μ is the dynamic viscosity, p and T are the fluid pressure and fluid temperature respectively. Generally, in the above governing equations of the gas phase: the left hand side of the equations are the terms of the rate of change and the convective terms; the right hand side of the equations are the diffusive and the source terms.

The fluid flow in real boilers is dictated by the turbulence. Currently, the Reynolds Averaged Navier–Stokes (RANS) approach, which solves the time-averaged equations of fluid flow by decomposing the instantaneous quantity into time-mean and fluctuating quantities, is the most common practice for predicting the fluid flow in boilers in a steady state [11]. There exist many different turbulence models for RANS, including the Spalart Allmaras model (one-equation model), k-ε model (two-equation model), k-ω model (two-equation model) and Reynolds stress model (seven-equation model). Choosing a suitable turbulence model should be relevant with a detailed analysis of the numerical solvers and the numerical errors associated with them [11]. It is regarded that, in determining the high accurate numerical predictions of a turbulent flow, the quality of the grid and the numerical solver maybe more significant than the RANS model itself [11].

2.2.2 Radiative heat transfer

The radiative heat transfer could account for approximately 90% of the total heat transfer in radiation section of boilers and furnaces [72]. In CFD, the radiation is modelled by dealing with the radiative transfer equation (RTE). For an absorbing, emitting and scattering medium, the RTE at position $\vec{r}$ in the direction $\vec{s}$ is given by [70]:

$$\frac{dI(\vec{r},\vec{s})}{ds} = an^2\frac{\sigma T^4}{\pi} - (a+\sigma_s)I_{rad}(\vec{r},\vec{s}) + \frac{\sigma_s}{4\pi}\int_0^{4\pi} I_{rad}(\vec{r},\vec{s}')\phi(\vec{s}\bullet\vec{s}')\,d\Omega' \qquad (2\text{-}5)$$

where I_{rad} and ϕ are the radiation intensity and phase function, $\vec{s}'$ is the scattering direction vector, s is the path length, a, n and σ_s are the absorption coefficient, refractive index and scattering coefficient respectively, Ω' is the solid angle. As shown in Equation (2-5), the left hand side of the equation is the term for the rate of change of the radiation intensity, which is a function of position and direction; the first term on the right hand side of the equation is the augmentation of radiation intensity due to the in-emission from the medium; the second term on the right hand side of the equation is the attenuation of the radiation intensity due to the out-absorption and out-scattering by the medium; the last term on the right hand side of the equation is the augmentation of the radiation intensity due to the in-scattering from other directions [74]. It is noted that the differention and integration are included in the equation. Hence, it is difficult to directly solve the RTE. Taking into account the computation expense and prediction accuracy, the discrete ordinates method (DO) is often employed to simplify and solve the RTE [70, 71].

The DO model assumes that the RTE can be solved by a finite number of discrete solid angles which are associated with the direction $\vec{s}$ [70]: each octant of the angular space 4π is discretized into $\theta\ divisions \times \varphi\ divisions$ solid angles; and

the integrals over the directions in the Equation (2-5) can be replaced by the numerical quadrature; θ and φ are the polar and azimuthal angles, respectively. Therefore, the integration term in the Equation (2-5) can be approximated by a summation term and the direction number is equal to $8 \times \theta\ divisions \times \varphi\ divisions$ in three-dimensional calculations. Increasing the discretization of $\theta\ divisions$ and $\varphi\ divisions$ will achieve more reliable results. However, this may substantially add to the cost of the computation.

In order to solve the above RTE, the radiation characteristics of the gases are required. The weighted-sum-of-gray-gases model (WSGGM), which assumes the flue gas is composed of a transparent gas and several gray gases [71], is often employed to calculate the radiation characteristics [70]. WSGGM predicts the total gas emissivity based on the temperature dependent polynomials and the absorption coefficient for a particular pressure and path length [57].

2.2.3 Combustion models

Modelling the combustion of coal particles mainly contain four steps, evaporation, devolatilisation, volatile combustion and char combustion. Evaporation refers to the release of moisture in coal particles into the gas phase; Devolatilisation refers to the release of the organic compounds into the gas phase from the volatile in coal particles; Volatile combustion refers to the combustion of the released organic compounds in the gas phases; Char combustion refers to the combustion of coal particles after the evaporation and the devolatilisation. Therefore, in CFD modellings, four different models should be employed to describe the rates of these four steps. Many efforts have been focused on developing a more accurate devolatilisation model, volatile combustion model and char combustion model [57].

2.2.3.1 Devolatilisation

The kinetics and yields of devolatilisation are strongly governed by the temperature history (holding time, heating rate, and peak temperature) [57]. Additionally, the ambient gas composition can affect the devolatilisation.

In the single kinetic rate model, the volatiles are released at the rate that is first-order dependent on the amount of remaining volatiles [75]:

$$Coal \xrightarrow{k} (1-X)residue + Xvolatiles \tag{2-6}$$

$$-\frac{dm_p}{dt} = \mathrm{k}[m_p - (1-f_{v,0})(1-f_{w,0})m_{p,0}] \tag{2-7}$$

$$k = \mathrm{A}e^{-(E/RT_p)} \tag{2-8}$$

where X is the volatile fraction, $m_{p,0}$ and m_p are the initial and current particle mass respectively, $f_{w,0}$ and $f_{v,0}$ are the mass fractions of the initial moisture and volatiles in the particle respectively, k is the kinetic rate, A is the pre-exponential factor, E is the activation energy, R is the the ideal gas constant and T_p is the particle temperature.

2.2.3.2 Char combustion

Char combustion involves the produce of CO and further CO_2 from the reactions of char with oxygen. The kinetic of char combustion is complex. According to the processes in the char combustion, the factors that control the reaction rates can be either the chemical adsorption and desorption or the diffusion. On the other hand, compared to the reaction rate of devolatilisation, that of char combustion is low. In pulverized-fuel flames, the char burn-out time is 1 s and the time for devolatilisation to take place is of the order of 0.1 s [72]. In addition, for typical temperature conditions (greater than about 100K), the char combustion will most likely be under the diffusion limited combustion region and

the intermediate combustion region between the chemically and diffusion limited combustion regions [76].

The Smith's intrinsic model, which is one of the most popular char combustion models, is employed in this study. In the Smith's intrinsic model [70, 77]: the oxygen order of the surface reaction is unity; the overall reaction rate is a function of the particle temperature, chemical reaction rate, surface area and oxygen concentration and diffusivity:

$$R_c = \eta \frac{d_p}{6} \rho_p A_g k_i \tag{2-9}$$

where

$$\eta_{eff} = \frac{3}{\varnothing^2}(\varnothing coth\varnothing - 1) \tag{2-10}$$

$$k_i = A_i e^{-(E_i/RT)} \tag{2-11}$$

Further, R_c, η_{eff} and k_i are the reaction rate, the effectiveness factor and the intrinsic reactivity, respectively, A_g is the specific internal surface area of the char particle, $\varnothing$ is the Thiele modulus which is a function of the effective diffusion coefficient and the density of the oxidant in the bulk gas, and E_i and A_i are the activation energy and the pre-exponential factor, respectively.

2.2.3.3 Volatile combustion

Volatile combustion is dictated by the reaction of volatile products with oxygen to produce gas species (CO, H_2O, and CO_2). Global mechanisms are often employed to represent the reactions during volatile combustion. A two-step reaction of volatile combustion can be described as follows:

$$CxHyOz + \frac{2x + y - 2z}{4} O_2 \rightarrow xCO + \frac{y}{2} H_2O \tag{2-12}$$

$$CO + \frac{1}{2}O_2 \rightarrow CO_2 \qquad 2\text{-}13$$

The eddy dissipation model (EDM) is commonly employed to model the turbulence-chemistry interaction model caused by the volatile combustion [57, 70]. In the EDM, which assumes that chemical reactions are infinitely fast, volatile combustions are not governed by reaction rates but by the turbulent mixing when the flow is fully turbulent [78-80]. Two turbulent mixing rates are computed in the EDM based on the Magnussen–Hjertager expression [70, 78, 79]: the first is the reactant mixing rate and the second is the product mixing rate. The net rate of production is determined by the smaller of the two turbulent mixing rates [12]:

2.2.4 Particle trajectory and particle impaction

Accurate prediction of particle trajectories and particle impaction, which determines the arrival rate of particles onto the deposition surface, is a prerequisite to predict the ash deposit formation. In terms of solid fuel combustion, particle transport modelling is determined by the Discrete Phase Model (DPM) using an Eulerian-Lagrangian approach [70]. In the DPM, the trajectory of the combusting particles is predicted by the equations of motion for the particles; The motion equation integrates the velocity of these particles, which is dictated by the force balance on the combusting particles [70]. Also, the particle trajectory is influenced by the fluctuating velocity of the gas phase in a turbulent flow. This can be predicted by using the stochastic tracking model (also known as the discrete random walk model) [70].

It should be noted that when an ash particle approaches the deposition surface in a boiler, there may exist three different orientations to the fluid streams [11]: (i) cross-flow when the deposition surface is the heat exchanger in the convection section of the boiler; (ii) flow moving along the deposition surface when the

surface is the water wall; (iii) recirculating flow when the surface is burner eyebrows. In deposition experiments from either a lab-scale combustor or a pilot scale combustor, the deposition probe is often inserted into the cross section of the furnace to collect the deposits. Therefore, ash deposit formation in a cross-flow is investigated during the deposition experiments.

For particle impaction on a pipe in a cross-flow, Israel et al. [81] developed a correlation to predict the particle impaction efficiency based on the particle Stokes number. The correlation, which is often employed to estimate the particle impaction efficiency (η_{ic}) caused by the inertia force for the pulverised coal combustion system [24, 82, 83], is defined as follows [81]:

$$\eta_{ic} = [1 + b(St - a)^{-1} + c(St - a)^{-2} + d(St - a)^{-3}] \quad (2\text{-}14)$$

$$St = (\rho_p d_p^2 U_p)/(9\mu_g d_c) \quad (2\text{-}15)$$

where St is the particle Stokes number, d_c is the diameter of the deposition probe, the values of a, b, c, and d are 0.125, 1.25, -0.014 and 0.508×10^{-4}, respectively [81].

Currently, from the publications related to the CFD prediction of ash deposition for solid fuel combustion, only some of the articles presented the particle impaction results. Only employing the final ash deposition results is not enough to be confident with the prediction of the particle deposition behaviours. However, only when both the particle impaction and particle sticking are reasonablely predicted then one can be confident in the prediction of ash deposition results since the final ash deposition results can be adjusted through the sticking model, even though an improper prediction of the particle impaction occurs [11, 84].

Wacławiak et al. [85] investigated ash deposit formation through a CFD simulation and the particle impaction efficiency results were presented. For particles with a small Stokes number, much larger particle impaction efficiency is predicted in the CFD results than that through the useful correlation by Israel et al. [81], as shown in Figure 2-1. Since only inertia impaction is considered in the particle transportation mechanism, there should not exist the high particle impaction efficiency for small particles, which may be caused by the improper mesh employed in the CFD study [84].

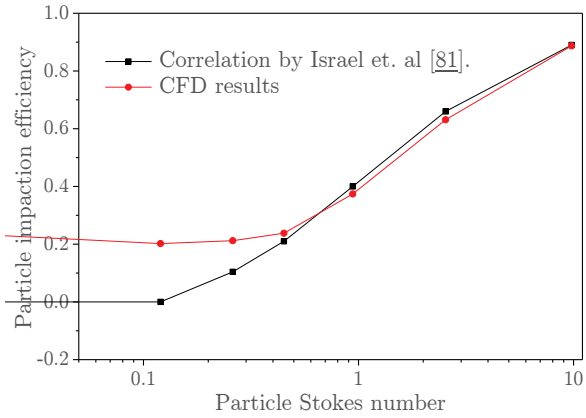

Figure 2-1 Comparison of the particle impaction efficiency between the CFD results and the correlation results as a function of the particle Stokes number [85].

Weber et al. [84] investigated the requirements for accurately calculating the particle impaction (particle arrival rate) on a probe in a cross-flow. The authors pointed out three different scenarios in the CFD prediction of particle impaction when only considering the inertia impaction, as shown in Figure 2-2. In order to achieve the accurate CFD-predictions of the particle impaction, the flow-field in the vicinity of the impaction surface needs to be accurately resolved by using a properly located fine grid. The fine grid should be applied in the vicinity region of the impaction surface in order to reach this aim. Therefore, a mesh independent study, which is evaluated by using the gas properties (gas temperature and gas velocity) in the bulk region of combustors [25, 50, 62], is not suitable for

determining a suitable mesh in order to resolve the particle impaction near the deposition surface. Furthermore, it is difficult to meet the mesh requirements to predict the particle impaction for an industrial boiler [84].

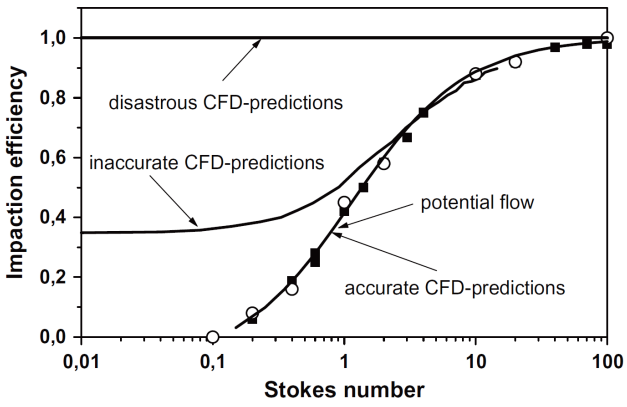

Figure 2-2 Three scenarios in predicting the impaction efficiency for particles approaching a probe by using CFD methods[11, 84]: the points are results by using the correlation of particle impaction efficiency.

2.2.5 Particle sticking

After the particles impact on the walls or surfaces of the boilers, not all the impacting particles can stick on the surfaces. The sticking efficiency, which is defined as the ratio of the impacting particles that can deposit on the surface to the total impacting particles, is dictated by both the physical properties of the impacting particles themselves and the physical properties of the deposition surfaces. Generally, the sticking efficiency can be determined based on such as the viscosity, the kinetic energy and the molten degree of the fly ash particles [86].

2.2.5.1 Viscosity based sticking model

The viscosity based sticking model was firstly introduced by Walsh et al. [46]. The sticking efficiency (η_{stick}) of the particles is defined as follows:

$$\eta_{stick}(T) = \begin{cases} \beta_{ref}/\beta & if\ \beta > \beta_{ref} \\ 1 & if\ \beta \leq \beta_{ref} \end{cases} \quad (2\text{-}16)$$

where T is the particle temperature, β_{ref} is the reference viscosity, β is the viscosity of the particles.

In order to employ this sticking model, the value of the reference viscosity needs to be assigned and the ash viscosity needs to be estimated. The reference viscosity was chosen as 8 Pa·s and a viscosity model for completely molten silicates was employed [46]. It should be noted that the chosen value for the reference viscosity is difficult since the value ranges within 8–10^8 Pa·s [62, 86], as shown in Table 2-1. This makes the viscosity based sticking model strongly sensitive to the reference viscosity and may contribute to an inaccurate stickiness prediction. In addition, in terms of the ash deposition scenario under a temperature much lower than the particle melting temperature, predicting the ash viscosity is challenging since ash particles are not completely molten, but rather liquid-solid mixtures. Furthermore, for some cases when high AAEM coals or biomass with high amounts of alkali/alkaline phases in the inorganic components are firing, it is difficult to predict the ash viscosity though current viscosity models [49].

Table 2-1 The reference viscosity used in the sticking models.

Work	Combustor and fuel	Reference viscosity
Walsh et al. [46]	Pilot scale furnace; Bituminous US coal.	8 Pa·s
Srinivasachar et al. [87]	Lab scale furnace; Bituminous US coal.	10^5 Pa·s
Huang et al. [82]	Lab scale furnace; Bituminous US coal.	10^4 Pa·s
Wang et al. [65]	Both pilot-scale and utility-scale combustion facilities; subbituminous and lignite US coal.	10^5 Pa·s
Wieland et al. [86]	Lab scale furnace; El Cerrejon coal and Pittsburgh No.8 coal.	10^4 Pa·s
Rushdi et al. [88]	Pilot-scale furnace; Australian bituminous coals.	10^8 Pa·s
Degereji et al. [50]	Pilot-scale furnace; Australian bituminous coals.	10^8 Pa·s

2.2.5.2 Kinetic energy thresholding sticking model

The kinetic energy thresholding sticking model, which is based on the Johnson–Kendall–Roberts (JKR) theory, takes into consideration the kinetic energy of the particles and the surface energy of both the particle and the impacted surface. It is regarded that if the dissipated energy due to the impaction is larger than the particle's kinetic energy, then the particle will not rebound from the surface [11, 89]. Based on this assumption, a critical velocity, V_{cr}, can be determined as follows [89, 90]:

$$V_{cr} = \left(2K/d_p R^2\right)^{10/7} \tag{2-17}$$

$$K = 0.51\left[5\pi^2(k_s + k_p)/(4\rho_p^{3/2})\right]^{2/5} \tag{2-18}$$

$$k_s = (1 - \nu_s^2)/(\pi E_s) \tag{2-19}$$

$$k_p = (1 - \nu_p^2)/(\pi E_p) \tag{2-20}$$

where K is the effective stiffness parameter, ν_s and ν_p are the Poisson's ratios of the surface and particle, respectively, E_s and E_p are the Young's modulus of the surface and the particle, respectively, d_p and ρ_p are the diameter and the density of particle, R (=0.9) is the kinematic restitution coefficient [89]. It is assumed that $E_s = E_p$. In addition, the correlation of E_p is a function of the particle temperature and the particle diameter. The sticking condition is usually defined as that the particle velocity is not larger than the critical velocity [11, 89].

It should be noted that, in order to employ this sticking model, a fitting process is required to obtain the correlation of E_p, which is a function of the particle temperature and the particle diameter, by matching the experimental data with the simulation results [89]. In addition, the adhesion work and the Young's modulus are influenced by the material. Currently, the information of these two

parameters for coal ash with high alkali/alkaline metals and biomass ash are rare, which increases the difficulty employing the kinetic energy thresholding sticking model.

2.2.5.3 Molten degree based sticking model

The molten degree based sticking model regards that the sticking efficiency of the particles is dictated by the melting ability of the ash particles and the deposit on the deposition surface. The melting ability is usually evaluated by the ash fusion experiments and the melting curves based on the thermodynamic calculations.

For the ash fusion experiment determination, there are two different methods: (i) this is based on the AFTs, and (ii) the other is based on the height of ash samples during the ash fusion experiments. The sticking efficiency can be defined as follows:

$$\eta_{stick}(T) = \begin{cases} (FT - T_p)/(FT - IDT) & (i) \\ (h_{max} - h_T)/(h_{max} - h_{min}) & (ii) \end{cases} \quad (2\text{-}21)$$

where FT, IDT, and T_p are the fluid temperature, initial deformation temperature and the particle temperature, respectively, h_{max}, h_{min} and h_T are the maximum height of the ash sample, the minimum height of the ash sample and the height of the ash sample under the particle temperature. It should be noted that particle melting and particle deposition occurs at a temperature much lower than the IDT and the maximum height [63]. Therefore, this kind of sticking model may not be suitable for particle deposition under a lower furnace temperature.

In terms of the melting curves based criteria, the sticking efficiency can be directly represented by the molten fraction [86]. The molten fraction can be determined by the thermodynamic equilibrium calculations. It is regarded that

[86]: (i) compared to the viscosity based sticking model, the melt fraction based sticking model can predict the ash deposition in a higher temperature range, and (ii) compared to the ash fusion experiment based sticking model, the melt fraction based sticking model can predict the ash deposition under lower temperature.

2.2.6 Ash deposition growth and shedding

The ash deposition rate is a combined result of the deposition build-up rate and the deposit shedding rate. At the initial stage of ash deposition, vapour condensation and sticky particles are deposited on the clean heat exchangers. In the radiation section of the boilers, condensation is less significant due to the high furnace temperature. The deposit temperature increases with the deposit growth. This results in a higher particle temperature and may increase the particle sticking efficiency. In addition, the melt phases may generate on the deposit and enhance the sintering degree of the deposit. With the further deposit growth, the deposit may be removed by the shedding, which is caused by the erosion, liquid flow at the deposit surface, gravity shedding, etc. [59]. In addition, the deposit characteristics (porosity, heat conductivity, emissivity, etc.) change with the ash deposition growth. Due to the formation of the melt phases and the increase of the sintering degree, it is commonly regarded that the porosity can decrease and the heat conductivity can increase with the deposition growth [91].

2.2.7 Current research on the CFD prediction of ash deposition

Generally, the CFD methods for predicting the ash deposition behaviour can be divided into two groups, the steady simulation and the dynamic simulation. In terms of the steady simulation based CFD methods (as shown in Table 2-2), it is assumed that both the ash deposition rate and the deposit characteristics are not dependent on the deposit growth. However, in terms of the dynamic simulation based CFD methods (as shown in Table 2-3), it is regarded that both

the deposition rate and the deposit characteristics are dependent on the deposition growth. Therefore, the steady state based CFD methods are more suitable for the deposit formation on an uncooled deposition probe, although some researches have improperly employed the steady state based CFD methods to simulate the ash deposition on cooled heat exchangers [50, 62, 92]. This is because the deposit surface temperature is close to the furnace temperature under this condition and the influence of deposit surface temperature on the particle deposition behaviour cannot change significantly with the deposit growth. In addition, the dynamic simulation based CFD methods are more suitable for the deposit formation on a cooled deposition probe. This is because the deposit surface temperature changes with the deposition growth, which results in both the deposition rate and the deposit characteristics changing with the deposit growth.

Table 2-2 Steady state based CFD simulations of ash deposit formation for solid fuel combustion.

Work	Combustor/Deposition regions	Ash deposition model
Huang et al. [82] (1995)	Lab-scale and pilot-scale combustors; superheaters.	Thermophoresis and inertial impaction; viscosity based sticking model.
Mueller et al. [93] (2003)	Boilers; heat exchanger surfaces.	Inertial impaction; melt based sticking model.
Degereji et al. [50] (2012)	Pilot-scale furnace; burner region and furnace wall.	Inertial impaction; viscosity based sticking model and particle momentum rebounding model.
Taha et al. [62] (2013)	Boiler; furnace walls and superheaters.	Inertial impaction; viscosity based sticking model.
Garba et al. [25] (2013)	Lab-scale furnace; uncooled deposition probe.	Thermophoresis and inertial impaction; viscosity and melt based sticking model.
Wieland et al. [86] (2013)	Lab-scale furnace; deposition probe.	Only inertia impaction; Viscosity and melt fraction based sticking model

2.2.7.1 Steady state models

Huang et al. [82] predicted the ash deposit formation on superheaters in a drop tube furnace and a pilot-scale pulverized coal combustor. Both thermophoresis and inertia impaction were considered to be responsible for the transportation of the ash particles. Particle impaction efficiency was predicted based on the useful correlation by Israel et al. [81]; Particle sticking efficiency was predicted based on the viscosity based sticking model. It was found that particles with higher density are more prone to impact on the deposition surface than particles with smaller density; The furnace temperature, which can affect the particle temperature, is a significant factor in determining the ash deposit formation; Both the ash yield and the ash composition have a strong influence on the deposition rate and deposition characteristics.

Muller et al. [93] predicted the ash deposit formation in a biomass fired fluidised bed boiler. (i) Inertia impaction was considered for the particle transportation; (ii) Particle impaction efficiency was assumed to be unity, which represents the worst scenario for particle impaction; (iii) Particle sticking model was developed based on the melting behaviour of biomass ash combined with advanced fuel analysis (chemical fractionation analysis and chemical equilibrium calculations). Qualitative agreement was obtained between the predicted results and the experimental data for the deposition region.

Degereji et al. [50] predicted the ash deposit formation in an Australian Coal Industries Research Laboratories (ACIRL) furnace. A two-dimensional mesh was employed and the mesh independent study was based on comparing the gas temperature and gas velocity in the mainstream. (i) Inertia impaction was considered for the particle transportation; (ii) No special treatment was employed to the particle impaction; (iii) Particle sticking was predicted based on the viscosity based model and particle momentum rebounding model. Qualitative

agreement was obtained between the predicted results and the experimental data for the deposition rate.

Taha et al. [62] predicted the ash deposit formation for co-combustion in a tangentially fired utility boiler. A three-dimensional mesh was employed and the mesh independent study was based on comparing the gas temperature along the boiler height. (i) Inertia impaction was considered for the particle transportation; (ii) No special treatment was employed to the particle impaction; (iii) Particle sticking was predicted based on the viscosity based model. It was observed that the slagging on the furnace wall increase with increasing the biomass co-firing ratio, but the wall slagging may reduce at 40% co-firing ratio due to the incomplete combustion of the biomass. Also, the flame height, which has a strong influence on the particle temperature, increases due to the high volatile concentration in the biomass.

Garba et al. [25] predicted the ash deposit formation for co-combustion on an uncooled deposition probe in a drop tube furnace. A three-dimensional mesh was employed and a mesh independent study was based on comparing the gas temperature and gas velocity in the mainstream. (i) Both thermophoresis and inertia impaction were considered to be responsible for the transportation of the ash particles; (ii) No special treatment was employed to the particle impaction; (iii) Particle sticking was considered separately for coal and biomass. The viscosity based sticking model was employed for coal and melting curve based sticking model was employed for biomass. Qualitative agreement was obtained between the predicted results and the experimental data for the deposition rate.

Wieland et al. [86] compared the performance of different sticking models on predicting the ash deposition behaviour for coal combustion in a drop tube furnace. In the particle sticking model, different empirical viscosity models were tested to predict the particle viscosity; different melting criteria were tested to

predict the particle melting behaviours. It was found that the viscosity based model is very sensitive to the reference viscosity; the ash fusion criteria was not reasonable for the Pittsburgh No. 8 coal. However, the melting curve based on chemical equilibrium calculations may bring the most promising results, since the melt fraction of the ash particles is considered.

Weber et al. [84] investigated the requirements for accurate prediction of particle impaction by using the RANS-based CFD methods. It was found that extremely fine mesh is required near the deposition surface to accurate predict the flow-field and particle impaction. Therefore, a mesh, which is developed based on the gas properties in the mainstream, may not be suitable to resolve the particle impaction near the deposition surface. However, this mesh requirement is difficult to be satisfied in the simulation of an industrial boiler [11, 84].

2.2.7.2 Dynamic models

Richards et al. [94] and Wang et al. [65] have predicted the slagging formation on the furnace wall. The deposit properties were defined to be dependent on the solid fraction and liquid fraction in the deposit. The deposit surface temperature, which is dependent on the deposit growth, is determined by predicting the heat transfer rate though the deposit. It was observed that the deposit surface temperature sharply increases at the initial stage and then slowly increases at the later stage, which is dictated by the variances of the heat conductivity and the heat flux. The deposit porosity gradually reduces due to the generation of the liquid phase in the deposit.

Table 2-3 Dynamic CFD simulations of ash deposit formation for solid fuel combustion.

Work	Combustor/Deposition regions	Ash deposition model
Richards et al. [94](1993)	Pilot-scale combustors; Furnace wall.	Only inertial impaction; Viscosity based sticking model; Heat transfer rate through the deposit.
Wang et al. [65] (1997)	Pilot-scale combustors; Furnace wall.	Only inertial impaction; Viscosity based sticking model. Heat transfer rate through the deposit.
Kaer et al. [91] (2006)	Straw-fired grate boilers; Superheaters and tube banks.	Thermophoresis and inertial impaction; melt fraction based sticking model; Heat transfer rate through the deposit.
Li et al. [95, 96] (2009 and 2013)	Kraft recovery boiler; Superheaters.	Thermophoresis and inertial impaction; Force balance based sticking model; Heat transfer rate through the deposit.
Wacławiak et al. [85] (2012)	Boiler; Superheaters.	Only inertial impaction; Force balance based sticking model; dynamic mesh.

Kaer et al. [91] developed a dynamic ash deposit model for straw combustion in a grate boiler. The inertia impaction, thermophoresis, and turbulent eddies were considered to be responsible for the transportation of the ash particles. Qualitative agreements were obtained between the predicted results and the experimental data for identifying the slagging regions in the boilers. Li et al. [95, 96] employed a dynamic slagging model to predict the ash deposit formation for a heat recovery boiler to investigate the deposit growth and its influence on the heat transfer rate through the heat exchanger tube. Wacławiak et al. [85] developed a slagging prediction model to investigate the slagging growth on the heat exchanger tube banks. Also, a dynamic mesh was employed to predict the shape of the deposit with the deposit growth.

2.3 Ash deposition indices

The ash deposition indices are often based on the physical and chemical properties, such as AFTs (ash fusion temperatures), sintering properties,

viscosity, ash composition, and melt fraction. These indices are not only simple and easy to compute, but also can provide a reasonable accuracy for specified coals. Therefore, it has a wide range of applications in engineering. In order to improve the accuracy of these traditional indices, several synthetical slagging indices have been developed based on these single indices.

2.3.1 AFT indices

AFTs based indices are very common practice for ash deposition prediction. It is often regarded that IDT corresponds to the temperature where the less sintered ash deposition commences and ST corresponds to the temperature where serious slagging/fouling issues occur [97, 98]. Therefore, the furnace exit gas temperature (FEGT) should be lower than the ST in order to avoid the ash deposition issues. In addition, for wet bottom combustors/gasifiers, the ST and FT are important parameters to choose the operation temperature in order to avoid slag block.

- ST >1350 °C represents a low slagging potential; ST <1350 °C represents a medium or high slagging potential [99].
- $(HT_M+4IDT_M)/5$[2], this indice is more suitable for lignite or coal with an ash content ($CaO+MgO>Fe_2O_3$) [22]: the indice >1343 °C, low slagging potential; 1232-1343 °C, medium slagging potential; 1149-1232 °C, high slagging potential; <1149 °C, severe slagging potential.

It should be noted that AFT measurement is a subjective assessment, which may lead to an inaccurate result, especially for the IDT [12, 100]. In addition, AFTs only represent the overall melting behaviour of the ash composition and ignore the selective melting/evaporation behaviour of some basic components (Fe,

[2] HT_M represents the HT under the oxidising atmosphere and IDT_M represents the IDT under the reducing atmosphere.

alkali/alkaline metals, etc.). Both disadvantages may reduce the accuracy of using AFTs to predict the ash deposition behaviour in real boilers.

2.3.2 Ash sintering

Ash sintering is an indication of the severity of ash deposit formation in the convection section of boilers [97]. Two parameters (sintering strength and the initial sintering temperature) are proposed to represent the ash sintering properties and they are often employed to predict the ash deposition propensity [97]. It is often regarded that coal ash with higher sintering strength after heat treatment and lower initial sintering temperature can represent a higher ash deposition potential.

- Sintering strength (SS) under 925 °C heat treatment [97]: the indice < 6.89 MPa, low ash deposition potential; 6.98-34.47 MPa, medium ash deposition potential; 34.47-110.32 MPa, high ash deposition potential; >110.32 MPa, severe ash deposition potential.

2.3.3 Ash viscosity

For a wet-bottom combustor/gasifier, there is a suitable viscosity range (ash viscosity cannot be either too high or too low) to maintain long-term operation in a cost-effective manner [45]. However, for a dry bottom combustor, it is often regarded that coal ash with lower viscosity may represent a higher slagging propensity. It is often employed by using the ash viscosity at a given temperature, the temperature at a given viscosity and the critical viscosity in order to predict the ash deposition behaviour.

- R_N<0.05, low slagging potential; 0.05-0.15, medium to high slagging potential; >0.15, severe slagging potential. R_N is defined as in [101]:

$$R_N = 2 \bullet (T_{250} - T_{10000}) / (T_{250} + T_{10000}) \quad (2\text{-}22)$$

where, T_{250} and T_{10000} are the temperatures at which the viscosity is 250 and 10000 Pa·s, respectively. It should be noted that the experimental measurement of the ash viscosity is difficult and expensive. Although many viscosity prediction models have been developed, these models may be more suitable for coal ash with silicate as the major ash composition. In addition, the ash viscosity only represents the overall ash behaviour and cannot represent the selective ash melting/evaporation behaviour.

2.3.4 Ash composition

Since the ash behaviours are dictated by the ash composition, many ash deposition indices have been developed by using the ash composition, as defined in Equations (2-23) - (2-27). These indices attempt to correlate the concentration of some ash compositions with ash properties (ash melting, ash sintering, and ash viscosity). In addition, some indices incorporate the specific ash compositions to represent the selective ash deposition behaviours in boilers.

- Silica ratio, I_Si, represents the weight fraction of SiO_2 in the ash [102]. It can be used to correlate the ash viscosity under high temperature and estimate the ash deposition propensity. The higher values of I_Si lead to lower ash deposition propensity. I_Si>0.72, low slagging potential; 0.65-0.72, medium slagging potential; <0.72, high to severe slagging potential.
- Basic/acid ratio, $I_{B/A}$, represents the ratio of the total basic components to the total acid components [102]. It can be used to correlate the ash fusion temperature and the ash viscosity under high temperatures and estimate the ash deposition propensity [103]. The higher values of $I_{B/A}$ lead to higher ash deposition propensity. $I_{B/A}$<0.2, low slagging potential; 0.2-0.4, medium slagging potential; >0.4, high to severe slagging potential.

However, for lignitic ash, $I_{B/A}$ <0.5, low slagging potential; 0.5-1.0, medium slagging potential; >1.0, high to severe slagging potential.

- Slagging factor, $I_{B/A} \times S$, is given by the result of the Basic/Acid ratio multiplied by the sulphur content [102]. This slagging indice is attributed to the contribution of both the pyrite induced slagging and the overall slagging behaviour. The higher is the value of $I_{B/A} \times S$, the higher is the ash deposition propensity. $I_{B/A} \times S$<0.6, low slagging potential; 0.6-2.0, medium slagging potential; 2.0-2.6, high slagging potential; >2.6, severe slagging potential. However, for bituminous ash, $I_{B/A} \times S$>2.0, severe slagging potential.
- Iron oxide content in ash, $I_{Fe_2O_3}$, represents the pyrite induced slagging [102]. The higher the value of $I_{Fe_2O_3}$, the higher is the ash deposition propensity. $I_{Fe_2O_3}$ <8, low slagging potential; 8-15, medium slagging potential; >15, high to severe slagging potential.
- Iron oxide to calcium oxide ratio, $I_{Fe/Ca}$, is correlated to the overall ash melting behaviour [102]. $I_{Fe/Ca}$, <0.3 and >3.0, represent low to medium slagging potential; 0.3-3.0, represents high to severe slagging potential.
- Silica to alumina ratio, $I_{Si/Al}$, is correlated to the ash viscosity when the total amount of basic components is low [97, 102]. In addition, it is regarded that $I_{Si/Al}$ may decrease the ash fusion temperatures. Therefore, the higher the value of $I_{Si/Al}$, the higher is the ash deposition propensity. $I_{Si/Al}$<1.4, low slagging potential; 1.4-2.8, medium slagging potential; >2.8, high to severe slagging potential.

$$I\_Si = \frac{SiO_2}{(SiO_2 + Fe_2O_3 + CaO + MgO)} \quad (2\text{-}23)$$

$$I_{B/A} = \frac{(Fe_2O_3 + CaO + MgO + K_2O + Na_2O)}{(SiO_2 + TiO_2 + Al_2O_3)} \quad (2\text{-}24)$$

$$I_{B/A} \times S = I_{B/A} \times \%Sulphur \quad (2\text{-}25)$$

$$I_{Fe_2O_3} = Fe_2O_3 \ content \ in \ the \ ash \quad (2\text{-}26)$$

$$I_{Fe/Ca} = Fe_2O_3/CaO \quad (2\text{-}27)$$

$$I_{Si/Al} = SiO_2/Al_2O_3 \quad (2\text{-}28)$$

2.3.5 Thermodynamic equilibrium

Since it is quite difficult for both AFTs and the ash composition based indices to accurately estimate the whole melting behaviour of coal ash under a reasonable temperature range, thermodynamic equilibrium methods are often employed to calculate both the mineral reactions and the phase transformations of coal ash under high temperatures. The thermodynamic equilibrium is calculated based on the minimizing of the Gibbs free energy. The ideas of minimization of the Gibbs free energy are that [104]: (i) At constant pressure and temperature, compute the equilibrium components under the constraint that the Gibbs free energy is minimized; (ii) It is not necessary to compute the specific chemical reactions and this can avoid the understanding of the detailed reaction mechanisms. Therefore, the minimization of the Gibbs free energy is widely employed to compute the thermodynamic equilibrium in the coal ash/slag system.

Van Dyk et al. [105-107] investigated mineral transformations (especially Ca-containing minerals) and slagging properties for a fixed bed gasification reactor. Thermodynamic computation results indicated that anorthite ($CaSi_2Al_2O_8$) forms within the gasification zone and all non-reacted Ca reacts with CO_2 to form $CaCO_3$ further down in the combustion zone [107]. In addition, the predicted results using Factsage was correlated with the high temperature X-ray diffraction

(HT-XRD) results [105]. Also, Factsage was employed to predict the composition of the slag and then the viscosity can be predicted after this [108].

Song et al. [53-55] studied the relationship of the liquidus temperatures and AFTs and the relationship of the liquid phase content and the critical viscosity temperature under different atmospheres by employing the thermodynamic equilibrium calculations. Reliable correlations can be acquired from their results and therefore the thermodynamic equilibrium calculation can be employed to forecast the ash viscosity.

In addition to predicting the mineral transformation and viscosity, the melt fraction predicted from the thermodynamic equilibrium calculations is widely applied for directly comparing the slagging potential. Gilbe et al. [109] predicted the deposition tendencies for biomass by employing different methods, including AFTs, thermal-gravimetric analysis and differential thermal analysis (TGA/DTA), deposition indices, and chemical equilibrium calculations. It was found that the chemical equilibrium calculations can obtain relatively good agreements for the actual slagging tendencies from the combustion tests [109]. However, the authors also pointed out that the chemical equilibrium calculations must be further improved before quantitative results can be employed [109]. Öhman et al. [110] investigated the sintering tendencies of wood pellets (sawdust, logging residues and bark). Their results indicate that [110]: The slagging properties were relatively sensitive to the variations in the total ash content and ash forming elements; Good quantitative agreement between chemical equilibrium modelling and experimental results were obtained.

It should be noted that the thermodynamic equilibrium is based on the assumption that all the reactions are able to reach equilibrium and all the reactants are well mixed. Therefore, in order to better understand the deposition

property and obtain better thermodynamic equilibrium calculations, it is essential to understand the ash forming compositions and the ways they are associated in the fuel as part of the organic structures, salts and minerals [111]. Chemical fractionation analysis (CFA) is often employed to investigate the modes of ash-forming matter in coal [111]. The procedure of CFA normally involves a standard leaching process with a set of successively more severe chemical reagents, e.g. water→ammonium acetate solution→hydrochloric acid solution [112]. After the leaching, four factions can be obtained [112]: (i) the water-leachable components which are mainly the alkali metal salts and, the chlorine and sulphur based anions; (ii) the acetate-leachable components, such as materials in the form of cations and chelates; (iii) the acid-leachable components, such as the carbonates and sulphates; (iv) the solid residue, mainly silica, silicates and other acid-unleachable mineral species. In general, it is regarded that [112]: water and acetate-leachable components may be released into the gas phase, which may generate aerosols; the acid soluble and solid residue fractions may tend to form coarser fractions of the ashes. Therefore, it is suggested that, in the thermodynamic equilibrium computation, only the reactive fraction should be employed as input for the modelling, whereas the non-reactive fraction is regarded as being relatively inert [112].

Nutalapati et al. [113] studied the ash behaviours of wheat straw combustion by using CFA based thermodynamic equilibrium calculations. It was assumed, in addition to the reactive fraction, under high temperatures, a part of the non-reactive fraction may be reactive. Two models have been introduced and compared in the computations [113]: (i) The first method is based on only CFA; (ii) The second method is based on not only CFA, but also secondary reactions (part of the non-reactive fraction, mainly silica). The results indicate that [113]: (i) The melt proportion from the first model is as low as about 5% and this

indicates that there is not a severe slagging problem; (ii) However, in the second model, the melt fraction increased with the increasing amount of non-reactive components and for 10% and 25% non-reactive fraction adding, the melt proportion is more than 15%, which indicates significant slagging problems. Additionally, the amount of potassium sequestered in the condensed phase increased with an increase in the non-reactive fraction in the high-temperature section [113]. In 5% of non-reactive fraction calculation, around 10–15% of total potassium is in the slag phase in the temperature range of 1600–1300 °C. The potassium concentration in the condensed phase increased to about 28–47% when the non-reactive fraction increased to 25%[113].

2.3.6 Current research on ash deposition indices

Generally, using ash deposition indices in predicting the ash behaviours (melting, sintering and viscosity) includes the ash fusion/sintering experiments, ash composition and theoretical calculations. Recent studies not only employ the ash composition which is related to the ash deposition issues to develop the indice, but also use synthetical indices to predict the ash deposition issues.

Gibb [68] developed a slagging indice (I_{CCSEM}) based on computer controlled scanning electron microscopy (CCSEM) based mineral compositions in the coal. For UK coals, iron (derived from pyrite) and calcium (derived from calcite) are the major fluxing elements that contribute to the melt formation and affect the ash sintering and ash viscosity. Therefore, the slagging indice assumes that the slagging behaviour of UK coals is dictated by the degree of assimilation of these fluxing elements into the alurninosilicate glass. It was found that the predicted results by using this indice agreed well with the deposit structure for three coals combustion. It should be noted that the degree of the slagging severity is represented by the degree of the melting and sintering degree of the deposits. In

addition, the indice assumed that pure pyrite particles are less possible to cause ash deposition issues than the pyrite assimilated into the alurninosilicate glass. However, pure pyrite particles are very significant for the initial slagging formation on the furnace wall in boilers. This CCSEM based indice is yet to be validated with other real boilers.

$$I_{CCSEM} = \sum_{\substack{all-min-\\ occurrences}} \left\{ m_{fraction} \left[CaO + Fe_2O_3 \left(1 - 0.5 \frac{Fe_2O_3}{Fe_2O_3 + Al_2O_3 + SiO_2} \right) \right] \right\} \qquad (2\text{-}29)$$

Chen et al. [114] developed a synthetical slagging indice based on the Basic/Acid ratio, the silica to alumina ratio, AFTs and the silica ratio. This indice assumed that the overall melting propensity dictates the ash deposition behaviour. However, Tang [115] employed this synthetical indice to evaluate the slagging propensities for ten coal blends and found that the accuracy of the synthetical indice was only about 60%.

McLennan et al. [22] developed the CCSEM based slagging indices, $I_{Fe-CCSEM}$ under oxidising and reducing atmospheres. The slagging indice took into consideration the ash deposition issues caused by the iron species in coal. It was regarded that the extent of the included iron minerals is significant for generating ash deposition under oxidizing conditions. In addition, both the excluded pyrite mineral and the included iron-containing minerals associated with clays were significant for generating ash deposition under reducing conditions. Therefore, this indice is only suitable for iron related ash deposition issues. This CCSEM based indice is yet to be validated with field observations in real boilers. The indices are shown as follows:

Oxidising atmosphere:

$$I_{Fe-CCSEM} = \left[(FeCO_3 + FeS_2 + FeS)_{excl} * E(T)_{OX} + 0.5 * (FeCO_3 + FeS_2 + FeS)_{incl} * E(T)_{OX} + 0.5 * (FeCO_3 + FeS_2 + FeS + SiO_2 - Al_2O_3)_{incl} * D(T)_{OX}\right] \quad (2\text{-}30)$$

Reducing atmosphere:

$$I_{Fe-CCSEM} = \left[(FeCO_3)_{excl} * B(T)_{RED} + (FeS_2 + FeS)_{excl} * A(T)_{RED} + 0.5 * (FeCO_3)_{incl} * B(T)_{RED} + 0.5 * (FeS_2 + FeS)_{incl} * A(T)_{RED} + 0.5 * (FeCO_3 + FeS_2 + FeS + SiO_2 + Al_2O_3)_{incl} * C(T)_{RED}\right] \quad (2\text{-}31)$$

where, $A(T)_{RED}$, $B(T)_{RED}$, $C(T)_{RED}$, $D(T)_{OX}$, and $E(T)_{OX}$ represent the sticking temperature of the related iron-containing ash phases (FeO-FeS, wustite, Fe-glass under reducing atmosphere, Fe-glass under oxidising atmosphere, and magnetite/hematite, respectively).

Barroso et al. [102, 116] employed some conditional slagging indices to predict the slagging observations of coals/blends in an entrained flow reactor. The predicted results can be improved by incorporating the ash content and the aerodynamic diameter of fly ash into the conventional slagging indices. It should be noted that the slagging propensity is represented by the deposit mass in the experiments. In an entrained flow reactor, the gas velocity is as low as approximately 0.5 m/s, which may result in fewer particle rebounding after impaction than the high fluid velocity condition that occurs in real boilers. Therefore, the deposition propensity could increase in a higher particle impaction caused by a higher value of the aerodynamic diameter of particles.

Lawrence et al. [100] and Degereji et al. [25, 50, 117] developed the slagging indices based on the overall ash behaviour (the ash sintering and the ash viscosity) and the energy based ash content. It should be noted that only considering the

overall ash behaviour can neglect the influence of selective fluxing elements on the ash deposit formation.

2.4 Knowledge gap

2.4.1 CFD methods

The CFD based ash deposition models have been developed based on resolving particle impaction and particle sticking. Both numerical methods and proper ash deposition sub-models are required to accurately predict these physical ash deposition mechanisms.

2.4.1.1 Particle impaction

It is regarded that the accurate predictions of the particle impaction is a prerequisite for predicting the ash deposit formation [84]. The impaction efficiency of the particles is usually assumed to be unity which represents the worst scenario in terms of the ash deposition rate [93, 118]. In practice the impaction efficiency can be much lower than this depending on the size, shape and density of the particles and the nature of the depositing surface. Weber et al. [84] investigated the requirements for accurate predictions of the impaction efficiency of fly ashes in a 2D geometry using the RANS- based CFD methods. It was concluded that only when the flow-field in the neighbourhood of the deposition surfaces is accurately resolved can accurate predictions of the particle impaction be obtained by using the RANS-based CFD methods, especially for small particles since their trajectories are strongly affected by the boundary layer development. Haugen et al. [119, 120] applied direct numerical simulation (DNS) to investigate the particle impaction behaviour on cylinders and superheater tube bundles in a crossflow in order to accurately resolve the boundary layers around the cylinders. It should be noted that in these models [84, 119, 120], an extremely fine grid for RANS or DNS is needed. However, it is very difficult to accurately

predict the particle impaction since an extremely fine grid is required in order to accurately resolve the flow field in the neighbourhood of the deposition surfaces [84]. This requirement is difficult to be satisfied in three-dimensional combustors, especially in real boilers. A coarse mesh near the deposition surface may cause inaccurate predictions of particle impaction, especially for small particles [84]. Currently, most of the publications have not taken into consideration this issue, which may result in an inaccurate prediction of the particle impaction behaviour.

2.4.1.2 Particle sticking

In addition to the particle impaction, the stickiness of the ash particles plays a critical role in the formation of ash deposit and related slagging and fouling. The stickiness of an ash particle can be determined based on such as the viscosity, kinetic energy and the degree of molten of fly ash particles. In terms of viscosity based sticking models, a reference viscosity is used to determine the stickiness. The value of the reference viscosity ranges within $8\text{-}10^8$ Pa.s which makes the sticking model strongly sensitive to the reference viscosity and may contribute to an inaccurate stickiness prediction [62, 86]. In addition, the kinetic energy thresholding sticking model, based on the Johnson-Kendall-Roberts (JKR) theory [89, 90, 121], has been proposed which takes into account the kinetic energy of the particles and the surface energy of both the particles and the impacted surface. However, a fitting process was necessary to develop the effective Young's modulus versus the particle temperature and the particle diameter by matching the experimental data with the simulation results [89]. In addition, the biomass ash (e.g. palm kernel) and the coal ash (e.g. Zhundong lignite) have a high content of potassium/phosphorus and sodium/calcium, which increases the difficulty to predict the ash viscosity and the effective Young's modulus from the present modelling methodology.

2.4.1.3 Dynamic CFD model

Currently, most of the publications employ the 'steady state' assumptions for the deposition rates to develop the sub-models in the CFD methods (for better describing the ash deposition behaviours [82, 89, 93, 122-125], for new fuels [25, 62, 126-128], for the oxy-combustion condition [129], etc.). This kind of assumption is suitable for the ash deposit growth on the uncooled deposition tube where the deposit surface temperature is close to the furnace temperature, which results in the stable particle impaction and sticking. However, for real heat exchanger tubes (which are cooled in boilers), the deposit surface temperature on the tube could increase with the growth of the deposit. This may change the particle impaction and sticking behaviours and the contribution of the major deposition mechanisms on the overall ash deposition growth. Therefore, only a dynamic consideration of the ash deposition growth is suitable for a cooled tube. Recently, only a limited number of studies have investigated the ash deposition growth through a dynamic CFD simulation. Kaer et al. [91] developed a dynamic CFD model to predict the ash deposit formation and heat transfer rates and the paper focused on straw combustion and investigated the ash deposition rate caused by different deposition mechanisms. Wang et al. [65], Li et al. [96, 130], and Balakrishnan et al. [131] developed CFD models to predict the ash deposition growth and heat transfer rate for boilers. Their models mainly considered the slag layer growth where the inertial impaction mechanisms are the main contribution. Waclawiak et al. [85, 132] modelled the ash deposit growth in the convection section based on the inertial impaction mechanism. Garcia-Perez et al. [133] modelled the deposit growth of fume particles based on the thermophoretic force, Brownian motion and inertial impaction. In both the Waclawiak and Garcia-Perez's models, they focused on predicting the deposit shape and weight. The energy conservation principles were neglected in their models, which cannot consider the influence of the increase of the deposit surface temperature on the

deposition behaviour. In addition, the details of particle impaction and sticking behaviours during the deposition growth process are still not clear from these previous publications [65, 85, 91, 94-96, 132, 133].

2.4.2 Ash deposition indices

The ash deposition indices are widely used in engineering in order to predict the ash deposition propensity. Currently, many indices have been developed based on the ash chemistry and ash properties (ash melting, ash sintering and ash viscosity). Although there exist several publications on developing a slagging indice for coal combustion, most of these methods were developed either based on slagging observations in entrained flow reactors or by only considering the sintered/slagging route [22, 68, 102, 125, 134, 135]. Gibb et al. [68] developed a slagging indice based on the Computer Controlled Scanning Electron Microscopy (CCSEM) based mineral composition in the coal. This indice was developed based on the assumption that the degree of assimilation of iron and calcium into the aluminosilicate glass determines the ash deposition characteristics of the coal. This assumption neglects the influence of the initial slagging routes caused either by pyrite or by condensation. McLennan et al. [22] developed an iron-based slagging indice based on the included and excluded iron related minerals composition in the coal. However, this indice only considers the effect of iron related minerals on the slagging behaviour. Also, both of these two CCSEM slagging indices are yet to be validated with full-scale field observations in boilers [125]. In addition, Barroso et al. [102, 116] employed conventional slagging indices to predict the slagging potential of coals/blends in an entrained flow reactor. It was found that by incorporating the aerodynamic diameter of fly ash particles into the conventional slagging indices one can improve the prediction performance because the aerodynamic diameter is proportional to the particle Stokes number which determines the particle impaction efficiency [125, 136]. It

should be noted that the fluid velocity in the EFR is as low as approximately 0.5 m/s [102, 116], which means that particles may not have enough kinetic energy to rebound from the deposition surface after impaction and hence deposition accumulation could increase with an increase in the aerodynamic diameter under this low velocity condition in the EFR [93]. However, the fluid velocity could be as high as 10-25 m/s in pulverised coal boilers and, for the particles with similar aerodynamic diameter, it is possible to have high enough kinetic energy (proportional to the square of the velocity, possible 20^2-50^2 times higher than in the EFR) to rebound from the deposition surface after impaction [9, 93]. Therefore, the conclusions from the low velocity conditions of the EFR may not be suitable for the real conditions in boilers.

Moreover, for some of the existing typical slagging indices (B/A, B/A*Sulphur, Si value, etc.), the slagging prediction for the sintered/slagging route directly employs the mass fractions of ash components and assumes the same contribution of each basic or acid component to the slagging prediction. However, the sintered/slagging layer is not linearly related to the mass fraction of the basic or acid components [55, 137, 138]. Further, fuel ash content and heating values are important factors of ash deposit formation. A numerical slagging indice (NSI) has been developed to reflect these factors for both single coals and blends of coal and biomass [25, 117, 135]. The NSI has shown reasonable success in ranking the slagging potentials of some of the world trade coals. Nevertheless, in general, uncertainty still exists in the understanding of the contributions from different slagging routes and correlations between the existing coal slagging indices and the actual observations made in conventional boilers. Therefore, it is still very important to develop an ash deposition indice which can better represent the ash properties and the ash deposition routes in order to provide guidelines for real engineering applications.

Chapter 3: Experimental facilities and data

Summary

This chapter introduces the experimental facilities and data which are used to develop and validate the ash deposition prediction models. Ash deposit formation on an uncooled deposition probe for the co-combustion of South African coal and palm kernel expeller in an entrained flow reactor is applied to develop the steady CFD based ash deposition model, as described in Section 3.1. Ash deposit formation on a cooled deposition probe for the Zhundong lignite combustion in a pilot scale coal-fired furnace is applied to develop the dynamic CFD based ash deposition model, as described in Section 3.2. The ash deposition observations in utility boilers are applied to develop the ash deposition indice, as described in Section 3.3.

3.1 Ash deposition in an entrained flow reactor

3.1.1 Entrained Flow Reactor (EFR)

Since it is expensive to directly undertake the ash deposition experiments in full scale boilers, many experimental works have been undertaken in lab-scale entrained flow reactors. In this section, an entrained flow reactor, which is located at Imperial College, London, is described and the experimental data has been published [139]. Since the time-temperature history of fuel particles is significant in determining the transformation of inorganic constituents of fuel particles, the time–temperature history of fuel particles is one of the key parameters for the

design and operation of the EFR tests (temperature and velocity conditions in the furnace) to achieve a similar condition for the ash deposit formation as in a power plant. This has been carefully designed and operated in the experiments where a fuel particle with the residence time of approximately three seconds has been achieved [139].

Figure 3-1 shows a schematic geometry of the entrained flow reactor (EFR), which consists of four electrically heated furnaces with an inner diameter of 0.1 m and a length of about 5 m. The deposition probe is inserted into the cross section of the furnace as shown in Figure 3-1 and the ratio of the project area of the probe to the cross area of the furnace is approximately 21.7%. Three heating elements, including molybdenum disilicide ($MoSi_2$) for furnace 1, silicon carbide (SiC) for furnace 2 and two kanthal AF wire (FeCrAl alloy) for furnace 3 and 4, are employed to heat these furnaces and to provide a temperature gradient from 1650 °C at the top to 1200 °C at the bottom as shown in Figure 3-1 [75]. The burner consists of a primary inlet through which the pulverized coal and the primary air are fed, and a secondary inlet for the heated air. The pulverized coal particles are fed into the burner through a vibratory hopper system with an accurate control for the vibration amplitude, in order to operate the feeding system without blocking and provide a continuous feed without the detectable size separation [140]. The pulverized coal particles are entrained in the primary air and the adjustments to the primary and secondary airs ensure that the pulverised coal particles are established in the central region of the furnace [140]. Therefore, turbulent flow mainly occurs near the burner region and laminar flow takes place in the downstream of the furnace [140]. On the other hand, the pulverised coal particles could have a residence time of approximately three seconds in the EFR and half a second is spent in the furnace 1 (1650 °C) so that the fuel particles would have a similar time-temperature history in EFR as those in real boilers. The bottom of the EFR is used to cool the flue gas and the fly

ashes by using the water-cooled stainless steel jacket. Fly ashes are then collected by a primary cyclone and a second smaller cyclone [140].

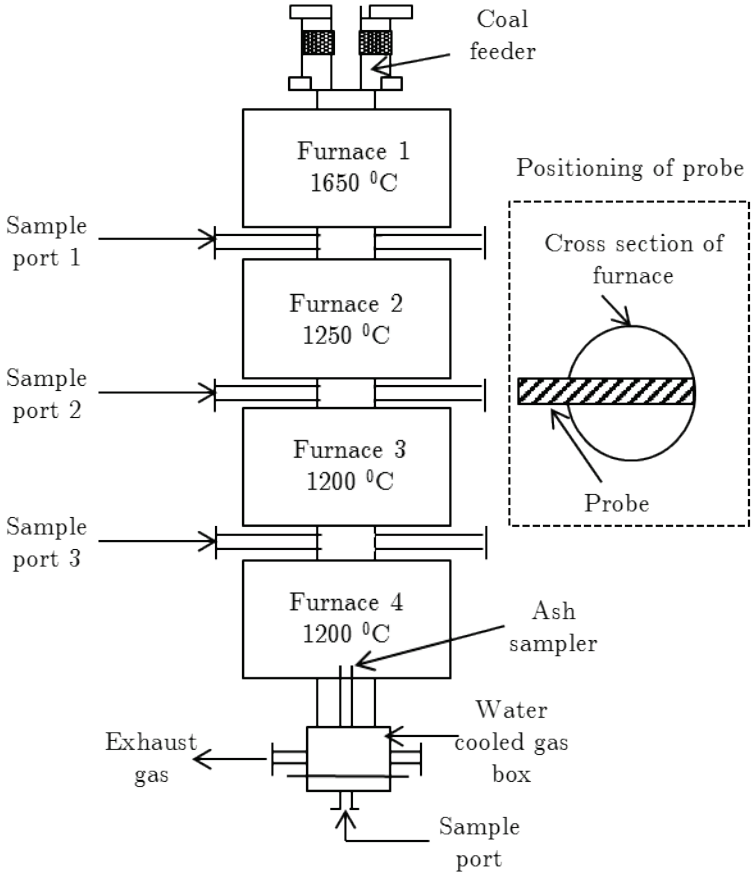

Figure 3-1 A schematic diagram of the geometry of the EFR based on [139, 140].

3.1.2 Ash deposition probe

An ash deposition probe should be capable of reproducing the ash deposit formation on a heat exchanger tube in boilers. Therefore, before introducing the design of the probe, it is important to understand the ash deposit formation on a heat exchanger tube in boilers. Figure 3-2 shows a schematic diagram of the typical structure of the deposition layers formed on the front surface of a heat exchanger tube. The initial layer is typically formed due to the thermophoresis of small particles and the condensation of alkali vapour compounds, such as NaCl,

KCl, Na_2SO_4, and K_2SO_4 [141-149]. This initial layer is usually porous and has a low thermal conductivity. The lower surface temperature of the tube enhances the growth of the initial layer and as a result the surface temperature of the deposit will increase to a point that can facilitate the melt and sintering to form a slag/sintered layer. The further growth of the slag/sintered layer is then mainly dictated by the inertial impaction of larger fly ash particles. The slag/sintered layer has a higher thermal conductivity compared to the initial layer and this is because of its dense structure and the more melt being formed at the layer, and the grain size is also larger than that formed at the initial layer [146-149].

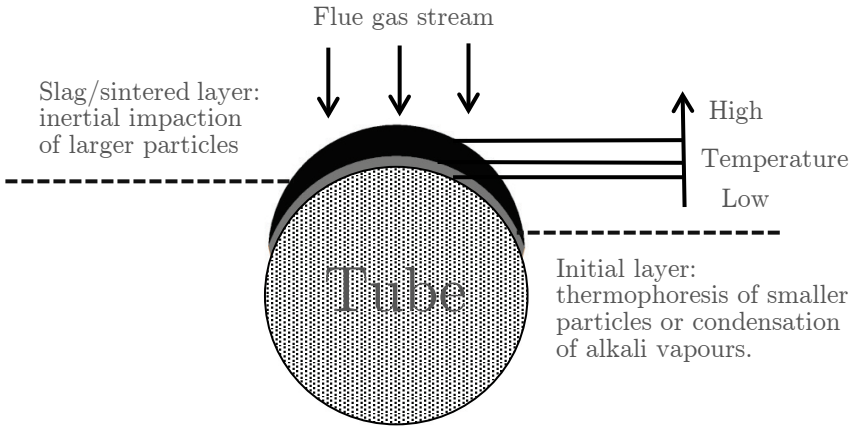

Figure 3-2 Schematic diagram of the main formation of the different deposition layers on the front surface of the cylindrical probe.

In the ash deposition experiments, an uncooled probe is used for collecting deposits and it is placed in the cross section of the furnace with a temperature about 1250 °C to simulate the deposit formation on the heat exchanger which is governed mainly by the cross-flow flue gas streams [84]. Therefore, the ash deposit formation is similar to that of the slag/sintered layer which is mainly dictated by the inertial impaction of the larger fly ash particles. The ash deposition probe is composed of the tube section and the sampling section, as shown in Figure 3-3. The tube section is used to hold the sampling section in the furnace and the

sampling section is used to collect the deposits. The sampling section of the uncooled ash deposition probe has an outer diameter of 17 mm and an inner diameter of 12.5 mm. The sampling section of the probe is made of mullite which has a similar surface composition to the coal ash [140]. In addition, mullite is resistant to the thermal shock which may affect the shedding of the deposits [140].

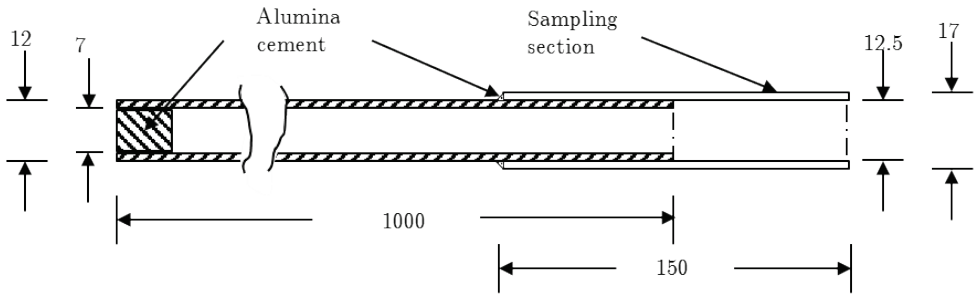

Figure 3-3 A schematic diagram of the ash deposition probe and the dimensions (mm) [140].

3.1.3 Case description

A range of scenarios of co-firing coal and biomass fuels have been experimentally investigated with the Imperial College EFR, where ash depositions were collected and subsequently analysed. The experimental data for the co-combustion of palm kernel expeller (PKE) with South African coal (SAC) has been employed, namely the SAC are blended with 0, 20, 40 and 60 *wt.*% of the PKE. The same EFR operational conditions as indicated in Figure 3-1 were employed for all four cases investigated. The fuel flow rate of 0.014 g/s, the primary air flow rate of 0.067 kg/s at 70 ^{o}C, and the secondary air flow of 1.167 kg/s at 300 ^{o}C [25] have been used for all the cases. Only the biomass additions were different to make PKE 0, 20, 40 and 60 wt.% of the fuel flow rate. The EFR was operated at a relatively low Reynolds number of approximately 400 so that near laminar flow conditions take place in the reactor although low turbulence occurs near the burner region [140]. The particle size of the SAC used ranged between 1 μm and 95 μm with a

mean diameter of 50 μm and the particle size of the PKE ranged between 105 μm and 355 μm, with a mean diameter of 130 μm [140, 150, 151]. Both the particle sizes are assumed to be spherical. The fuel properties, including proximate and ultimate analysis, as well as ash compositions, of both coal and PKE are summarized in Table 3-1 [139, 151, 152].

Table 3-1 Coal and PKE properties used in the calculations [139, 151, 152].

Ash composition (wt.%)			*Proximate analysis (wt.%)(ar)*		
	SAC	PKE		SAC	PKE
SiO_2	54.1	15.1	Volatiles	26.4	71.6
Al_2O_3	33.5	3.2	Fixed carbon	60.2	28.4
Fe_2O_3	3.1	5.3	Ash	12.1	4.2
CaO	4.1	10.7	GCV(MJ/kg)	27.3	18.7
MgO	1.3	12.0	*Ultimate analysis (wt.%)(daf)*		
K_2O	0.7	9.7	C	70.0	44.2
Na_2O	0.1	0.3	H	3.9	7.0
TiO_2	1.7	0.1	O	7.3	46.2
MnO	0.0	1.0	N	1.7	2.6
P_2O_5	1.1	42.7	S	0.6	0.5

As expected, PKE has much lower values of fixed carbon and ash content than the SAC but a higher volatile content. With regard to the ash composition, SAC is mainly composed of acid oxides (silicon and aluminium) whereas PKE is mainly composed of phosphorus, potassium and alkaline earth metals. Biomass with an ash rich in alkali metals and chlorine have shown a tendency to accelerate the process of deposition, slagging and fouling on the boiler surfaces [142-144]. The situation for phosphorus-rich biomass fuels is more complex and relatively few research works and data are available. In very general terms, high potassium and high phosphorus ashes tend to have a low fusion temperature and thus show a higher slagging tendency. However, depending on the overall compositions of the

fuel and ash, phosphorus can combine with the reactive alkali/alkaline species, e.g. potassium, calcium and magnesium, to form higher melting temperature phases [153, 154], and it can also influence the release of potassium during combustion, thus it can reduce the overall ash deposition tendency [153, 154]. In the experiments preformed at the EFR, an uncooled ceramic probe is employed and placed at the sample port 2 (which has a furnace temperature of approximately 1250 ^{o}C) to collect the ash deposits that represent a slag/sintered layer [139, 140, 155]. Therefore, in the current study, the initial layer is not modelled and the inertial impaction of particles is considered to be the main factor in controlling the ash deposition on the tube [25].

3.2 Ash deposition in a pilot-scale combustor

3.2.1 Pilot-scale combustor

The 300 kW_{th} combustion test facility is located at Zhejiang University, China and the experimental data has been published [148]. In order to reproduce the real combustion and the ash deposit formation on the water wall tube, the pilot-scale combustor has two main properties [148]: (i) it is a self-sustained combustor in order to provide the heat for the furnace, and (ii) a cooled ash deposition probe is used for the deposition experiments and the CCD imaging system is applied to monitor the dynamic deposit growth process.

Figure 3-4 shows a schematic diagram of the 300 kW combustion test facility [148]. It is consisted of (i) the coal feeding and preheating system, (ii) the combustion furnace with a swirling burner, (iii) the ash deposition sampling and imaging systems, and (iv) the post systems for flue gas and fly ash. The combustion furnace has an inner diameter of 0.35 m and a length of about 3.95 m. The swirl burner consists of a primary inlet through which the pulverized coal and the primary air are fed, and a secondary inlet for the heated air to maintain

a stable flame. The quench system is applied to cool the flue gas and fly ash in order to avoid the system damage. The cyclone and the bag filter are applied to capture the fly ash in order to avoid its emissions.

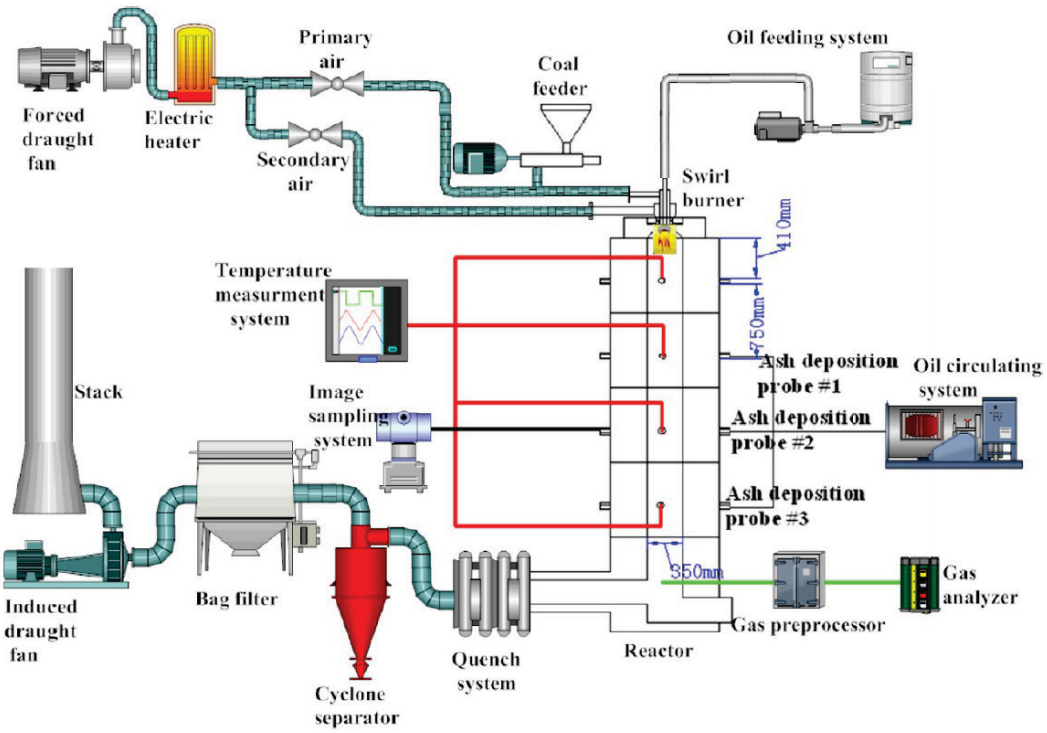

Figure 3-4 A schematic diagram of the 300 kW_{th} combustion test facility [148].

3.2.2 Ash deposit sampling and imaging system

It is important to understand the dynamic ash deposition behaviour on cooled heat exchanger tubes in order to design a suitable cooled ash deposition probe. Figure 3-5 shows a schematic diagram of ash deposition formed on a cooled heat exchanger tube. Ash deposits are mainly generated by the fine and coarse fly ash particles and the alkali/alkaline vapour after coal combustion. Due to the low tube surface temperature, the deposition due to the thermophoretic force and the vapour condensation may play an important role in the ash deposit formation in the initial stage of the ash deposit formation [142, 156, 157]. The deposition

surface temperature could rapidly increase due to the deposit growth and due to the rapid decrease in the heat flux to the deposition tube in the initial stage.

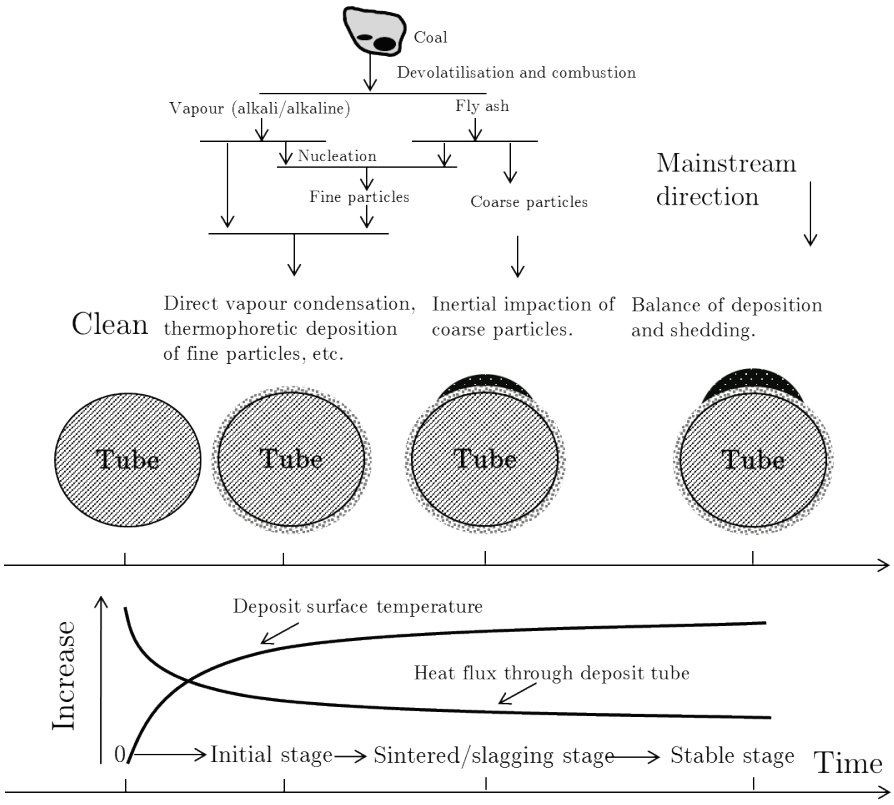

Figure 3-5 Schematic diagram of the main formation of the ash deposits on a cooled heat exchanger tube.

With the increase in the deposition surface temperature, the melting potential of the deposition surface is enhanced, which causes the sintering and slagging formation, the vapour condensation disappears and the contribution of the thermophoretic deposition on the arrival rate of ash particles declines [158]. At this stage, the deposition caused by the inertial impaction of coarse particles is the main deposition mechanism. Due to the higher thermal conductivity and lower heat flux through the tube than those in the initial stage, the deposition surface temperature increases slowly and this results in the slow decrease in the heat flux through the deposition tube. With the deposit growth, the shedding of the deposit is enhanced by the erosion, liquid flow at the deposit surface, gravity

shedding, etc.[59]. When the shedding rate is similar to the deposition rate, the deposit growth could stop or fluctuate and then the deposit height becomes stable [59]. The cooled deposit sampling system consists of the oil cooling section and the sampling section is shown in Figure 3-6.

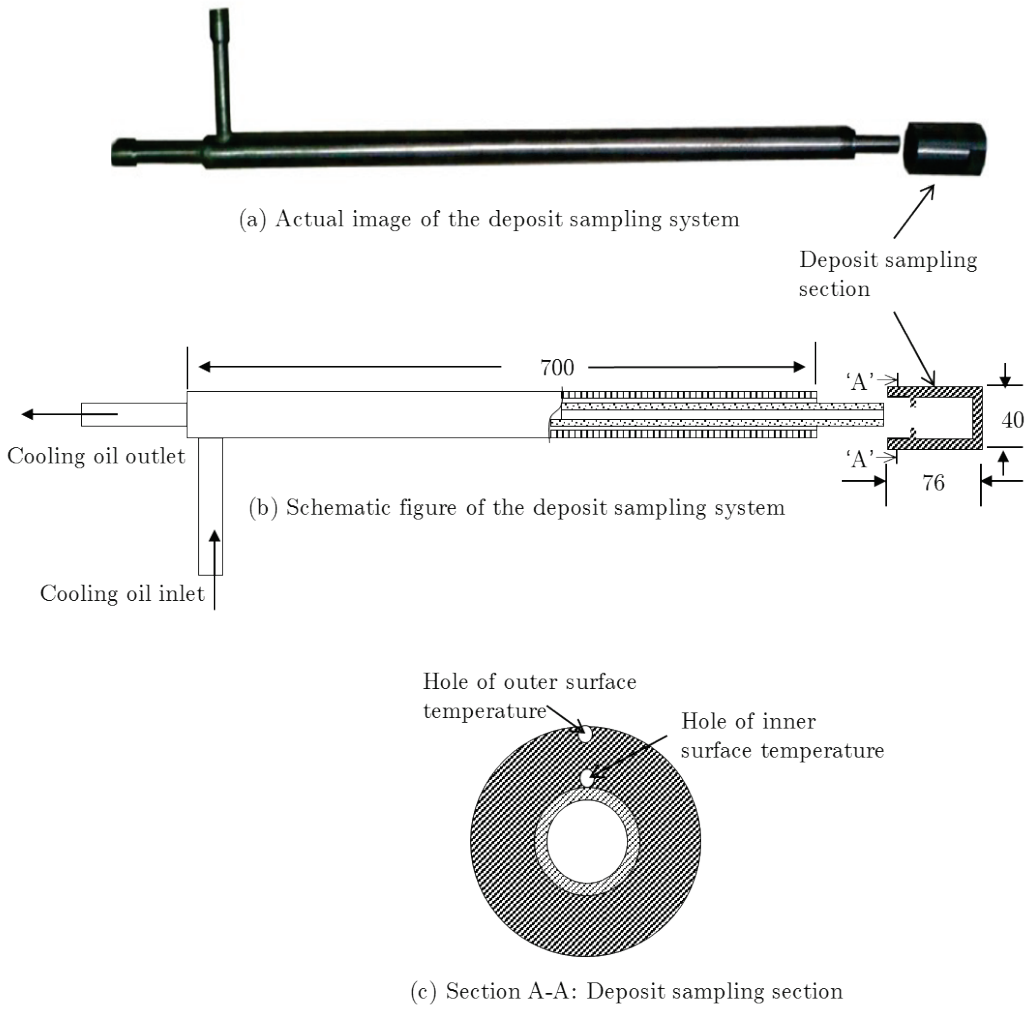

Figure 3-6 (a) Actual image of the deposit sampling system; (b) Schematic figure of the deposit sampling system; (c) Section A-A of the deposit sampling section (mm) [146-149].

The deposition probe is positioned at the cross section of the furnace and the ratio of the projected area of the probe to the cross area of the furnace is approximately 14.6%. The cooling oil with a temperature 230 °C flows into the outer pipe, passes the sampling section, flows back to the cooling section, and

then flows out the inner pipe [148]. The flow rate of the cooling oil can be adjusted through a valve in order to control the surface temperature of the sampling section. The sampling section, which is made of stainless steel (similar material as for the water wall tubes), has an outer diameter of 40mm and a length of 76 mm [148]. In addition, two K-type thermocouples are installed at the outer surface and inner surface of the sampling section in order to measure the outer surface temperature and inner surface temperature respectively [148]. By doing this, the heat flux, q, through the deposit and the sampling section tube can be determined by Equation (3-1). It is noted that, comparing to the uncooled ash deposition probe, the cooled ash deposition probe need a cooling system to control the surface temperature of the probe and thermocouples are often installed in the probe to monitor the variance of the probe inner/outer surface temperatures.

$$q = \frac{k_{steel}(t_2 - t_1)}{r ln(\frac{r_2}{r_1})} \tag{3-1}$$

where k_{steel} with a value of 48 W/(K*m) is the thermal conductivity of the stainless steel probe, t and r are the measured temperature by the thermocouples and the radius of probe, Digitals in the t and r (1 and 2) represent the properties for inner thermocouple and the outer thermocouple, respectively.

In order to dynamically monitor the deposit growth, a CCD imaging system is applied, which consists of the CCD camera, the camera lens, the protective tube and the camera shield, as shown in Figure 3-7 [146-149]. The protective tube and camera shield are used to avoid the high temperatures and the fouling of the small particles on the camera lens. The process to determine the deposit growth is as follows [146-149]: (i) the deposit images are recorded by the CCD imaging system; (ii) the original images are processed to be 24-bit images through the Matlab software; (iii) the average deposit height can be determined from the pixel numbers of the edge images (deposit probe and the deposit thickness) through

the edge detection and the algorithm of Hough transform. In this study, the deposit thickness obtained from the CCD imaging system is used to compare with the CFD prediction results of the deposit thickness. The simple procedure of an ash deposition experiment in the furnace is as follows [146-149]: (i) Start up the furnace and operate the furnace to reach the stable status; (ii) Install both the CCD imaging system and the ash deposition sampling system; (iii) Record the ash deposit growth for about three hours; (iv) Collect the ash deposits on the probe and shut down the furnace.

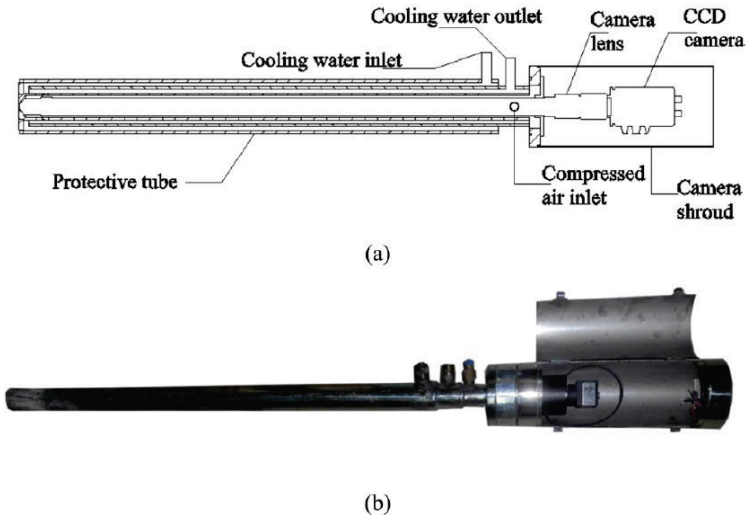

Figure 3-7 (a) Schematic diagram of the Charge Coupled Device (CCD) imaging system; (b) Photograph of the CCD imaging system [146-149].

3.2.3 Case description

The ash deposition data of Zhundong (ZD) lignite combustion in the combustion facility under three different furnace temperatures (1100 °C, 1270 °C, and 1320 °C) has been employed. Table 3-2 shows the properties of the ZD coal, including the proximate and ultimate analysis, as well as the major ash composition of the ZD coal [148]. Table 3-3 shows the mineral compositions of the low temperature ZD coal ash [148]. The low temperature coal ash is prepared by ashing the finely ground coal at a temperature of 60-70 °C using the plasma asher [159].

As expected, the ZD coal has a high volatile content and low-medium ash yield. The ash analysis is dominated by silicon (Si), calcium (Ca), sodium (Na), aluminium (Al), iron (Fe) and magnesium (Mg) oxides, accounting for almost 96% of the total ash composition. In particular, the low temperature ash is rich in sodium (Halite) and calcium (Calcite and Anhydrite). Additionally, quartz and hematite are present in the ash sample. The ZD coal rich in Alkali and Alkaline Earth Metal (AAEM) has shown a high tendency to cause ash slagging, fouling and corrosion in the radiation and convection sections of the boilers [63, 69, 145]. It should be noted that the present research focuses on the deposition probes placed in the central region of the furnace. It is assumed that the discrete parcels of particles are uniformly distributed [85, 132, 133]. The flow rate of the ash particles of 1.153 g/s and the velocity of the flue gas and particles of 2.8 m/s have been used for all the three cases from the experiments [148]. The ash particle size is ranged between 1 μm and 60 μm with a mean diameter of 16 μm [148]. It should be noted that the prediction of the ash deposition behaviour is focused on the first two hours in this study, where the shedding is less important [148].

As expected, the ZD coal has a high volatile content and low-medium ash yield. The ash analysis is dominated by silicon (Si), calcium (Ca), sodium (Na), aluminium (Al), iron (Fe) and magnesium (Mg) oxides, accounting for almost 96% of the total ash composition. In particular, the low temperature ash is rich in sodium (Halite) and calcium (Calcite and Anhydrite). Additionally, quartz and hematite are present in the ash sample. The ZD coal rich in Alkali and Alkaline Earth Metal (AAEM) has shown a high tendency to cause ash slagging, fouling and corrosion in the radiation and convection sections of the boilers [63, 69, 145]. It should be noted that the present research focuses on the deposition probes placed in the central region of the furnace. It is assumed that the discrete parcels of particles are uniformly distributed [85, 132, 133]. The flow rate of the ash

particles of 1.153 g/s and the velocity of the flue gas and particles of 2.8 m/s have been used for all the three cases from the experiments [148]. The ash particle size is ranged between 1 μm and 60 μm with a mean diameter of 16 μm [148]. It should be noted that the prediction of the ash deposition behaviour is focused on the first two hours in this study, where the shedding is less important [148].

Table 3-2 Fuel properties of the ZD coal [148].

Ash composition (wt.%)		*Proximate analysis (wt.%)*	
SiO_2	35.08	Volatiles (*db*)	32.79
Al_2O_3	14.04	Fixed carbon (*db*)	52.91
Fe_2O_3	6.07	Ash (*db*)	12.3
CaO	27.78	HHV(MJ/kg)	54.01
MgO	4.73	*Ultimate analysis (wt.%) (db)*	
K_2O	0.48	C	64.07
Na_2O	8.31	H	3.58
TiO_2	0.71	O	19.22
SO_2	2.8	N	0.65

Table 3-3 Mineral compositions of low temperature ash (*wt%*) [148].

Quartz (SiO_2)	Calcite ($CaCO_3$)	Halite (NaCl)	Hematite (Fe_2O_3)	Anhydrite ($CaSO_4$)
28.0	27.6	24.7	13.4	6.2

3.3 Ash deposition data in utility boilers

In order to develop and validate the new ash deposition indice, ash deposition data from 30 sets of coals/blends combustion in utility boilers are applied. Two representative cases of utility coals have been investigated: (i) Case 1 is the Eastern US bituminous coals/blends combusted in T-fired boilers; (ii) Case 2 is the Western US sub-bituminous or lignite coals/blends combusted in opposed-wall boilers. Case 1 contains 13 sets of coal combustion data (including data for

6 sets of coal blends); Case 2 contains 17 sets of coal combustion data (including data for 10 sets of coal blends). The range of coals and ash properties for the 30 sets of US coals/blends studies are presented in Table 3-4. Bituminous coals have a higher Fe_2O_3, SiO_2 and Al_2O_3 contents compared to low rank coals but a lower content CaO and MgO contents. Both bituminous and sub-bituminous coals have low Na_2O and K_2O contents contrary to lignites that have higher levels of Na_2O. Slagging observations in boilers are evaluated by using not only the field performance data in the radiation and convection sections based on FEGT, soot blowing frequency increase, heat transfer rate, etc., but also periodic visual examinations of the deposit strength/ease of removal. The degrees of the slagging observations, ranging from no slagging to severe slagging, are represented using the values from 0 to 1. The details of the ash properties and the slagging observations for the 30 sets of data are presented in Appendix A. Also the field slagging observations can be classified into four groups: low slagging < 0.4; $0.4 \leq$ medium slagging ≤ 0.6; $0.6 <$ high slagging ≤ 0.9; severe slagging <0.9.

Table 3-4 Ash composition ranges for the US coals.

	Bituminous		Low rank coal			
			Sub-bituminous		lignite	
	Min	Max	Min	Max	Min	Max
SiO_2	44.8	55.9	32.2	41.8	34.3	37.7
Al_2O_3	20.5	28.7	16.4	22.5	16.7	18.2
Fe_2O_3	6.2	22.1	4.0	14.7	5.3	5.6
CaO	1.4	5.6	13.8	21.9	16.7	18.6
MgO	0.7	1.4	2.8	6.5	3.7	4.0
K_2O	1.2	2.6	0.5	1.5	0.3	0.5
Na_2O	0.3	1.3	1.0	1.3	6.3	6.7
Ash content	7.5	10.6	4.9	6.6	3.9	4.6
Sulphur	0.4	2.7	0.3	1.1	0.3	0.4
LHV(MJ/kg)	26.4	30.3	20.6	24.3	20.6	21.6

Chapter 4: Steady CFD prediction of ash deposit formation in an entrained flow reactor

Summary

This chapter presents the methodology and the results of the steady CFD predictions of ash deposit formation for the co-combustion of South African coal (SAC) and palm kernel expeller (PKE) in an entrained flow reactor based on modelling particle impaction and sticking. The numerical related errors, caused by interception and the improper resolving of the flow-field within the boundary layer near the deposition surface, are investigated. In order to minimize the numerical related errors without excessive meshing, a new revised particle impaction model has been developed and accomplished using an impaction correction factor. The particle sticking is predicted based on the molten fraction results that have been obtained from the chemical equilibrium calculations using the chemical fractionation data in order to consider the short residence time of fly ash particles. The simulation results of the deposition efficiency show that a reasonable coarse mesh, coupled with the revised particle impaction model, is suitable to accurately resolve the particle impaction without using a prohibitive large meshing size.

4.1 Introduction

Co-combustion of biomass with coal has been used as a near term measure to reduce CO_2 emission from coal fired power plants [160, 161]. Currently, co-firing

10-20% (thermal) biomass with coal has been widely used in power stations in the UK and Europe and a higher co-firing rate is also used. Further, some power stations, such as the Drax in the UK, are being converted to firing 100% biomass. With the recent announcement of the new EU targets of reducing gas emissions, fuel flexibility is likely to be one of the key factors influencing the operation of the power stations in the future, and the uses of various biomass and waste for power in the EU are expected to substantially increase. Currently most large scale power stations are using relatively clean biomass, such as wood pellets, and to some extent straw, olive stones and palm kernel expeller (PKE). An addition of up to about 10-20% biomass has only moderate effects on the ash deposition in the furnace. However, with an increased co-firing rate and the use of a wide range of biomass sources, ash related problems are ranking high on the list of significant operational constraints in co-firing power plants [62, 118]. Ash deposition reduces the efficiency of the heat transfer through the water walls and heat exchangers and causes corrosion of boiler tubes, which may lead to reduced generating capacity and unscheduled outages [65]. Therefore, an improved understanding of the ash deposition in firing various types of biomass is imperative for an efficient boiler operation and optimization in the future [162].

The optimum biomass co-firing rate in coal-fired boilers has still been mainly determined by experiments up to now [62]. Computational Fluid Dynamics (CFD) has been widely used for solid fuel combustion simulations and various sub-models have been developed for predicting ash depositions in lab-scale test facilities as well as for full scale boilers [25, 50, 62, 65, 82, 118, 124, 162-166]. Considerable progress has been made in the last decades in developing ash deposition models for CFD simulations [62, 65, 84, 89, 93, 118, 167], and more detailed and accurate sub-models for combustion, fuel/ash particle transport, and sticking and deposition rate predictions have been developed [118, 167]. Typically, Lagrangian methods are employed to compute the trajectories of ash

particles, coupled with an Eularian method for the flow and gaseous phase reactions, where the inertial impaction of the particles is often considered as the only or main mechanism for ash deposit formation.

This chapter aims to develop an improved ash deposition CFD model through (i) a new revised particle impaction model to minimize the numerical related errors with an affordable number of computational mesh, and (ii) an appropriate particle sticking model based on the ash chemistry and the particle momentum for the PKE where there is relatively a scarce amount of data available. The model developed has been tested using the experimental data from Imperial College's entrained flow reactor [139, 140], where PKE with the high level of phosphorus has been considered.

4.2 Mathematical models

4.2.1 Combustion models

The combustion of coal and biomass is modelled in a combined Eularian-Lagrangian frame of reference where the volatile combustion is modelled in the Eularian frame of reference and the fuel/ash particles are tracked in a Lagrangian frame of reference. The single kinetic rate model was employed for the devolatilisations of the coal and biomass, where the rate of devolatilisation depends on both the temperature and the volatile content of the particles [160, 168]. The values of the Arrhenius rate constants, pre-exponential factor and activation energy that have been previously used and validated are used [160, 166, 168], as shown in Table 4-1. The combustion of the volatile gases was modelled using the Eddy Dissipation Model with a two-step global reaction mechanism [79]. Also it is assumed that the particle size remains constant, while the particle density reduces during the release of the volatile gases from the fuel particles [62, 168].

Table 4-1 The combustion properties of SAC and PKE [57, 160, 163, 168-170].

Fuel	Devolatilisation		Char combustion	
	A (1/s)	E_a (J/kmol)	A_i (kg/m^2-s-Pa)	E_{ai} (J/kmol)
SAC	$3.8*10^{14}$	$2.3*10^{8}$	15.3	$1.52*10^{8}$
PKE	$6.13*10^{13}$	$2.5*10^{8}$	0.658	$7.48*10^{7}$

Char combustion was modelled with the intrinsic char combustion model (see Section 2.2.3.2), which assumes that the order of the surface reaction is unity and that the surface reaction rate takes into consideration the effects of both the chemical reaction and bulk diffusion rates [160]. The same model constants were employed as [79, 153, 169], as shown in Table 4-1. In the Smith intrinsic model, the variation of the char particle size and density is related to the fractional degree of burnout, U, in terms of the burning mode, α , as follows [50, 169]:

$$\left(d_p/d_{p,0}\right) = (1-U)^{\alpha} \tag{4-1}$$

$$U = [1-(m_p/m_{p,0})] \tag{4-2}$$

where d_p and m_p are the char particle size and mass, respectively, and the subscript zero refers to the initial conditions (at the start of the char combustion). For the coal, the value of α used was 0.25, and this corresponds to a decrease in both the particle size and density during combustion [50, 169]; for the biomass, it is believed that the particles would most likely maintain their original size during combustion, and therefore the value of zero was used for α, and this corresponds to a constant size but with a decreasing density of the particle during combustion [171].

The trajectories of the coal and biomass particles are governed by the particle momentum equation, which is a balance of the drag, gravity, and other body forces as formulated in the following equation [50, 172]:

$$\frac{d\vec{v}_p}{dt} = \frac{18\mu_g}{\rho_p d_p^2}\frac{C_D Re_p}{24}\left(\vec{v}_g - \vec{v}_p\right) + \frac{\vec{g}(\rho_p - \rho_g)}{\rho_p} + \vec{F} \tag{4-3}$$

where $\vec{v}$, ρ, μ and d are the velocity, density, viscosity and diameter of the particles, respectively; the subscripts p and g refer to the particle and gas, respectively, C_D is the drag coefficient, and $\vec{F}$ is the other body forces, such as the thermophoretic force, virtual mass force, etc. The thermophoretic force, which is caused by the temperature gradient in the gas stream close to a solid depositing surface may be neglected when modelling a heavily deposited surface such as the slag/sintered tube surface where a high surface temperature exists. The virtual mass force, which is due to the acceleration of the fluid around the particle, may also be ignored when the density of the particle is much greater than the density of the fluid.

The effect of fluid turbulence on the particle trajectories was considered by decomposing the instantaneous gas velocity, $\widetilde{u}$, into time-mean and fluctuating components $\overline{u}$ and u' and solved using the Discrete Random Walk (DRW) model. Assuming isotropic turbulence, the fluctuating component can be valuated using the turbulent kinetic energy, k_t. It is assumed that the fluctuating velocity prevails for a time period equal to the life time of the fluid eddy that the particle is traversing [11]. The time, τ, can be approximated by Equation (4-6) in terms of the turbulent kinetic energy and the dissipation rate k_t and ε_t, see Equation (4-6):

$$\widetilde{u} = \overline{u} + u' \tag{4-4}$$

$$u' = \varsigma\sqrt{\overline{u'^2}} = \varsigma\sqrt{2k_t/3} \tag{4-5}$$

$$\tau \cong C_L(k_t/\varepsilon_t) \tag{4-6}$$

where ς is a normally distributed random number, and C_L is the time scale constant. Since no local information on the velocity and pressure are available, the distribution of the impacting particles is used to validate the turbulent effect on particle dispersion modelling since the particle dispersion can affect the particle impaction flux distribution. With the DRW model, only a few particles impact on the middle section of the probe surface and particles mainly expand to impact on each side of the front surface of the probe, and some of the particles will impact on the furnace wall (as shown in Figure 4-1 and Figure 4-2). Without the DRW model, the particle impaction is located mainly in the middle section at the front surface of the probe; no particles will impact on the furnace wall (as shown in Figure 4-1 and Figure 4-2). In the experimental data, no deposits are formed on the furnace wall and the ash particles were restrained to remain in the central part of the furnace tube [139, 140], and this gives rise to the effect of particle turbulent dispersion being small in the experimental investigations. Therefore, the mean fluid flow velocity is considered in the particle tracking calculations and the effect of turbulent particle dispersion is neglected [62].

In order to better resolve the particle trajectories in the gas flow boundary layer, the boundary layer has to be modelled carefully [84] and the enhanced wall treatment was used. If the near-wall mesh is fine enough to resolve the fluid viscous sublayer, then the enhanced wall treatment can be similar to the traditional two-layer zonal model [173]. If a coarse mesh is used together with a wall-function, the accuracy of the near wall modelling will not significantly be reduced when the enhanced wall treatment is used, where a single wall law for

the entire wall region is generated by blending the linear (laminar) and the logarithmic laws of the wall [174].

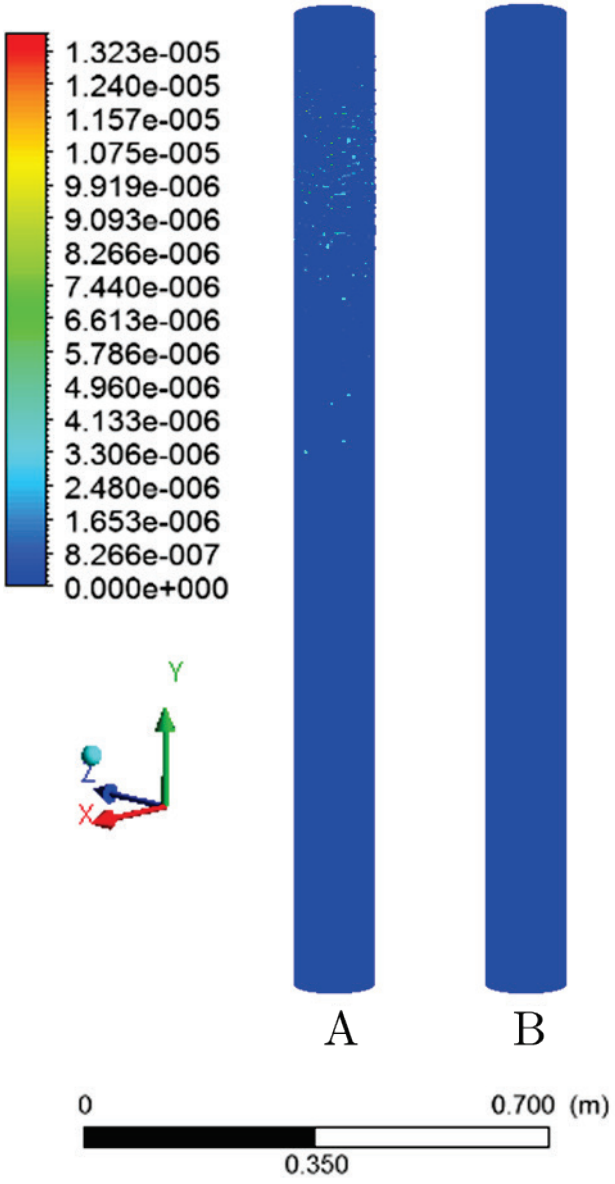

Figure 4-1 Particle arrival rate on the deposition probe: A, with the DRW model; B without the DRW model.

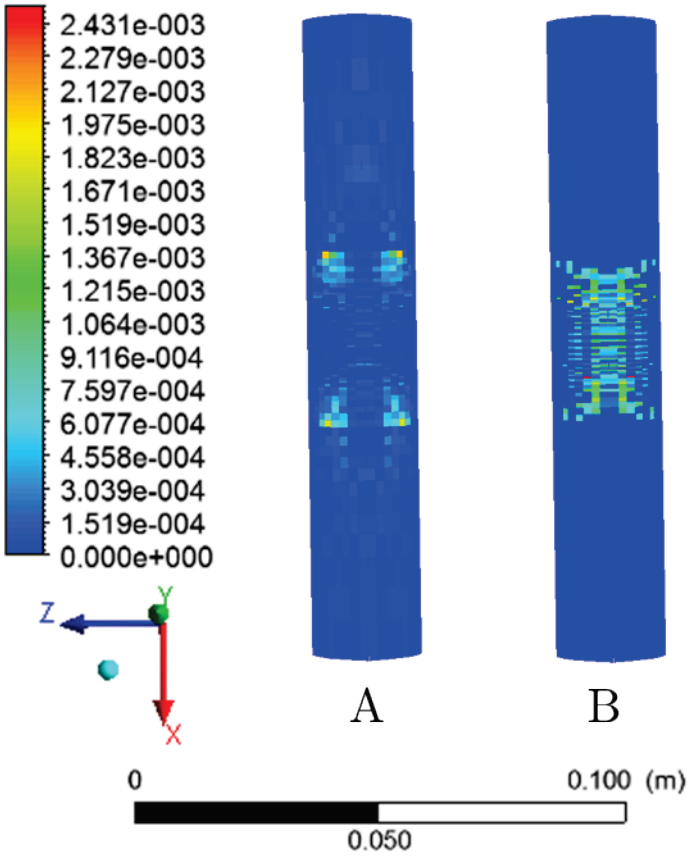

Figure 4-2 Particle arrival rate on the furnace wall 1: A, with the DRW model; B without the DRW model.

The energy balance equation of the particles, which are solved along the trajectories of the particles in order to obtain the corresponding particle temperatures, is given as follows [50, 160, 165]:

$$m_p c_p \frac{dT_p}{dt} = hA_p\left(T_\infty - T_p\right) + \varepsilon_p A_p \sigma\left(\theta_R^4 - T_p^4\right) - Q_p \tag{4-7}$$

where m_p, c_p, T_p, A_p, and ε_p are the mass, specific heat, temperature, surface area and emissivity of the particles, T_∞ is the gas temperature, σ is the Stefan–Boltzmann constant, and θ_R is the radiation temperature. Q_p, which is the latent heat or the heat of reaction is determined by the following equations:

$$Q_p = \begin{cases} 0, & \text{if under the step of inert heating or cooling} \\ \dfrac{dm_p}{dt} h_{fg}, & \text{if under the step of devolatilisation} \\ f\dfrac{dm_p}{dt} H_r, & \text{if under the step of char combustion} \end{cases} \quad (4\text{-}8)$$

where h_{fg} is the latent heat, f is the fraction of the heat absorbed by the particles, and H_r is the heat of reaction released by the surface reaction. The radiative heat transfer was modelled using the Discrete Ordinates model and the gas absorption coefficient was calculated with the domain based weighted-sum-of-gray-gases model (WSGGM).

4.2.2 Revised particle impaction model

Due to the influence of the gas flow, not all the particles carried by the gas stream will impact on the depositing surface. The amount of ash particles that may hit a depositing surface can be estimated by the particle impaction efficiency, which is defined as the percentage of particles of given size in the projected area of the deposition surface in the upstream gas flow that can impact on the deposition surface [84]. The impaction efficiency is dependent on the particle Stokes number, St, that is defined as follows for particle impaction on a circular cylinder[24, 175]:

$$St = (\rho_p d_p^2 u_p)/(9\mu_g D) \quad (4\text{-}9)$$

where ρ_p, d_p, u_p, and μ_g are the particle density, particle diameter, bulk particle velocity and gas dynamic viscosity, respectively, and D is the outer diameter of the deposition pipe. Particles with larger Stokes number are less likely to be affected by the gas flow and more likely to impact on the surface of the deposition pipe; however, particles with smaller Stokes number follow more closely to the fluid streamlines and are less likely to impact on the surface [48]. Therefore, accurately predicting the gas flow in the boundary layer near the deposition surface is very important for accurately predicting the particle impaction

efficiency, in particular for particles with a small Stokes number. However, this often requires an extremely fine computer mesh close to the deposition surface in order to resolve the flow boundary layer accurately and this is often prohibitively expensive computationally for modelling real combustors and industrial boilers. In the most cases, as seen in most publications, a reasonably coarse mesh is employed to satisfy the mesh independency requirement for the bulk of the gas flow. However, with this reasonably coarse mesh, the particle impacting efficiency is often over-estimated [12, 17], since the trajectory of small ash particles close to a deposition surface is very sensitive to the details of the boundary layer flow, leading to errors in the deposition rate prediction.

Further, during the particle tracking in CFD, the particle is usually treated as a point in the computational domain and whether a particle hits a wall or not is determined by the position of the center of the particle without considering the effect of the size of the particle [84, 120]. However, in reality, a particle will hit the surface with a distance equal to the particle radius away from the centre of the particle [84, 120]. This interception effect of the particle size on the impaction efficiency can be described using the interception parameter, R_i, defined as follows [84, 120]:

$$R_i = d_p/D_{probe} \tag{4-10}$$

where d_p and D_{probe} are referred to the diameters of the particles and the deposition probe, respectively. Clearly the larger is the ratio of the particle diameter to the tube diameter, the larger is the interception. In order to remove the errors resulting from using a coarse computational mesh in the boundary layer and from the particle interceptions, an impaction correction factor, F_i, may be introduced which can be defined as the ratio of the real particle impaction efficiency and that predicted using a reasonably coarse computational mesh for a

particular particle stream, i.e. for the ith particle stream, $F_i = I_{real,i}/I_{coarse,i}$. The real impaction efficiency $I_{real,i}$ can be estimated by using a small computational domain that only contains part of the furnace that is close to the superheat tubes where extremely fine meshing may be used. The boundary conditions for flue gas and ash particle flows may be taken from the existing results obtained using the reasonably coarse computational mesh. If the interception parameter is also considered, then the impaction correction factor may be calculated using the following equation:

$$F_i = (I_{fine,i} + R_i)/I_{coarse,i} \tag{4-11}$$

where $I_{fine,i}$ is the predicted particle impaction efficiency from a well resolved boundary layer, $I_{coarse,i}$ is the impaction efficiency from a reasonably coarse mesh, and R_i is the interception parameter, of the i th particle stream; This impaction correction factor can be used to correct the CFD predicted mass flux, i.e. the arrival rate of the particles to the deposition surface using a reasonably coarse computational mesh in the CFD simulation as illustrated in Figure 4-3. Therfore, a reasonably coarse computational mesh can be used to predict the particle impaction efficiency through using the revised particle impaction mdoel. The overall effect of the interception parameter on the impaction efficiency, O_{IP}, can be defined as follows:

$$O_{IP} = \left[\sum_{i=1}^{n}(MF_i \bullet R_i)\right]/\eta_o \tag{4-12}$$

where MF_i is the mass fraction of each particle stream, η_o is the overall impaction efficiency which is defined as the ratio of the arrival rate of the particles to the mass flow of particles in the upstream flow.

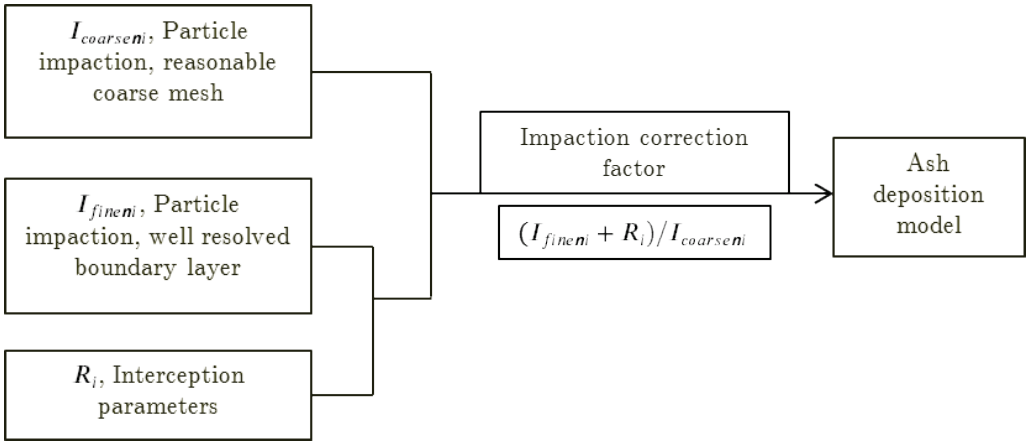

Figure 4-3 Schematic of the methodology for the revised particle impaction model.

In order to validate the proposed approach for improving the accuracy of the particle impaction efficiency calculations, particle impactions on a two-dimensional cylinder have been simulated and compared with the results from the direct numerical simulation (DNS) reported by Haugen and Kragset [120]. Figure 4-4 shows the flow configuration and boundary conditions employed. A computational domain of 6D×12D is employed with the tube being placed in the centre of the domain. The tube diameter D=40mm. Gas (viscosity=4.6×10^{-5} Pa.s and density=0.245 kg/m^3, which represent a stream of hot flue gas under 1500 K [84]) enters into the domain with a given free stream velocity, U_0. Two velocities, U_0= 0.47 m/s and 7.91 m/s (corresponding to a Reynolds number, Re_t, based on deposition tube diameter, approximately 100 and 1685, respectively) have been considered to represent the low velocity condition in a drop tube furnace and a high velocity condition in real boilers . In order to obtain the impaction efficiency with a well resolved boundary layer mesh, i.e. I_{fine}, RANS simulation with a fine mesh of approximately 400 nodes ($Re_t = 100$) and 1600 nodes ($Re_t = 1685$) on the tube circumference have been employed as suggested by [84, 120, 176].

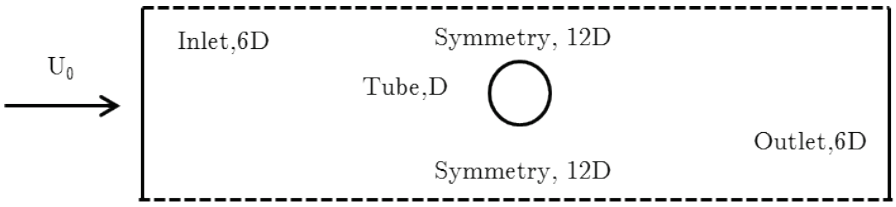

Figure 4-4 The flow configuration and boundary conditions of the 2D computational domain.

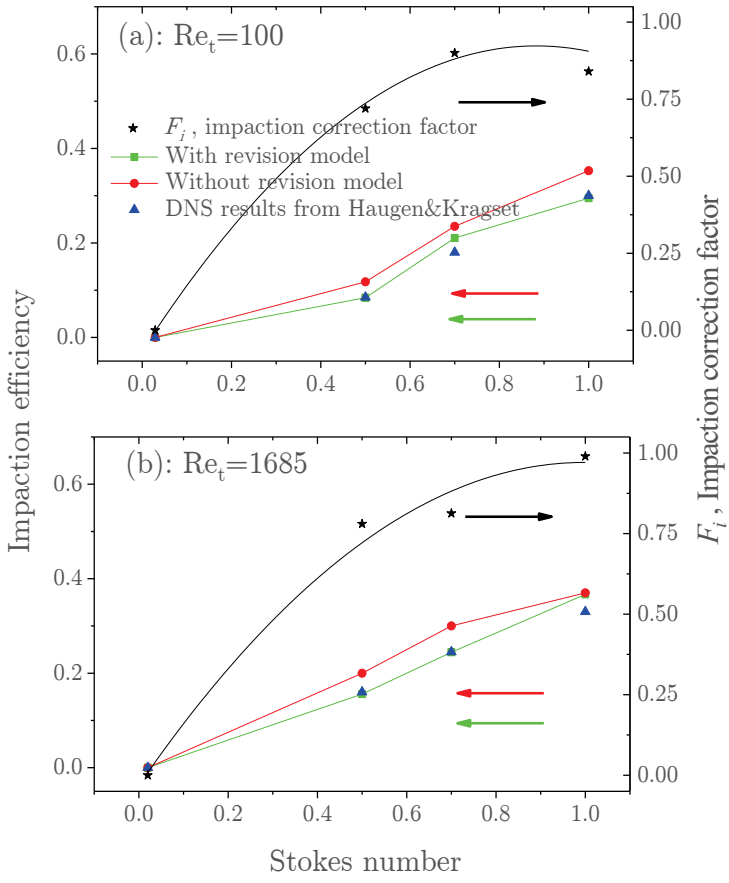

Figure 4-5 The impaction correction factor and comparisons of the predicted particle impaction efficiency using a coarse mesh and the DNS, with and without particle impact correction when (a): Re_t=100 and (b): Re_t=1685 as a function of the Stokes number.

Figure 4-5 compares the predicted particle impaction efficiencies with and without the corrections for the two cases investigated with the DNS results obtained from [120]. Reasonably coarse meshes with approximately 140 nodes

and 180 nodes on the circumference of the tube for the $Re_t = 100$ and $Re_t = 1685$ cases, respectively, have been employed. Figure 4-5 shows that the impaction correction factor increases with increasing particle Stokes number and the value of the correction factor is approaching one when the Stokes number is greater than 1. Also, it can be found that applying the revised particle impaction model can substantially reduce the errors in the predicted particle impaction efficiency when a coarse mesh is used, compared with the results from the DNS.

4.2.3 Particle sticking model

After the particles reach a deposition surface, not all the arriving particles will stick to the surface. If the particle, or the deposition surface, is sticky then the particle may deposit [164]. On the other hand, particles with high impact energy may rebound back into the gas flow after hitting the wall [93, 163]. The sticking efficiency of the impacting particles is defined as the ratio of the number of particulates depositing on the surfaces to the number of the particles impacting on the surfaces [162]. There are at least two factors that influence the particle sticking efficiency, namely, (i) whether a particle is sticking or not, and (ii) whether the particle will rebound back from the surface. In this work, the stickiness of the particles was determined by the degree of melting of the particle, i.e. the molten fraction of the particles [86] calculated based on the thermodynamic equilibrium of the particles. Since not all ash components can reach chemical equilibrium when arriving at the deposition surface, in particular for EFR test conditions [113], the chemical fractionation analysis data is employed from a stepwise leaching of the relevant fuels in order to consider the short residence time of the ash particles in the reactor [113]. The chemical thermodynamics software package FactSage 6.4 is employed to perform the thermodynamic equilibrium calculations based on the minimization of the Gibbs free energy from the system subject to the mass balance constraints [177, 178].

In the thermodynamic equilibrium calculations, the gas composition N_2, O_2, CO_2 and H_2O are taken from the CFD predictions and their amounts are dictated by the inlet air/fuel ratio. The reactants in the ash are obtained from the ash analysis shown in Table 3-1 and the chemical fractionation data from [179, 180] for both SAC and PKE as shown in Table 4-2. Potassium and sodium can be completely leached with chemicals such as water and acetate for PKE whereas only part of sodium can be leached for SAC. Phosphorus is more difficult to be leached for both PKE and SAC. The amount of the non-reactive fraction of the inorganic mater in the ash particles which can reach equilibrium during combustion is difficult to determine through the experiments and this amount is typically in the range 0 to 25% depending on particle size, temperature and residence time, etc. [93, 113, 180-182]. Hence, a middle value of 10% was chosen [180]. For particles impacting a slagging/sintered surface, the value for the non-reactive fraction is less significant in predicting the overall sticking efficiency than impacting on a new tube surface.

Table 4-2 Chemical fractionation (percentage) of ash components leached from fuels [179, 180].

	SiO_2	Al_2O_3	Fe_2O_3	CaO	MgO	K_2O	Na_2O	TiO_2	P_2O_5
SAC	0	0	0	70	0	2	40	0	0
PKE	1	0	0	5	3	100	100	0	3

The calculations were performed for a temperature range between 1500 K and 1750 K at a temperature interval 20 K and at atmospheric pressure. The possible products selected are the entire compound species (ideal gases and pure solids) from the ELEM, FToxid, FTsalt and FACTPS databases. The slag model chosen in the calculations was the 'SLAGC' with possible 2-phase immiscibility to consider the relative high amount of phosphorus in the ash [183, 184], which covers oxide liquid solutions of MgO, FeO, Na_2O, SiO_2, TiO_2, Ti_2O_3, CaO, Al_2O_3,

etc., and phosphates as $Na_3(PO_4)$, $Ca_3(PO_4)_2$, $Mg_3(PO_4)_2$, $Fe_3(PO_4)_2$, K_3PO_4 and $FePO_4$.

As mentioned earlier, whether an impacting particle actually sticks or not depends on whether the particle rebounds from the deposition surface or not, and this depends on the deformation after the particle impacts on the surface and the momentum of the particles [25]. The particle energy balance model, developed by Mueller et al. [93] and Mao et al. [185], was employed to assess the excess energy , E_x, which is the excess rebounding energy particles possess after impaction and can be calculated using the following empirical formula [93, 163, 185]:

$$E_x = \frac{D_m{}^2}{4}(1 - cos\alpha_c) - \frac{3D_m{}^{2.3}}{25}(1 - cos\alpha_c)^{0.63} + \frac{2}{3D_m} - 1 \quad (4\text{-}13)$$

where D_m is the ratio of the maximum deformation in the particle diameter to the actual particle diameter, and α_c is the static contact angle of the particle. D_m is related to the particle Weber number, We, and the Reynolds number, Re, as follows:

$$D_m = (12 + We)^{0.5} \bullet [3(1 - cos\alpha_c) + 4(We/Re^{0.5})]^{0.5} \quad (4\text{-}14)$$

$$We = (\rho_p U_n^2 d)/\sigma \quad (4\text{-}15)$$

$$Re = (\rho_p U_n d)/\mu_p \quad (4\text{-}16)$$

where U_n is the impact velocity component normal to the impact surface, and σ is the particle surface tension. If the excess energy of a particle is large enough, $E_x > 0$, the particle will rebound off the deposition surface, otherwise the particle will stick.

4.3 EFR CFD model set up and results

4.3.1 Model set up

Since EFR was operated at a relatively low Reynolds number of approximately 400, [140], the Transition SST turbulence model which is applicable to flows with the low Reynolds number, was chosen to simulate the gas flow [186]. The adiabatic condition has been employed at the surface of the deposition probe to consider its uncooled condition. The commercially available CFD software package ANSYS Fluent version 15.0 has been employed to perform the basic calculations of the coal and biomass combustion incorporating the User Defined Functions and Memories in order to model the ash deposition process with the revised particle impaction model and the particle sticking model.

Six different meshes consisting of 0.5, 0.7, 1.1, 1.6, 2.0, and 3.3 million hexahedral cells generated from Ansys ICEM CFD 15.0, which have mesh qualities larger than 0.33 for the Orthogonal Quality and smaller than 0.67 for the Ortho Skew, have been employed to investigate the effect of the mesh on the CFD solutions. The meshes were refined in the vicinity of the probe and the injection region, as well as in the burner region, as shown in Figure 4-6. The residuals for the equations of continuity, momentum, species, and energy were about the magnitude of 10^{-4}, 10^{-5}, 10^{-6} and 10^{-7}, respectively. Both the typical gas flow properties, such as the distributions of the gas temperature and the arrival rate of fly ash particles that impact the probe surface were examined. It was found that there is only little difference in the prediction results with the six different meshes, as shown in Figure 4-7. The independent solutions in the bulk of the EFR can be obtained using a mesh with no less than 0.7 M cells which may be regarded as a reasonably coarse mesh. However, mesh independency was not achieved for the predicted arrival rate of fly ash particles until a mesh with a cell number of over 1.6 M was used, as shown in Figure 4-8. It can be seen from

Figure 4-8, if the 0.7 M cell mesh is employed, then the arrival rate of the impacting particles would be overestimated by approximately 40% compared to the results obtained using 1.6 M cells. This is because a higher impaction efficiency is predicted for all the particles as shown in Figure 4-8. It should be noted that for industrial boilers, the gas flow is highly turbulent (Re $\geqslant$ 100000) and a very thin flow boundary layer will be formed, thus achieving a grid independent solution for particle impaction is usually very difficult in a 3D geometry [84].

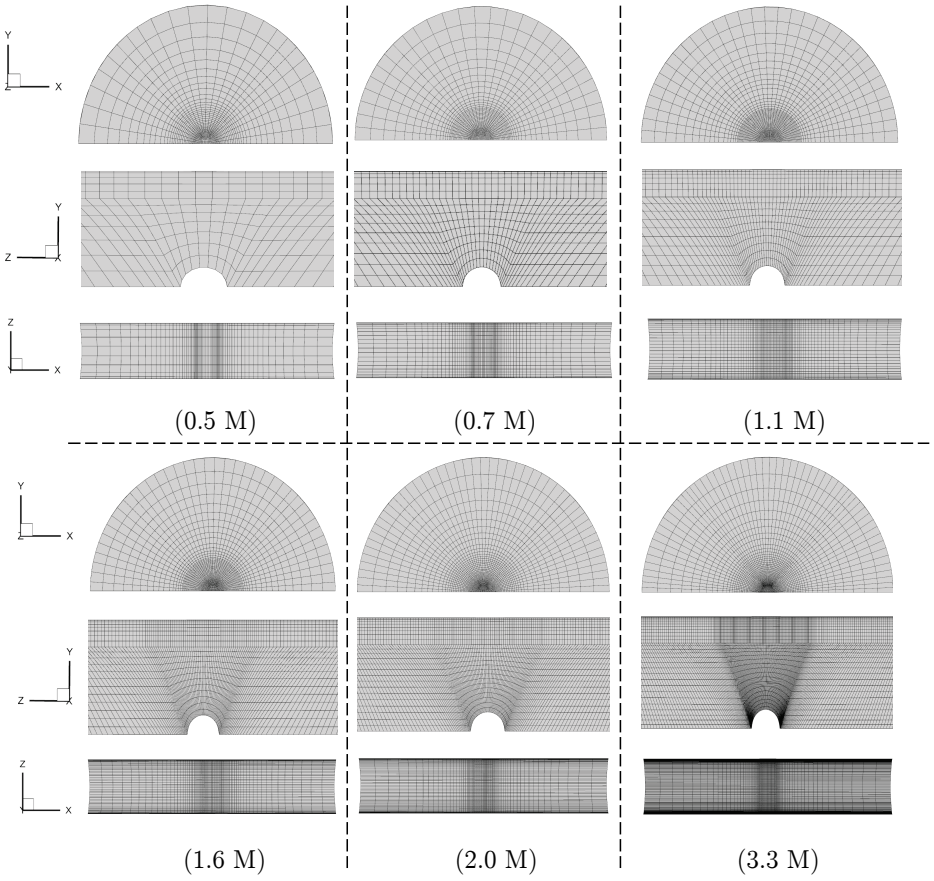

Figure 4-6 Mesh details of the six difference cases investigated.

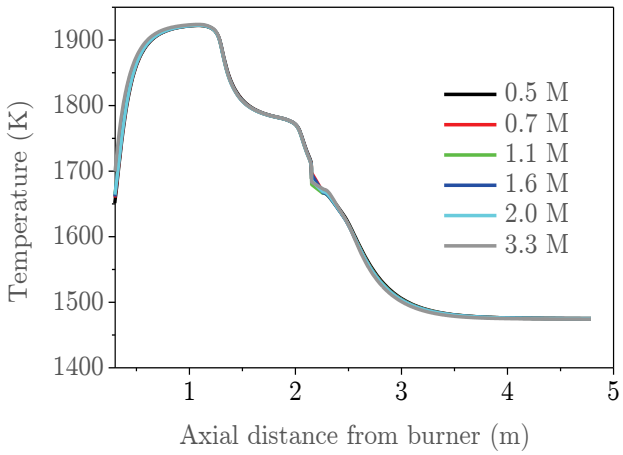

Figure 4-7 Gas temperature along the axis of the furnace using the six different meshes.

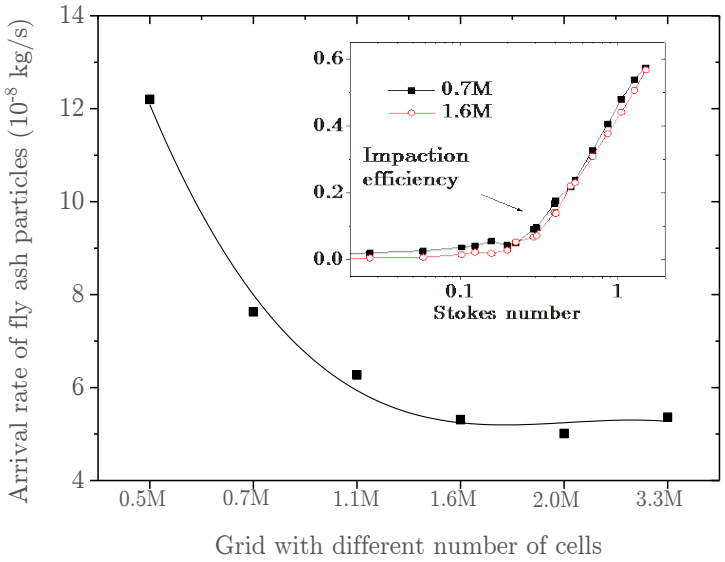

Figure 4-8 The arrival rate of fly ash particles that impact the probe surface as a function of the number of cells and the impaction efficiency of particles as a function of the particle Stokes number for 0.7M and 1.6M.

In the particular case of the Imperial EFR, the particle impaction results obtained from, using the 1.6 M grid was taken as I_{fine} since they are mesh independent solutions for the particle impaction, and the particle impaction results from the 0.7 M grid was taken as I_{coarse} since they are mesh independent solutions of the gas flows. For the case investigated, the interception parameter, R, is in the range

2.9×10^{-5} to 7.5×10^{-3} which give an overall effect on the particle collection efficiency, O_{IP}, in the range of 7-8% and therefore cannot be ignored.

4.3.2 Predicted impaction efficiency and sticking efficiency

The modelling of the particle impaction and sticking is critical for predicting ash deposit formation and growth. Both the improper resolving of the gas flow within the boundary layer near the deposition surface and particle interception can affect the accuracy of the predicted particle impaction in the CFD modelling. Figure 4-9 shows the calculated impaction correction factor F_i and particle impaction efficiency as a function of the Stokes number of the coal and biomass particles employed in the EFR simulation for the four co-firing cases investigated. It can be found that the correction factor increases with an increase in the particle Stokes number. The value approaches unity when the Stokes number is greater than one and this is because the particles are mainly driven by their inertia and the imperfection in the prediction of the boundary flow field which is of secondary importance [84, 120]. However, particles with small Stokes number have a small value of the correction factor and this indicates that the numerical related errors are large when a coarse mesh was used and this is because the particle trajectories are strongly affected by the flow field within the boundary layer which needs to be accurately modelled [84, 119, 120]. The predicted impaction efficiencies for particles with a similar Stokes number are similar for different levels of the PKE addition, and in particular for low co-firing rates. This is because the air and fuel flow rates are almost the same for the four cases and this results in a similar flow distribution, including in the boundary layer flow.

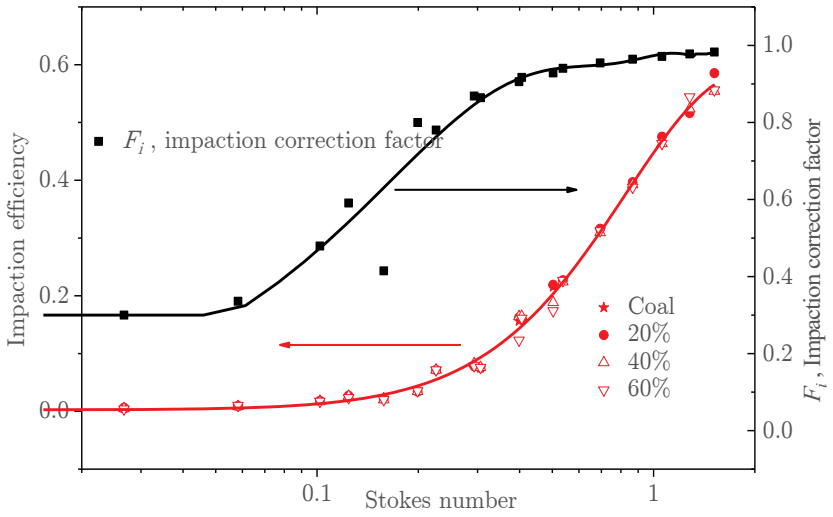

Figure 4-9 The impaction correction factor and impaction efficiency of particles as a function of the particle Stokes number.

Further, the figure shows that the Stokes number of most of the fuel particles is less than 1 and the maximum Stokes number is approximately 1.5, and this indicates the significance of the impaction correction factor in predicting the ash deposition rate. Figure 4-10 compares the results of the predicted overall impaction efficiencies both with and without applying the particle impaction correction. It can be observed that for all the cases, there is 30-50% over prediction in the overall impaction efficiency and this may be resulted if a coarse mesh is employed and no correction is made. Also the figure shows that on increasing the co-firing rates from 0-60%, the overall impaction efficiency increases from about 3.1% to 4.6%. This is due to the fact that the biomass particles have a higher value for the Stokes number than that of the coal particles due to the much larger particle size, and this results in a higher impaction efficiency than that of the SAC particles.

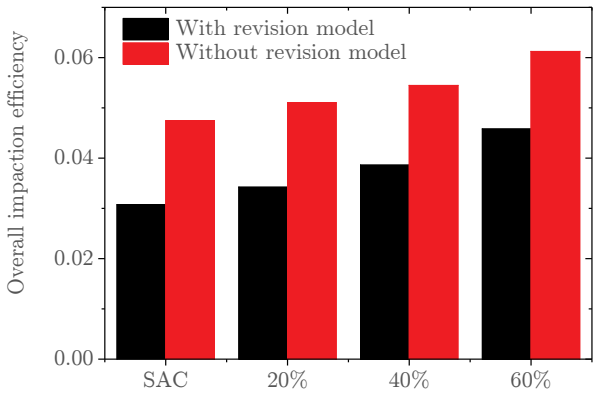

Figure 4-10 The overall impaction efficiency for SAC and for different levels of PKE with and without the revised particle impaction model.

Figure 4-11 shows the predicted overall sticking efficiency (defined as the ratio of the overall mass flow rate of the deposited particles to the overall mass flow rate of the impacting particles) taking into account both the sticking efficiencies of the ash particles and the deposition surface for the four cases investigated. The figure shows that the overall sticking efficiency for the 60% PKE co-firing ratio is approximately 33%, which is the lowest of the four cases investigated. The overall sticking efficiencies are similar for the 20% and 40% ratio cases which lie in the range 53% to 56%. This is because the molten fraction increases on adding 20% and 40% PKE co-firing ratio due to the larger amount of molten phases formed than in the case of 0% PKE co-firing ratio and then the sticking efficiency increases. However, the sticking efficiency decreases on adding 60% PKE. This is due to the formation of high temperature solid phases (such as $Ca_3(PO_4)_2$, $Mg_3P_2O_8$, $AlPO_4$, and $KAlSi_2O_6$) with increasing the alkaline earth metals (calcium and magnesium) by further adding the PKE.

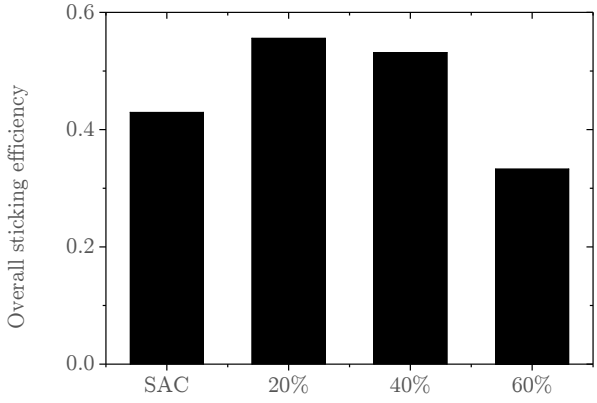

Figure 4-11 The overall sticking efficiency for SAC and for different levels of PKE.

It was noted that the sticking efficiencies for particles were almost the same for all Stokes numbers, with only a slight increase with an increase in the Stokes number. This is because the particles were at the cooling stage at the end of the char combustion, the small particles cool earlier and more quickly and thus have a lower temperature and are less sticky than those of the larger particles [89].

4.3.3 Predicted ash deposition

In the experiments reported in [139, 140], the deposition efficiency, which was determined by the mass percentage of the fuel ash that impacts on the projected surface area of the probe that was retained in the collected deposit, was employed to evaluate the deposition propensity. Figure 4-12 shows a quantitative comparison between the computed deposits (with and without the revised particle impaction model) and the experimental data in terms of the deposition efficiency. In general, the predicted deposition efficiency without the revised particle impaction model is much higher than both the experimental data and the results obtained with the revised particle impaction model. The predicted deposition efficiency with the revised particle impaction model varies between 6.1% to 9.5% for the four case investigated, which is in good agreement with the experimental data. Also the calculation results show that the deposition efficiency at the 60%

PKE co-firing ratio is lower than that at the 40% PKE co-firing ratio and the deposition efficiency is the highest for a co-firing ratio of 40% of PKE. The reason for this modelling outcome is due to the decreasing trend of the overall sticking efficiency at 60% PKE co-firing ratio. However, in the experimental data, the deposition efficiency with a value 8.5% at 60% PKE co-firing ratio is still slightly higher than that at the 40% PKE co-firing ratio which is 8.4%. The repeatability error for the measurement of the deposition efficiency can be up to 4.7% [139]. Therefore, the small disagreement in the deposition efficiency is acceptable between the predicted and experimental results [139, 187]. No obvious increase of deposition efficiency for co-combustion of PKE with South African coal was found when comparing with pure coal combustion both in the experimental results and the simulation results which is controlled by both the particle impaction and sticking. Higher sintering degree of the deposits for co-combustion cases was shown in the experiments. This is because the viscosity of the deposit was decreased with the decrease in SiO_2 and increase in MgO, CaO and P_2O_5 in the ash composition by adding PKE [139].

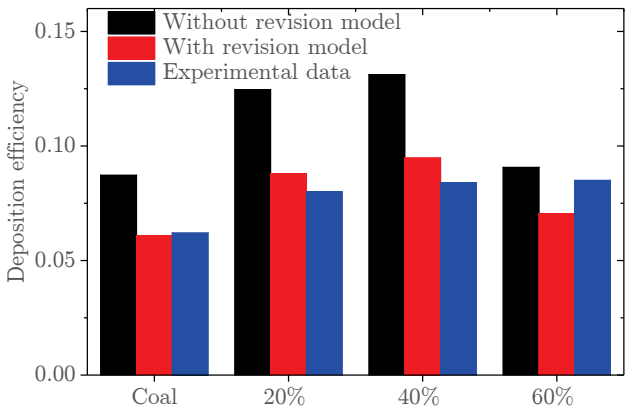

Figure 4-12 A comparison between the computed and the experimental data of the deposition efficiency for the SAC with different levels of PKE.

4.4 Conclusions

An ash deposition model based on modelling the particle impaction and sticking has been developed for the modelling of ash deposition for co-combustion of coal and palm kernel. A revised particle impaction modelling approach is proposed in order to minimize the numerical related errors and avoid using an excessive mesh size. A particle impaction correction factor that takes account of both the effect of particle interception and errors in the particle impaction prediction when a coarse computational mesh is employed. The particle sticking is predicted based on the molten fraction of the particles obtained from the chemical equilibrium calculation using the chemical fractionation data of the fuels in order to consider the short residence time of the fly ash particles.

The deposition efficiencies of co-firing SAC with PKE of four different ratios in the EFR have been calculated using the model and the results obtained have been compared with the experimental data obtained in the EFR. Reasonably good agreement was obtained and it is demonstrated that the proposed model can reduce the numerical related errors in the ash deposition prediction using a reasonable coarse computational mesh for the combustion process simulation. The results suggested that the overall impaction efficiency of the particles increase with an increase in the co-firing ratio of PKE, whilst the overall stickiness efficiency may depend on the relative amount of high- and low- melting point compounds that are formed and this is dictated by the ash composition of the fuels.

Chapter 5: Dynamic CFD prediction of ash deposition in a pilot-scale combustor

Summary

This chapter presents the dynamic ash deposition model and the results of the dynamic CFD predictions of the ash deposit formation for the Zhundong lignite combustion in a pilot-scale furnace. The dynamic CFD model is based on the inertia impaction, the thermophoresis and the direct alkali vapour condensation and incorporates the influence of the heat transfer rate. It is found that, particle deposition from the inertia impaction and the thermophoresis dictates the ash deposit formation under high furnace temperatures. The deposition caused by the direct alkali vapour condensation is less significant. As deposition time increases, particle impaction efficiency decreases and sticking efficiency increases due to the thermophoresis and the local temperature conditions, which result in the time-dependent behaviour of the deposition growth. In addition, the ash deposition characteristics are influenced under different furnace temperatures, due to the change in the particle impaction and sticking behaviours. The heat flux through the deposit can be larger under a higher furnace temperature.

5.1 Introduction

Zhundong (ZD) lignite, with a huge reserve forecast of 390 billion tons, could provide China with the coal consumption for many decades [63, 69, 145]. However,

due to the ZD lignite having a high content of Alkali and Alkaline Earth Metal (AAEM) elements [63, 69, 145], severe problems of ash slagging, fouling and corrosion are induced in the radiation and convection sections of the boilers [145, 188]. This can raise significant practical issues, such as reducing the efficiency and lifetime of boilers. In recent years, many efforts have been paid to experimentally study the ash deposition behaviour of Zhundong lignite combustion in lab-scale [63, 69]/pilot-scale test facilities [146, 148, 189, 190] as well as for full scale boilers [145, 188]. The main reasons for the ash deposition problems of ZD lignite are concluded as: (i) high amount of basic components in the ZD lignite can increase the melting potential in the radiation and convection sections which cause the slagging formation [69, 146, 148, 189], and (ii) both the thermophoretic deposition of small particles and the condensation induced by the sodium related alkali vapours are responsible for the severe fouling phenomenon in the convection section of the boilers [63, 145, 189]. Although the main reasons that caused the severe ash deposition characteristics have been investigated, the deep understanding and the prediction of the particle impaction and sticking behaviours, and the importance of the individual ash deposition mechanism on the ash deposit formation/growth is still insufficient.

This chapter aims to develop a dynamic CFD model to predict the ash deposit growth process for ZD lignite combustion in a pilot-scale furnace. Understanding the initial ash deposition behaviour on cooled tubes is significant to predict the deposition propensity. Therefore, this study focuses on predicting the influence of the main ash deposition mechanisms, namely the inertial impaction, the thermophoretic force and the direct vapour condensation, on the deposit rate and understanding of how the deposit growth will influence the heat transfer rate through the deposit to the cooled deposition probe. In addition to the effect of furnace temperatures on the deposit growth, the particle impaction and sticking behaviours with the deposit growth are studied in-depth and the importance of

the main ash deposition mechanisms on controlling the deposit growth is investigated. The model developed has been tested using the experimental data (including the deposit growth rate and the heat flux) from the Zhejiang University's pilot-scale furnace [148].

5.2 Mathematical models

In order to describe the dynamic deposition growth of the ZD coal, efforts have been made on producing an accurate numerical description of the ash deposition mechanisms in controlling the deposit growth and its interactions with the thermal boundary at the deposit surface. To achieve this, several submodels have been developed and applied in the CFD framework. In this section, the momentum equation to solve the particle trajectories is introduced, followed by a description on the submodels for the thermophoresis and the sticking model of the particles and the deposition surface, as well as the direct alkali vapour condensation and the deposit properties. The solving strategy of the deposition growth model with the CFD framework is discussed at the end of this section.

5.2.1 Particle trajectories

The arrival rate of the ash particles on the deposition surface is dictated by the particle trajectories. The particle trajectories are solved in a combined Eularian-Lagrangian frame of reference where the gas phase is modelled in the Eularian frame of reference and the ash particles are tracked in a Lagrangian frame of reference [70]. The velocity of the particles is governed by the particle momentum equation, which is a balance of the drag, gravity, and other body forces as formulated in the following equation [70]:

$$\frac{d\vec{v}_p}{dt} = \frac{18\mu_g}{\rho_p d_p^2}\frac{C_D Re_p}{24}\left(\vec{v}_g - \vec{v}_p\right) + \frac{\vec{g}(\rho_p - \rho_g)}{\rho_p} + \vec{F} \tag{5-1}$$

where $\overrightarrow{v}$, ρ, μ and d are the velocity, density, viscosity and diameter of the particles, respectively; the subscripts p and g refer to the particle and gas, respectively, C_D is the drag coefficient, and $\overrightarrow{F}$ is the other forces, such as the thermophoretic force, the virtual mass force, the pressure gradient force, the Saffman's lift force, etc.

In this chapter, both the gravitational force and the thermophoretic force are considered. The thermophoretic force, which is caused by the temperature gradient in the gas stream close to a cold deposition surface, needs to be considered when modelling the ash deposition on a cooled surface. In this chapter, the thermophoretic force, $\overrightarrow{F_{th}}$, is considered by the correlations employed by Tablot et al. [70, 84, 191]:

$$\overrightarrow{F_{th}} = -C_{th}\frac{d_p\mu_g^2}{2\rho_g T_g m_p}\nabla T \tag{5-2}$$

$$C_{th} = \frac{12\pi C_s(\tau_g/\tau_p + C_t Kn)}{(1+3C_m Kn)(1+2\,\tau_g/\tau_p + 2C_t Kn)} \tag{5-3}$$

where C_{th} is the thermophoretic coefficient, T_g is the gas temperature, m_p is the particle mass, ∇T is the temperature gradient in the gas phase, $C_s = 1.17$, $C_t = 2.18$, $C_m = 1.14$, τ_g is the fluid thermal conductivity, τ_p is the particle thermal conductivity, and Kn is the Knudsen number. The virtual mass and pressure gradient forces, which are due to the acceleration of the fluid around the particle and the pressure gradient in the fluid, can be ignored when the density of the particle is much greater than the density of the fluid.

The accuracy of predicting the arrival rate of the particles is determined not only by an accurate mathematical description of the physical mechanism, but also by an accurate numerical method. Previous studies have shown that an improper grid around the deposition surface can lead to an inaccurate prediction of the

particle arrival rate due to the inaccurate resolving of the flow-field within the boundary layer near the deposition surface [11, 125]. The accurate resolving of the flow boundary layer requires an extremely fine computational mesh close to the deposition surface. A revised particle impaction model has been developed in Chapter 4. It can be employed to better predict the arrival rate of the particles by resolving the particle impaction efficiency for both the drop tube furnaces and utility boilers without excessive meshing.

The energy balance equation for the particles, which are solved along the trajectories of the particles in order to obtain the corresponding particle temperatures, is given as follows [70, 160, 165]:

$$m_p c_p \frac{dT_p}{dt} = hA_p\left(T_\infty - T_p\right) + \varepsilon_p A_p \sigma\left(\theta_R^4 - T_p^4\right) \tag{5-4}$$

where m_p, c_p, T_p, A_p, and ε_p are the mass, specific heat, temperature, surface area and emissivity of the particles, T_∞ is the gas temperature, σ is the Stefan–Boltzmann constant, and θ_R is the radiation temperature.

5.2.2 Dynamic ash deposition model

The dynamic ash deposition model is composed of several sub-models in order to predict the particle sticking efficiency, deposition rate, and deposition properties. The sticking model is based on the molten fraction of the particles and deposit surface. The chemical equailibrium method is used to predict the molten fraction. The deposition rate is determined by the deposition caused by the inertia impaction, the thermophoretic force and the direct alkali vapour condensation.

The deposit properties (porosity, thermal conductivity, deposition surface temperature, etc.) may change with the deposit growth. Previous research indicates that these changes may have the following characteristics: (i) the deposition surface temperature can increase and the heat flux through the deposit

can decrease; (ii) the physical structure of the deposit can change from a loose and porous structure to a dense and molten structure; (iii) hence, the porosity can reduce at the sintered/slag layer and the thermal conductivity can increase. The porosity is predicted based on the volume fraction of the liquid phase and solid phase in the deposit through the correlation proposed by [65, 91, 94]. Thermal conductivity of the deposit is estimated from previous experimental data presented by [192, 193]. The deposit surface temperature is determined by the total heat flux to the probe surface and the total thermal resistance coefficient caused by the deposit, probe and the cooling oil. The dynamic ash deposition model is accomplished through using the User Defined Functions and the details of the dynamic ash deposition model can be found in Appendix B.

5.2.3 Integration of the ash deposition model with the CFD framework

The commercially available CFD software package ANSYS Fluent version 16.0 has been employed to perform the basic calculations, incorporating the in-house developed User Defined Functions in order to model the ash deposition growth process. Mathematical submodels, such as the SST k-ω model, Discrete Ordinate model and Discrete Phase Model (DPM), were used for modelling the turbulence, radiation heat transfer and particle trajectories. The present CFD model focuses on the deposition probes being placed in the central region of the furnace. A 2D geometry with a tube of diameter 40mm placed in the central region is considered as the computational domain. A fine mesh is generated around the deposition probe in order to resolve the flow-field within the boundary layer and minimize numerical inaccuracies in predicting the particle impaction efficiency. Figure 5-1 shows a schematic diagram of the computational domain and the meshing scheme around the deposition probe. The size of the first cell around the tube is approximately 0.3 mm in order to position about four nodes within the boundary

layer displacement thickness [84]. Hence, an accurate prediction of both the particle impaction efficiency and the particle temperature can be achieved. The mesh consisted of approximately $4.4*10^4$ quadrilateral cells that have qualities larger than 0.90 for the Orthogonal Quality and smaller than 0.10 for the Ortho Skew. The residuals for equations of continuity, momentum, and energy were about the magnitude of 10^{-5}, 10^{-5}, 10^{-4} and 10^{-8}, respectively.

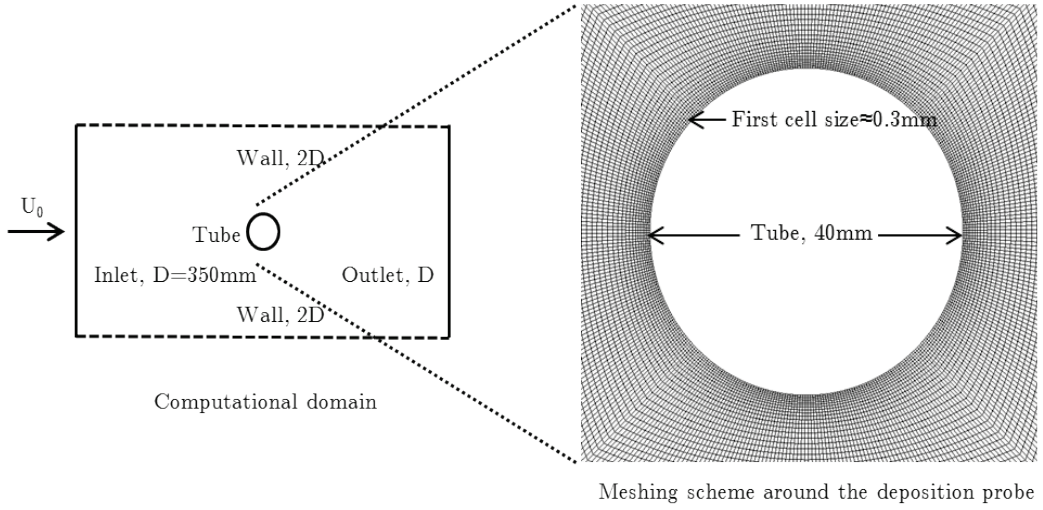

Figure 5-1 Schematic diagram of the computational domain and the meshing scheme around the deposition tube.

In this chapter, three cases with different furnace temperature have been investigated, namely, 1373 K, 1543 K and 1593 K. It is assumed that the discrete parcels of particles are uniformly distributed and the particles are injected through the inlet boundary condition [85, 132, 133]. The flow rate of the ash particles of 1.153 g/s and the velocity of the flue gas (N_2-0.758, CO_2-0.166, O_2-0.05, H_2O-0.026, mole fraction) and particles of 2.8 m/s have been used from the experiments [148]. The ash particle size ranges between 1 μm and 60 μm with a mean diameter of 16 μm and a spread parameter of 0.7 based on the Rosin-Rammler distribution, which indirectly results from the original coal particle size distribution and the ash content [148, 169]. It should be noted that aerosols

generated from nucleation of the alkali vapour is neglected due to the high furnace temperature [63].

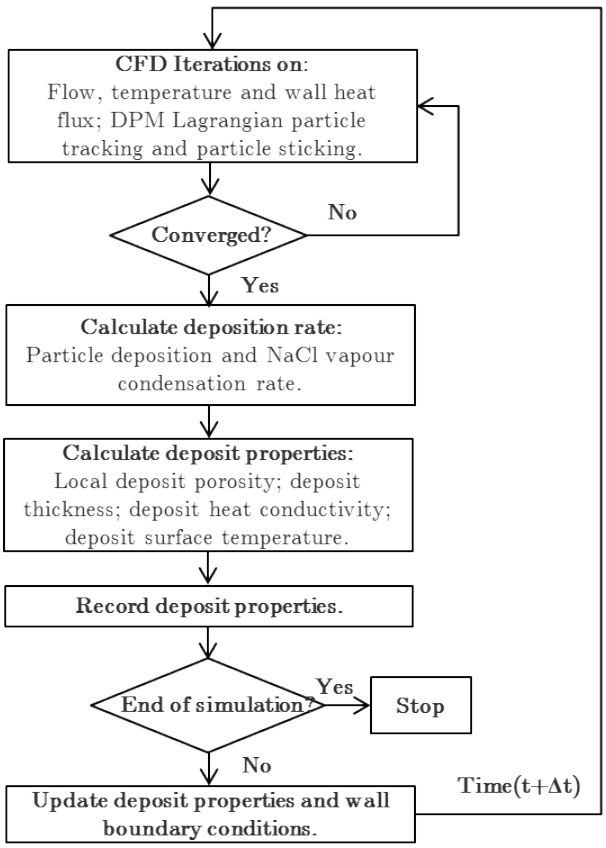

Figure 5-2 The algorithm of the ash deposition growth model integrated into the CFD framework (modified from [91, 130, 131]).

Figure 5-2 shows a brief flow chart of the algorithm used to carry out the simulation of the ash deposition growth process. A similar quasi-transient calculation concept has also been used to integrate the deposition model with the CFD framework [91, 130, 131]. In a time step, CFD iterations are carried out to solve the gas flow, temperature and wall heat flux. Then the Lagrangian particle tracking and particle sticking procedures are performed to determine the particle deposition. The total deposition rate can be determined by the particle deposition and the direct alkali vapour condensation rate. Then the new deposit properties (porosity, thickness, thermal conductivity, total heat resistance, etc.) are

calculated, updated and stored in the User Defined Memories. In addition, a new deposition surface temperature is calculated based on the total heat flux and the total heat resistance from the updated deposit properties; the new deposition surface temperature is given to the wall boundary surface conditions by the User Defined Functions for the CFD calculation in the next time step and this process is continued until the end of the simulation. It should be noted that the simulation process starts with a clean deposition tube (deposition time=0) placed in the furnace and the initial surface temperature is predicted based on the total thermal resistance contributed from the probe itself and the cooling oil [95], as shown in Equations (5-12) and (5-13). In addition, the calculation ends within two hours of the deposition time, where the shedding is less important [148]. The time step size is dynamically determined by limiting the increase in the deposition surface temperature in a time step to be less than 1K in order to achieve a balance between the accuracy of the simulations and the expense of the computation time. Therefore, a time step size of 1 s was employed at the initial stage because the surface temperature increased at a high rate at this stage. The time step size gradually increased to 30s at the later stages because the increase in the deposition surface temperature became very small.

5.3 Results and discussion

5.3.1 Ash deposit formation under different furnace temperatures

The furnace temperature, which can influence the local temperature condition (the impacting particle temperature and the thermal boundary near the deposition surface), is a significant factor that controls the ash deposit formation. Therefore, it is important to investigate the ash deposition behaviour under different furnace temperatures by using the present deposition model. Figure 5-3 shows a comparison of the heat flux between the predicted results and the

experimental data among the three different furnace temperatures as a function of the deposition time. It can be seen that the three curves show similar variance trends. Generally, it can be seen that the predictions are in reasonable agreement with the experimental data for the three cases. Also, it is noticed that higher furnace temperatures result in a higher heat flux.

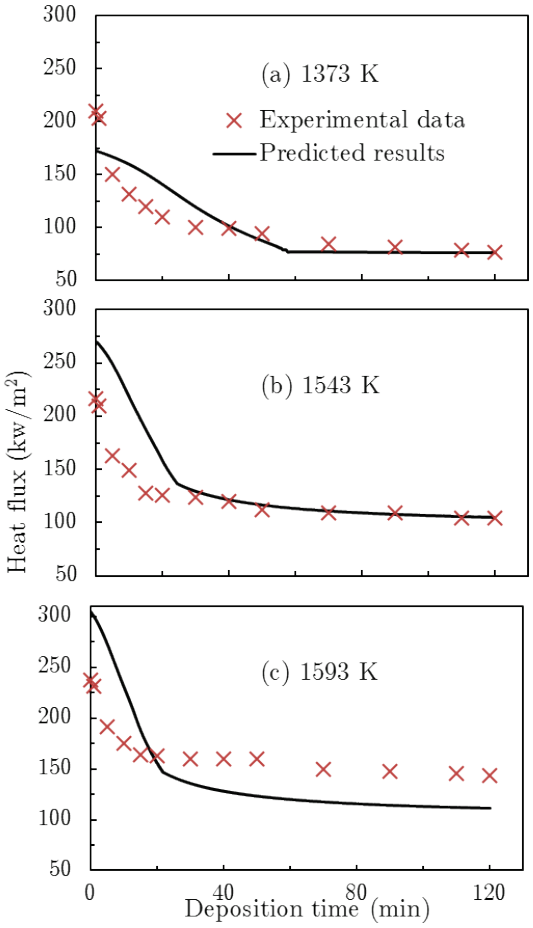

Figure 5-3 Comparison of the heat flux between the predicted results and the experimental data as a function of the deposition time for the three cases.

Figure 5-4 shows a comparison of the overall particle impaction efficiency for the three different furnace temperatures as a function of the deposition time. It is noticed that the 1543 K case has a similar overall impaction efficiency compared to that of the 1593 K case. At the initial stage of deposit formation, the 1373 K case has a much higher overall impaction efficiency than both the 1543 K and 1593 K cases at the same deposition time. This is because the deposition surface

temperature under a lower furnace temperature is much lower than that under a higher furnace temperature at the same deposition time, which can result in a larger thermal gradient near the deposit surface and a higher thermophoresis increase in the particle impaction efficiency. Figure 5-5 shows a comparison of the overall particle sticking efficiency for the three different furnace temperatures as a function of the deposition time. It can be observed that the sticking efficiency increases with an increase in the furnace temperature based on the present sticking model. The efficiency reaches the highest value in the later deposition stage, 0.25, 0.58 and 0.63 for 1373 K, 1543 K and 1593 K cases, respectively. Figure 5-6 shows a comparison of the accumulated deposition mass (normalized by the total accumulated deposition mass after two hours' deposition time for the 1593 K case) for the three different furnace temperatures as a function of deposition time. It is found that there is much more deposit mass accumulated under a higher furnace temperature. This is mainly because there is a much higher particle sticking efficiency under a higher furnace temperature as shown in Figure 5-5. Figure 5-7 shows a comparison of the average deposit thickness of the three different furnace temperatures as a function of the deposition time. It is also found that the higher deposit thickness is accumulated under a higher furnace temperature. It should be noted that the detailed experimental deposit thickness results have been presented for the 1543 K case. Therefore, the comparison of deposit thickness between the predicted results and experimental data will been given in the Section 5.3.2.3.

Therefore, the predicted results suggest that the heat flux through the deposit increases with increasing furnace temperature and this is confirmed by the experimental data. In addition, both the deposit mass and the deposit thickness are larger under a higher furnace temperature than those under a lower furnace temperature. This is because the particle sticking efficiency increases with an increase in the furnace temperature. Wu et al. [189] also observed a higher

deposition rate under a higher furnace temperature in the radiation section for the Zhundong coal combustion in a pilot-scale combustion test. However, Zhou et al. [148] found that the stable deposit thickness (when the shedding rate is balanced with the deposition rate) under a lower furnace temperature is higher than that under a higher furnace temperature. This may be attributed to the combined effect of the deposition rate, shedding rate, and the deposit microstructure.

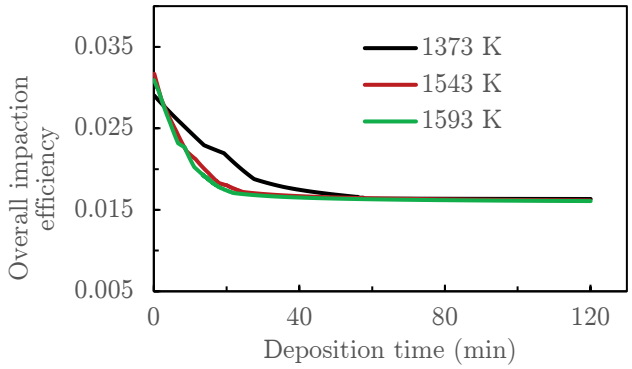

Figure 5-4 Overall particle impaction efficiency as a function of the deposition time under different furnace temperatures.

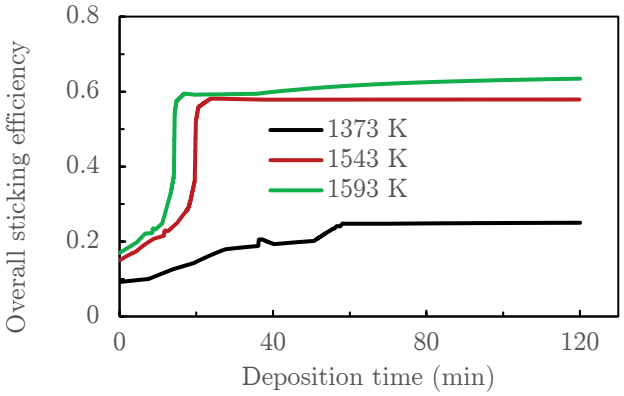

Figure 5-5 Overall particle sticking efficiency as a function of the deposition time under different furnace temperatures.

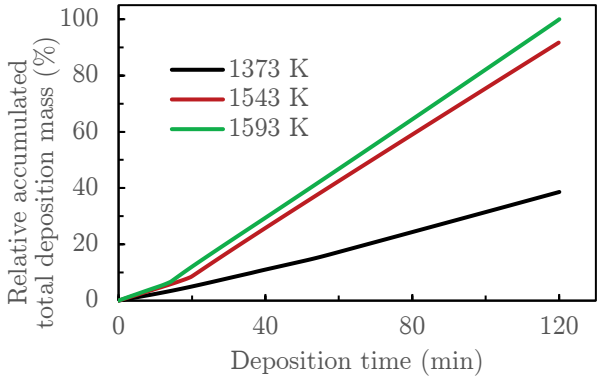

Figure 5-6 Relative accumulated total deposition mass as a function of the deposition time under different furnace temperatures.

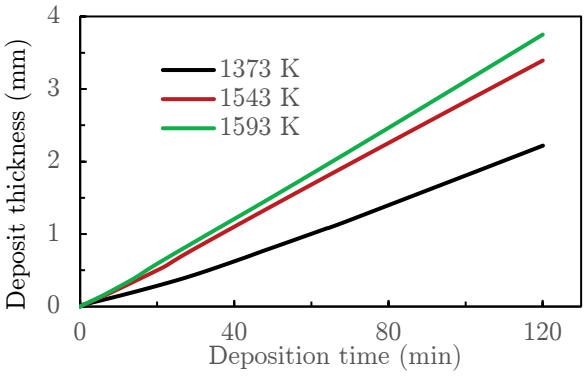

Figure 5-7 Average deposit thickness as a function of the deposition time under different furnace temperatures.

5.3.2 Predicted results of the baseline case (furnace temperature under 1543 K)

5.3.2.1 Particle impaction efficiency and sticking efficiency

The prediction of the particle impaction and sticking is critical for modelling the ash deposit formation because particle impaction and sticking determine the amount of the arrival particles which may stick on the deposition probe surface. Figure 5-8 shows the predicted overall particle impaction efficiency (defined as the overall mass flow rate of the particles impacting on the probe to the overall mass flow rate of particles in the projected surface area of the probe) and the deposition surface temperature as a function of the deposition time. It can be

found that, under the conditions without thermophoretic force and with only the inertia impaction, the overall particle impaction efficiency ($\eta_{i\_inertia}$), which has a value ranged from 0.021 to 0.015, decreases with an increase in the first 30 minutes and then it remains essentially unchanged. This is because the local condition near the deposition surface (velocity, gas viscosity, etc.) changes with the deposition growth. Under the condition with both the inertia impaction and thermophoretic force, the overall particle impaction efficiency ($\eta_{i\_inertia+tp}$) shows a similar variance trend compared to $\eta_{i\_inertia}$. In addition, $\eta_{i\_inertia+tp}$ is larger than $\eta_{i\_inertia}$, ranging from 0.032 to 0.016. Also, Figure 5-9 shows that the difference of overall particle impaction efficiency between $\eta_{i\_inertia+tp}$ and $\eta_{i\_inertia}$ gradually reduces with the increase in the deposition surface temperature. This is because the influence of the thermophoretic force on the particles, which is dictated by the thermal gradient near the deposit surface, is decreased as a result of the increase in the deposition surface temperature.

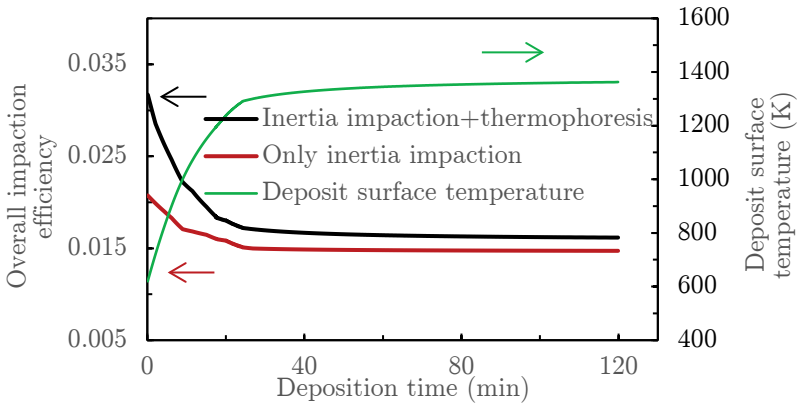

Figure 5-8 The overall particle impaction efficiency and deposit surface temperature as a function of the deposition time.

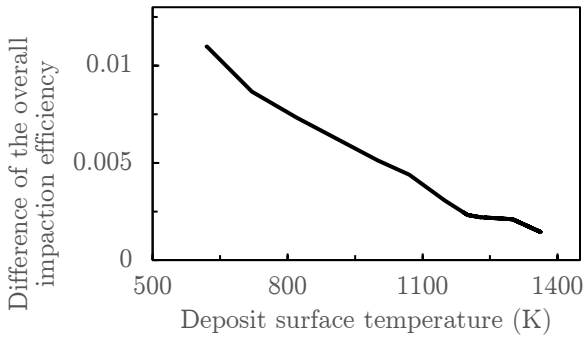

Figure 5-9 The difference of overall particle impaction efficiency between $\eta_{i\_inertia+tp}$ and $\eta_{i\_inertia}$ as a function of the deposition surface temperature.

Therefore, the thermophorestic force contributes to the overall particle impaction efficiency by as much as 50% in the initial stage and nearly 10% at the later stage. Beckmann et al. [125] also found that the thermophoresis could increase the arrival rate of the particles by as much as 7-50% onto the cooled deposition tube. The amount of the increased overall particle impaction efficiency (or the arrival rate) by the thermophosis is determined by the particle size distribution and the thermal gradient in the vicinity of the deposition surface.

In order to further study the influence of the thermophoresis on the individual particle impaction behaviour, the impaction efficiency of the particles as a function of the particle Stokes number is shown in Figure 5-10. It can be seen that, under the condition without thermophoretic force and with only the inertia impaction, the particle impaction efficiency ($\eta_{pi\_inertia}$) is very small and close to zero (smaller than 0.01) when the particle Stokes number is less than 0.1 and then the particle impaction efficiency sharply increases with an increase in Stokes number. This is because the particles with a larger Stokes number are less likely to be affected by the gas flow and more likely to impact on the deposition surface. However, particles with smaller Stokes number follow more closely to the fluid streamlines and they are less likely to impact on the surface [175]. Similar variations of the particle impaction efficiency by the inertia impaction is also

predicted in the references [84, 120, 158] using the RANS, LES and DNS based CFD methods. However, under the condition with both the inertia impaction and thermophoretic force, the particle impaction efficiency ($\eta_{pi\_inertia+tp}$) is larger than $\eta_{pi\_inertia}$, as shown in Figure 5-10. In addition, the influence of the thermophoresis on the increase in the efficiency is enhanced with a decrease in the deposition surface temperature, as shown in Figure 5-10. This results in a higher increase of overall impaction efficiency with a lower deposition surface temperature as shown in Figure 5-8 and Figure 5-9.

Figure 5-11 shows the predicted overall particle sticking efficiency (defined as the ratio of the overall mass flow rate of the deposited particles to the overall mass flow rate of the impacting particles) and the deposit surface temperature as a function of the deposition time. It can be observed that the overall particle sticking efficiency gradually increases with an increase in the deposition time and then it remains essentially unchanged, ranging from 0.15 to 0.58, and a corresponding increase in the deposition surface temperature, then a nearly flat variance of the temperature. It is noticed that there is a transition of a sharp increase in the sticking efficiency and this occurs at nearly 25 mins deposition time, which corresponds to a deposition surface temperature of approximately 1230 K, as shown by the red rectangle and the red arrow in Figure 5-11. This is because the deposit surface starts to melt at this temperature and becomes sticky according to the chemical equilibrium calculations. It is also noted that the sticking efficiencies for the particles increase with an increase in the Stokes number. This is because the ash particles were at the cooling stage when moving towards the cold deposition surface, the small particles cool earlier and more quickly and thus have a lower temperature [89].

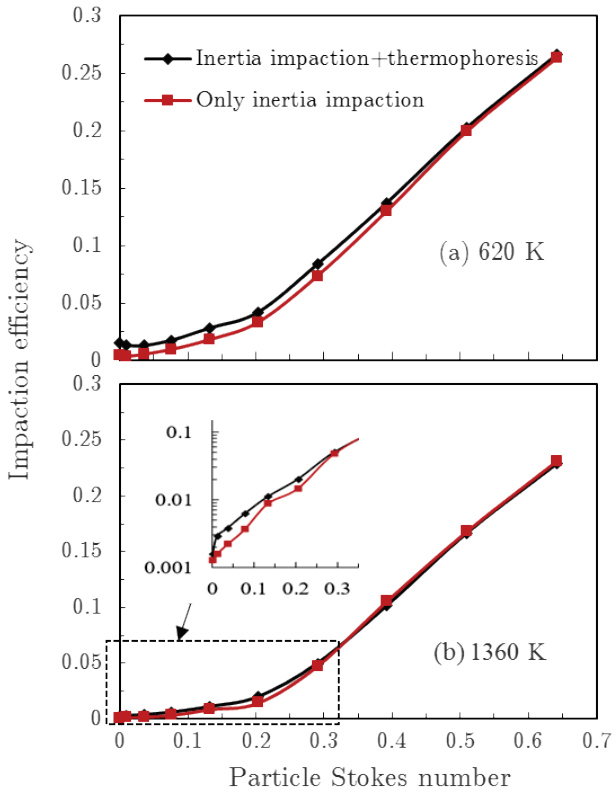

Figure 5-10 The particle impaction efficiency as a function of the particle Stokes number under a low deposit surface temperature (620 K) and a high deposit surface temperature (1355 K).

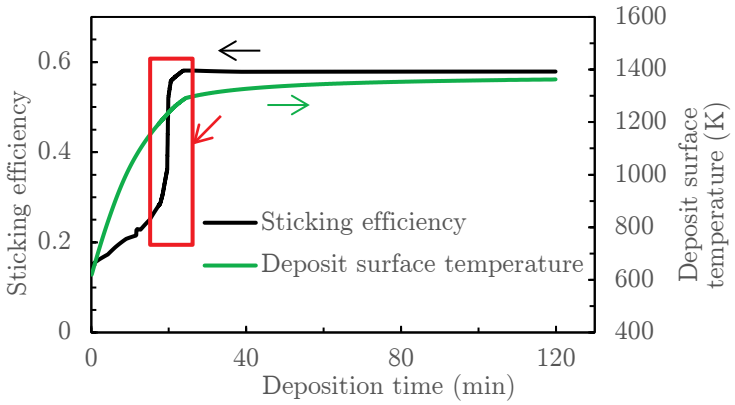

Figure 5-11 The overall particle sticking efficiency and deposit surface temperature as a function of the deposition time.

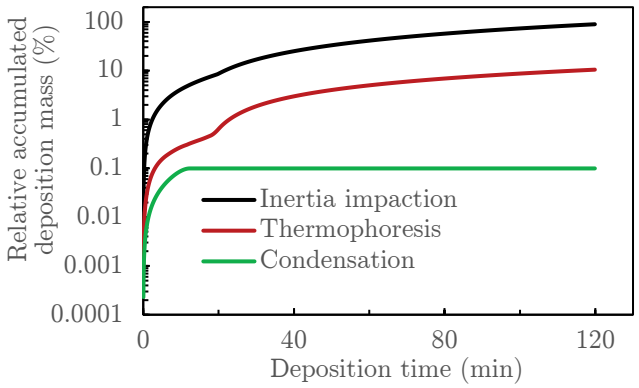

Figure 5-12 The relative accumulated ash deposition mass by different deposition mechanisms as a function of the deposition time.

5.3.2.2 Deposition properties

In order to understand the contribution of the deposition mechanisms (the inertia impaction and the thermophoresis, and the direct vaopur condensation) on the deposit formation, the relative accumulated deposition mass (defined as the ratio of the accumulated deposition mass to the total deposition mass after two hours' deposition time) by the three deposition mechanisms as a function of the deposition time as shown in Figure 5-12. It is found that the relative accumulated deposition mass caused by both the inertia impaction and the thermophoresis gradually increases with an increase in the deposition time. The deposition caused by the direct alkali vapour condensation is only accumulated in the initial stage for approximately thirteen mins by the deposition model. This is because the saturation vapour pressure of the alkali phase (NaCl) increases with a rise in the deposition surface temperature. When the saturation vapour pressure is high enough, the partial pressure of the alkali vapour (NaCl) cannot support the direct vapour condensation according to the direct alkali vapour condensation model [127, 194]. In addition, it can be seen that the relative accumulated deposition mass caused by the inertia impaction is almost four times as large as that by thermophoresis. The relative accumulated deposition mass caused by the direct condensation is the smallest, which is hundred times smaller than that caused by

the inertia impaction. In addition, it can be seen that the relative accumulated deposition mass caused by the inertia impaction is almost eight times as large as that by thermophoresis. The relative accumulated deposition mass caused by the direct condensation is the smallest, which is hundred times smaller than that caused by the inertia impaction. In addition, the contribution of the direct condensation (defined as the ratio of the accumulated deposition mass by the direct condensation to the total accumulated deposition mass) only accounts for approximately 2% in the initial stage and 0.1% in the final stage.

Therefore, the predicted results suggest that the main deposition mechanisms are the inertia impaction and the thermophoresis and the contribution by the direct vapour condensation is less significant. In addition, the experimental observations of the ash composition in the different layers of the deposit show that the sodium content among all the deposit layers is less than that in the original ash and the sodium content in the inner layer is larger than that in the outer layers for the studied furnace temperature [148], which is consistent with the predicted results related to the contribution of the alkali vapour condensation. Wu et al. [189] found that the particle depositions, rather than the vapour condensation, are the main ash deposition mechanisms in the radiation section for Zhundong coal combustion in a pilot-scale combustion test. Leppanen et al. [127] also found that the contribution of the direct alkali vapor condensation, which only contributes up to 0.01% of the total deposited mass, is insignificant by using a similar direct vapour condensation model to that employed in this study.

However, it should be noticed that the vapour condensation is significant for ash deposit formation in the convection section which has a much lower furnace temperature than that in the radiation section. Under a lower furnace temperature, alkali vapour may behave under the following modes [61, 122, 127]: (i) nucleation to generate fume particles; (ii) condensation onto already existing

particles; and (iii) direct condensation onto the deposition surfaces. Fume particles can enhance the initial ash deposit formation on the cooled superheater surfaces by the thermophoretic force [63, 127]; the particle surfaces coated with condensed alkali phases could have a higher sticking possibility [122]. Li et al. [63] investigated the ash deposit formation of Zhundong coal combustion in a down-fired furnace and they found that the fume particles generated by indirect alkali vapour condensation could initiate the ash deposit formation under a furnace temperature of almost 1073 K and the bulk fly ash particles with a sticky surface possibly coated by the condensed alkali vapour phases further enhance the ash deposit formation.

5.3.2.3 Heat transfer properties and deposition growth

In order to understand the heat transfer abatement with the ash deposit formation and growth, the heat flux (including both the predicted results and the experimental results) through the deposit as a function of the deposition time is shown in Figure 5-13. Generally, it can be observed that the predictions are in reasonable agreement with the experimental data. The heat flux significantly decreases in the first half an hour and then slowly decreases in the later stages, which is consistent with the fact that the initial stage of the ash deposition is significant in the heat transfer abatement [65]. This is because the heat conductivity of the deposit is quite low in the initial stage due to its high porosity and low sintering degree [148, 192, 193], even though the accumulated deposit at this stage is not huge compared to that in the later stage, as shown in Figure 5-12. The average deposit thickness (including both the predicted results and the experimental results) as a function of the deposition time is shown in Figure 5-14. It can be seen that the predicted deposit thickness shows a lower growth rate compared to the experimental data. This may be a result of the underestimation of the deposition rate, which can lead to a lower prediction of deposit growth

rate. Up to date, it is still a challenge to quantitatively predict the particle sticking efficiency, which needs a robust sticking model to take into consideration the particle melting behaviour (ash chemistry), particle kinetic energy (particle diameter and velocity) and material properties of the particle and deposit surface, which will be considered as future work.

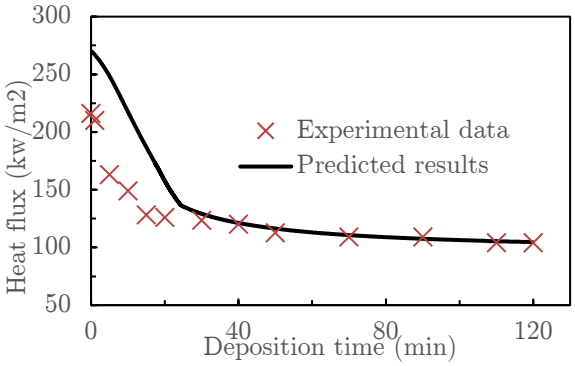

Figure 5-13 Comparison of the heat flux through the deposit between the predicted results and the experimental data as a function of the deposition time.

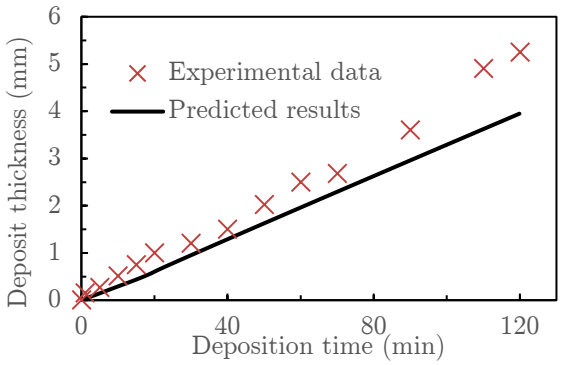

Figure 5-14 Comparison of the average deposit thickness between the predicted results and the experimental data as a function of the deposition time.

5.4 Conclusions

A dynamic ash deposition model based on inertia impaction, thermophoresis and direct alkali vapour condensation has been developed for the modelling of the ash deposit formation on a cooled deposition probe under high furnace temperatures in a pilot-scale furnace. The ash deposition model incorporates the energy

conversation principles to include the effect of the heat transfer on the deposition growth. The particle impaction and sticking behaviours, which are dependent on the deposit growth, are investigated. Also, the ash deposition behaviour under different furnace temperatures is studied through the developed deposition model.

The predicted results for the ash deposition behaviour and the heat flux through the deposition probe have been compared with the experimental data obtained in the pilot-scale furnace. Qualitative agreement is obtained for the heat flux and deposit thickness between the predicted results and experimental data. The results suggest that ash deposit formation is mainly dictated by the particle deposition from the inertia impaction and the thermophoresis under high furnace temperatures. The deposition caused by the direct alkali vapour condensation is less significant. The overall particle impaction efficiency decreases at the initial stage with the deposit growth and stabilised at higher deposition surface temperature. This is mainly due to the decrease in the effect of thermophoresis. The overall particle sticking efficiency increases with the deposit growth due to the increase in the local temperature conditions (particle temperature and the deposition surface temperature). The heat flux through the deposition probe significantly decreases at first and then slowly decreases as the deposit builds up. Also, it is noticed that both the particle impaction and stickiness control the ash deposit formation. Much higher sticking efficiency can result in a larger deposition rate under a higher furnace temperature, while the calculated overall particle impaction efficiency decreases at the initial stage. This is because the deposition surface temperature increases to a much higher level under higher furnace temperature and this results in a lower thermophoresis influence of the particle impaction.

Chapter 6: Development of an ash deposition indice for boilers

Summary

This chapter develops a method to build an indice to predict the overall slagging propensities for coals/blends combustion in utility boilers. The method is based on the initial slagging routes and the sintered/slagging route. Two types of initial slagging routes are considered, namely (i) pyrite-induced initial slagging on the furnace wall, and (ii) fouling caused by the alkaline/alkali components condensation in the convection section. The sintered/slagging route is considered by the liquids temperature (LT), which represents the melting potential of the main ash composition. The partial least square regression (PLSR) technique, coupled with a cross validation method, is employed to obtain the correlation for the ash deposition indice. The results obtained show that the developed indice yields a higher success rate in classifying the overall slagging/fouling potential in boilers than some of the typical slagging indices. The influence of the acid components (SiO_2 and Al_2O_3) on the ash deposition prediction is investigated for guiding the mineral additives.

6.1 Introduction

Considerable progress has been made in the last decades in understanding the ash deposition mechanisms of various coals. For example, Eastern US coals, such as Illinois and Appalachian coals, have higher concentrations of Fe

components than Western US coals [136], and the initial slagging caused by the pyrite is one of the main issues related to slagging problems [14, 136, 195]. For low rank Western US coals, such as Wyoming and Montana coals, which have higher concentrations of alkaline/alkali components than Eastern US coals, fouling in the convection section is a serious problem [46, 196, 197]. Figure 6-1 shows the main ash deposition mechanisms for US coals in utility boilers [21, 27, 136]. Generally, it is regarded that ash deposition can be mainly dictated by three different routes: (i) Pyrite-induced initial slagging route generates from the pyrite particles due to its large density and low melting temperature under a reducing atmosphere on the furnace wall [13, 21, 197]; (ii) Fouling-induced initial slagging route generates from the condensation of alkali vapours and thermophertic deposition of aerosol/fume particles on the superheaters or economizers; (iii) The sintered/slagging route is triggered by the molten matrix generated from the major basic components reacting with clay and quartz, etc., and the reducing atmosphere can promote this process when a high Fe concentration is present in the coal [27, 136]. Furthermore, severe slagging in the furnace chamber could increase the furnace exit gas temperature (FEGT) and hence this may further aggravate the ash deposition in the convection section. Therefore, the severe ash deposition in boilers could be triggered by the three different routes and a successful ash deposition indice should be capable of predicting the deposit formation from these three formation routes.

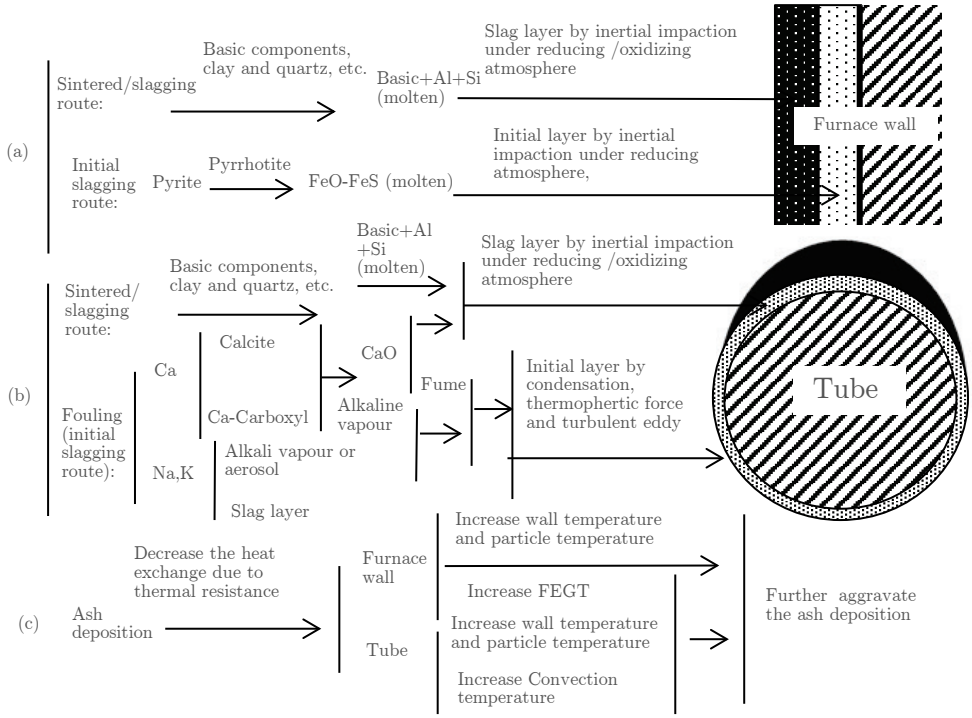

Figure 6-1 Schematic of the ash deposition routes in boilers (modified from [21, 27, 136]).

This chapter takes a new approach to build an ash deposition indice for fuel slagging propensity analysis. The ash deposition indice takes into consideration the multi-ash deposition routes which exist in industrial boilers and the indice is developed with support from the actual observations made in a range of industrial boilers. The sintered/slagging route is predicted by using the overall melting potential of the major ash components through the chemical equilibrium calculations; the initial slagging route caused by either the pyrite or the alkaline/alkali components is predicted by using the amount of the related basic ash components; the known slagging observations for coal combustion in boilers are used as the training data to acquire the correlation of the slagging indice. The partial least square regression (PLSR) method, coupled with cross-validation, is employed to develop the slagging indice. The study reported in this chapter is mainly based on the available data for typical US coals, and the results are

compared with the field observations for 30 sets of coals/blends combustion in boilers as presented in Appendix A.

6.2 Mathematical models

6.2.1 Model assumptions

(i) Both the Fe_2O_3 content and total sulphur content are employed to represent the pyrite content in the US coals, which can be used to represent the severity of the initial slagging route [13, 22]. Therefore, it is assumed that the pyrite-induced initial slagging route can be accounted for by the amount of the Fe_2O_3 content and the total sulphur content.

(ii) The alkaline/alkali content is used to represent the initial slagging route (or fouling route) caused by the condensation of the vapour species because the alkaline/alkali content is directly related to the accumulation of the fouling potential [134] and the alkali content is proportional to the content of the alkali phases in the flue gases [19, 20].

(iii) The SiO_2+Al_2O_3 content is considered in the model. This is because the acid components could have dual effects on the slag formation: (a) The high amount of acid components could increase the melting point and the viscosity of the ash [26], which can decrease the sintered/slagging propensity; (b) The acid components could possibly capture the alkali/alkaline components to decrease the alkali evaporation into flue gas [19, 20] as well as pyrite to decrease the formation of high molten Fe^{2+}-slag and Fe^{3+}-slag [198, 199], that can in turn decrease the initial slagging routes.

(iv) The melting capabilities of the major ash composition under oxidizing/reducing atmosphere are employed to represent the sintered/slagging route [86]. This assumption is employed for all types of coals. In order to evaluate

the melting capability, liquidus temperature (LT) is employed and predicted by using the chemical equilibrium calculations.

(v) For those coals with Fe_2O_3 as the major basic oxide, the deposition is formed mainly in the radiant section with the slag rich in the iron content [21]. However, for the coals with alkaline/alkali constituents as the major fluxing mineral, serious ash deposition (fouling) is observed in the convection section [200]. Hence coal ash can be classified into two types, the lignitic and bituminous types of ash [102]. For lignitic type ash defined as the amount of either alkaline or alkali components being greater than the amount of Fe_2O_3, only the initial slagging route caused by the alkaline/alkali condensation is considered as the major initial slagging route. For bituminous type ash defined as the amount of Fe_2O_3 being greater than the amount of alkaline and alkali components, only the initial slagging route caused by the pyrite is considered as the major initial slagging route.

Therefore, based on the above assumptions, the proposed method to build the ash deposition indice is developed as follows: for bituminous type coal, the liquidus temperatures under the oxidizing atmosphere and the reducing atmosphere (LT_o and LT_r), the SiO_2+Al_2O_3 content, the Fe_2O_3 content and the total sulphur content can be employed as the independent variables; for lignitic type coal, the liquidus temperatures under oxidizing atmosphere and reducing atmosphere, the SiO_2+Al_2O_3 content, and the alkaline/alkali content can be employed as the independent variables. The overall slagging/fouling observations can be employed as the dependent variable. The partial least square regression (PLSR) technique, coupled with a cross validation method, is employed to obtain the correlation for the indice. This is because (a) in this work, the data of slagging observations is limited and the independent variables in the method to build the ash deposition indice are highly correlated, and (b) the PLSR method is specifically designed to deal with multiple regression problems where the number

of observations is limited and the correlations between the independent variables are high [201].

6.2.2 Prediction of the liquidus temperature

The liquidus temperature is the temperature at which the first solid phase just starts to precipitate on the cooling of a slag-liquid oxide melt [138]. The temperature is predicted based on the major ash composition (Al_2O_3, SiO_2, Fe_2O_3, CaO, and MgO) by using the chemical thermodynamics software FactSage 6.4 [138]. The software is based on the minimization of the Gibbs free energy from the system subject to the mass balance constraints [177, 178].

The calculations were performed by using the equilibrium module together with the databases ELEM, FToxid, FTsalt and FACTPS. The slag model chosen in the calculations was the 'SLAGA' with possible 2-phase immiscibility [138]. Five major ash components (Al_2O_3, SiO_2, Fe_2O_3, CaO, and MgO) were included in the calculations; for lignite, Na_2O is also included due to its high amount; K_2O is excluded due to its low amount in the ash; however, the other components (SO_3 and P_2O_5) were also neglected due to the fact that S and P are volatile under high temperatures observed near the liquidus temperature [138]. It was assumed that all Fe was in the Fe^{3+} state under the oxidizing atmosphere because a large portion of iron is in the Fe^{3+} state for oxidizing conditions [202] and both the Fe^{2+} and Fe^{3+} states were considered under the reducing atmosphere.

6.2.3 PLSR and Cross-Validation

The Partial Least-Squares Regression (PLSR) technique is a mathematical technique that generalizes and combines features from multiple regression and a principal component analysis [203, 204]. Therefore, PLSR is able to analyse data of larger and highly correlated multivariate systems and it has a higher prediction ability than those obtained with multiple regression [203, 205], which is suitable for the present work because of the high correlation coefficients among the independent variables (liquidus temperature, Fe_2O_3, and alkaline/alkali components). The one-at-a-time form of cross-validation method, which is a criterion to calculate the predicted error in the sum of the squares when leaving out a single observation, is often employed to determine the stopping criterion and the number of latent variables in the PLSR method [201, 203-205]. In this work, the algorithm of the PLSR, coupled with the cross-validation, is analysed and developed based on the Matlab platform as shown in Figure 6-2. For more details about the PLSR and cross-validation method, see [201, 203-208].

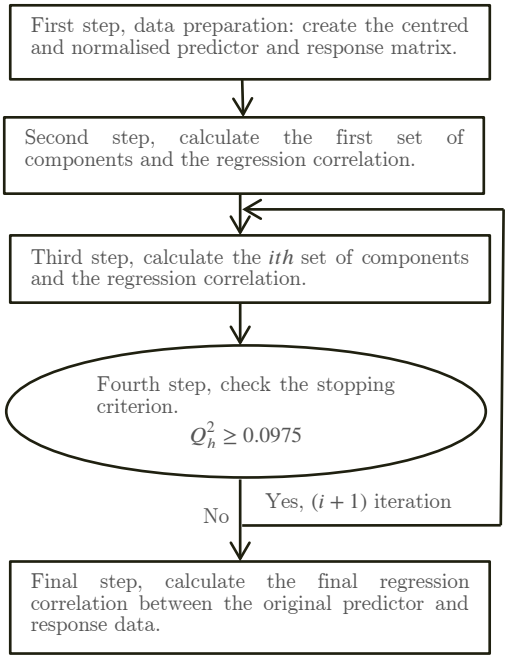

Figure 6-2 The algorithm for the PLSR coupled with cross-validation.

The first step is to create the predictor and response matrices, X ($\in R^{n\times p}$) and Y ($\in R^{n\times 1}$). Then these two matrices are centered and normalized, $E_0 = (\varepsilon_{ij})_{n\times p}$ and $F_0 = (f_i)_{n\times 1}$, respectively, which corresponds to giving the variables X and Y the same prior importance and weights in the analysis [201].

The second step is to calculate the first set of components (weight vectors, score vectors and loading vectors), which is defined as follows [201, 203]:

$$Objective\ function: \theta_1 = \left\| E_0^T F_0 \right\| \rightarrow max \tag{6-1}$$

$$w_1 = \frac{E_0^T F_0}{\left\| E_0^T F_0 \right\|} \tag{6-2}$$

$$t_1 = E_0 w_1 \tag{6-3}$$

where $\theta_1$is the objective function, w_1 is the first weight vector of E_0, and t_1 is the first score vector of E_0. The initial regression equation, which is used to predict E_0 and F_0 from t_1, can be determined as follows [201, 203]:

$$E_0 = t_1(\frac{E_0^T t_1}{\|t_1\|^2})^T + E_1 \tag{6-4}$$

$$F_0 = t_1(\frac{F_0^T t_1}{\|t_1\|^2})^T + F_1 \tag{6-5}$$

where E_1 and F_1 are the residual matrices.

The third step, which is the iteration step, is to calculate the following set of components by using E_i and F_i to replace E_{i-1} and F_{i-1} and by repeating the calculating processes from Equation (6-1) to Equation (6-5). The Equations (6-4) and (6-5) are then transformed into the following [201, 203]:

$$E_0 = t_1(\frac{E_0^T t_1}{\|t_1\|^2})^T + \cdots + t_i(\frac{E_{i-1}^T t_i}{\|t_i\|^2})^T + E_i \quad (6\text{-}6)$$

$$F_0 = t_1(\frac{F_0^T t_1}{\|t_1\|^2}) + \cdots + t_i(\frac{F_{i-1}^T t_i}{\|t_i\|^2}) + F_i \quad (6\text{-}7)$$

where t_i is the score vector for E_{i-1}.

The fourth step is to check the stopping criterion, determine the number of latent variables and acquire the final regression correlation. The stopping criterion is determined using the one-at-a-time form of the cross-validation method as follows [201, 203]:

$$Q_h^2 = 1 - \frac{S_{PRESS,h}}{S_{SS,h-1}} \geq 0.0975 \quad (6\text{-}8)$$

$$S_{PRESS,h} = \sum_{i=1}^{n}(y_i - \hat{y}_{h(-i)})^2 \quad (6\text{-}9)$$

$$S_{SS,h} = \sum_{i=1}^{n}(y_i - \hat{y}_{hi})^2 \quad (6\text{-}10)$$

where $S_{PRESS,h}$ and $S_{SS,h}$ are the residual sum of squares according to the cross-validation method and according to all data sets, respectively, y_i is the actual value of the dependent variable in the ith subset, and $\hat{y}_{h(-i)}$ and $\hat{y}_{hi}$ are the predicted values of the dependent variable in the ith subset according to the one-at-a-time form of cross-validation method and according to all data sets, respectively. If $Q_h^2 \geq 0.0975$, then the iteration is continued because adding the new set of components can make a clear contribution to the prediction performance. If $Q_h^2 < 0.0975$ at the hth iteration, then the iteration is stopped. In the final step, the results are as follows [201, 203]:

$$F_0 = (\frac{F_0^T t_1}{\|t_1\|^2})E_0 w_1^* + \cdots + (\frac{F_{h-1}^T t_h}{\|t_h\|^2})E_0 w_h^* \quad (6\text{-}11)$$

$$f^* = \sum_{i=1}^{p}(\alpha_i \varepsilon_i) \quad (6\text{-}12)$$

$$\alpha_j = \sum_{h=1}^{p}(\frac{F_{h-1}^T t_h}{\|t_h\|^2})w_{hj}^* \quad (6\text{-}13)$$

$$w_h^* = \prod_{i=1}^{h-1}(I - w_i(\frac{E_{i-1}^T t_i}{\|t_i\|^2})^T)w_h \quad (6\text{-}14)$$

where f^* is the predicted value of the centered and normalized dependent variable, I is the identity matrix with size $n \times n$, and w_{hj}^* is the jth element of w_h^*. The final results are obtained by preforming the anti-operation of normalization.

6.3 Results and discussion

6.3.1 Validation of the sintered/slagging route

The proposed ash deposition indice uses (i) the amount of the corresponding ash composition to represent the initial slagging routes, and (ii) employ the liquidus temperature to predict the overall melting potential and to represent the sintered/slagging route. Although it is known that the liquidus temperature can be used to predict the ash fusion temperature [138, 209], it is still significant to validate using the liquidus temperature to represent the sintered/slagging route before employing the parameter.

Slagging experiments in an entrained flow reactor (EFR), which are available in the published literature [102, 116], are chosen in this investigation. The experiments were undertaken by using a deposition probe with a high surface temperature that is placed in the cross section and at the bottom of the EFR to

simulate a steady state of deposit formation on the heat exchanger which are governed mainly by the cross-flow flue gas streams [84, 102, 116]. Under the condition that the probe has a high surface temperature, condensation and thermophertic deposition is less important than the inertial impaction and hence the sintered/slagging routes are the main mechanisms under this condition [68]. The EFR operates with a furnace temperature of approximately 1300 °C and with an oxidizing atmosphere at the bottom [102, 116]. The slagging propensity is represented by using the energy-based growth rate (GRE), which is calculated as the mass of deposit divided by the product of the low heating value and the mass of the coal burned in the test [102, 116]. The relative repeatability error of the GRE can be up to approximately 20% in the test [102, 116]. Four different kinds of coals and their blending (ranging from anthracite to bituminous, sub-bituminous and lignite) were used [102, 116]. More details related to the experimental work can be found in [102, 116].

In order to compare the predicted slagging propensity by the liquidius temperature with the experimental slagging observation, it should be noted that one type of sub-butiminous coal in the original experiments were excluded in this study due to its much larger aerodynamic mean diameter than the other four types of coals used in this study [116]. Figure 6-3 shows the predicted results of the slagging propensity (represented by the slagging ranking, which is defined by the ranking of the GRE from low to high among the 10 cases) through using the liquidus temperature. The prediction results are in very good agreement with the experimental data, which means that it is suitable to employ the liquidus temperature to represent the sintered/slagging routes. This is because the liquidus temperature can indicate the melting potential of the main ash composition and the melting potential determines the sticking process in the sintered/slagging routes.

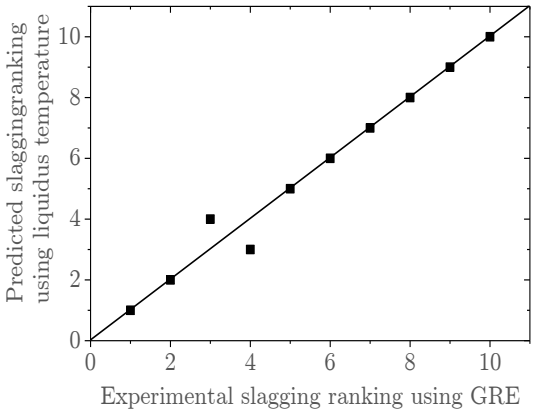

Figure 6-3 Comparison of the slagging propensity between the predicted ranking and experimental ranking.

6.3.2 Application to boilers

Two representative cases of utility coals have been investigated: (i) Case 1 is the Eastern US bituminous coals/blends combusted in T-fired boilers; (ii) Case 2 is the Western US sub-bituminous or lignite coals/blends combusted in opposed-wall boilers. In this section, the results of the newly developed slagging indice predictions for the two cases are analysed.

Case 1 contains 13 sets of coal combustion data (including data for 6 sets of coal blends); Case 2 contains 17 sets of coal combustion data (including data for 10 sets of coal blends). The range of coals and ash properties for the 30 sets of US coals/blends studies are presented in Appendix A. Bituminous coals have a higher Fe_2O_3, SiO_2 and Al_2O_3 contents compared to low rank coals but a lower content CaO and MgO contents. Both bituminous and sub-bituminous coals have low Na_2O and K_2O contents contrary to lignites that have higher levels of Na_2O. Slagging observations in boilers are evaluated by using not only the field performance data in the radiation and convection sections based on FEGT, soot blowing frequency increase, heat transfer rate, etc., but also periodic visual examinations of the deposit strength/ease of removal. The degrees of the slagging observations, ranging from no slagging to severe slagging, are represented using

the values from 0 to 1. Also the field slagging observations can be classified into four groups: low slagging < 0.4; 0.4 ≤ medium slagging ≤ 0.6; 0.6 < high slagging ≤ 0.9; severe slagging < 0.9.

Based on the ash compositions listed in Appendix A, the ash deposition indice for the bituminous type is calculated in Case 1 and the ash deposition indice for the lignitic type is calculated in Case 2. The training data, which cover fuels of low, medium and high slagging propensities, contain less than half of the total data set and therefore the testing data contain more than half of the total data set. The obtained linear correlations of the ash deposition indice, I_d, by performing the PLSR and Cross-Validation calculations are as follows:

$$\text{Case1:}\quad I\_d = 4.75 + 10^{-4} \times (-11.1 * LT_o - 7.85 * LT_r) - 2.06 \times 10^{-2} * (SiO_2 + Al_2O_3) + 10^{-2} \times (2.06 * Fe_2O_3 + 10.2 * Sulfur) \tag{6-15}$$

$$\text{Case2:}\quad I\_d = 2.19 + 10^{-4} \times (-5.79 * LT_o - 3.42 * LT_r) - 6.31 \times 10^{-3} * (SiO_2 + Al_2O_3) + 3.53 \times 10^{-3} * (CaO + MgO) + 7 \times 10^{-3} * (Na_2O + K_2O) \tag{6-16}$$

For both cases, the liquidus temperature and $SiO_2 + Al_2O_3$ have negative coefficients, which implies that the predicted slagging observation will decrease with an increase in the liquidus temperature and $SiO_2 + Al_2O_3$. However, the parameters related to the initial slagging routes (Fe_2O_3, $Sulphur$, CaO+MgO and Na_2O+K_2O) have a positive coefficient which means that the predicted slagging/fouling observation increases with a higher content of these four parameters.

Figure 6-4 shows a comparison of the predicted and experimental slagging observations and the prediction errors. It can be found that, (i) the predicted results are close to the experimental results for both the training data and testing data, and (ii) the slagging predictions of the coal blends do not largely deviate

from the slagging observations. It is difficult to obtain a very close agreement between the predictions and the experimental value of the slagging propensities. This is because the slagging indice is developed through an ash chemistry aspect and, the combustion condition in furnaces is ignored. It should be noted that, for Case 1, several predicted slagging values are larger than one, which represents the severe slagging issue. In addition, the uncertainty of the predictions may be attributed to the number in the training data set. In the calculations, the numbers from 5 to 9 have been tested. The predicted average relative errors range from 16.8% to 19.3% for Case 1 and from 9.0% to 9.4% for Case 2, which indicates that the prediction performance may not be greatly affected by the number of the training data. Figure 6-5 illustrates a comparison between the predicted performance of the ash deposition indice, I_d in this study and some of the conventional slagging indices based on the ranked slagging observations. It can be observed that the ranking for the accuracy of the prediction performance from high to low is $I\_d > I\_Fe_2O_3 > I\_Si = I\_B/A > I\_B/A \times S > I\_Si/Al$ for Case 1 and $I\_d > I\_Si > I\_Si/Al > I\_Fe_2O_3 > I\_B/A > I\_B/A \times S$ for Case 2, where $I\_Fe_2O_3$, I_Si, I_B/A, $I\_B/A \times S$ and I_Si/Al represent the slagging indice of Fe_2O_3 content, $SiO_2/(SiO_2 + Fe_2O_3 + CaO + MgO)$, $Basic\ content/Acid\ content$, $I\_B/A \times\ sulfur\ content$ and SiO_2/Al_2O_3 [102, 116]. It was found that 11 out of 13 coals with an accuracy of 85% and 15 out of the 17 coals with an accuracy of 88% evaluated in Cases 1 & 2, respectively, were accurately predicted for slagging propensity by the proposed indice, I_d. In contrast, conventional slagging indices have limited success rates, ranging from 1 to 7 for Case 1 (out of 13) with accuracies ranging from 8% to 54% and 0 to 12 for Case 2 (out of 17) with accuracies ranging from 0% to 71%. Therefore, the indice built by considering multi-slagging routes yields a higher success rate in classifying the overall slagging/fouling potential in boilers than that of the typical slagging indices.

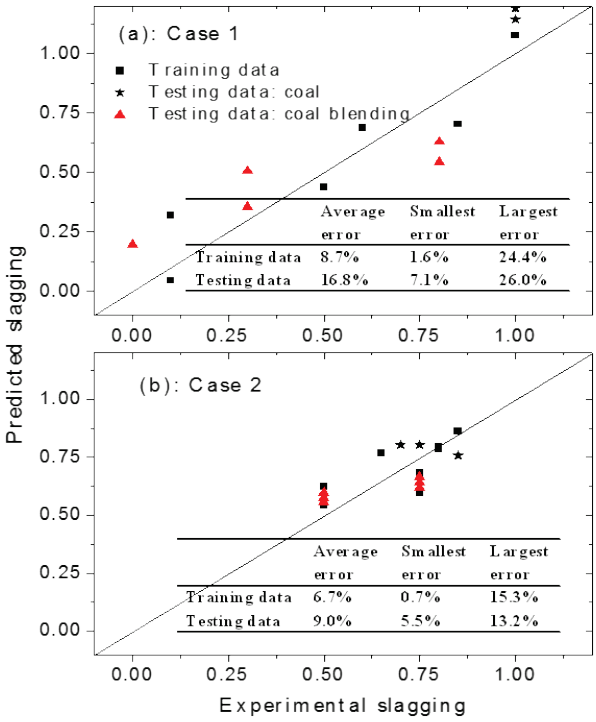

Figure 6-4 Comparison of the slagging propensity between the predicted and experimental values and the prediction errors.

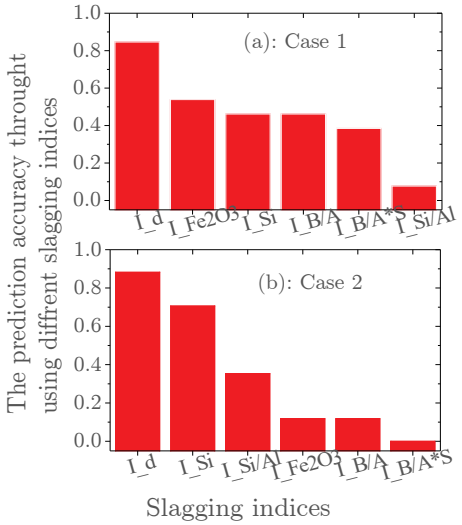

Figure 6-5 Comparison of the prediction performance among the *I_d* and five slagging indices.

In addition, Figure 6-6 shows the predicted values using the new indice for Case 1 and Case 2 defined in Equation (6-15) and (6-16) earlier versus the field slagging observations. It can be observed that the predicted value in the proposed ash deposition indice increases with the increasing value of the experimental slagging

observations, which indicates that both the initial slagging routes and the sintered/slagging route increase with the field slagging/fouling observations classification. This is because the coexistent dual slagging (alkali vapour induced slagging and the overall melting induced slagging) inevitably occurs in boilers and dictates the overall slagging behaviours [210]. In addition, due to the negative coefficients in the correlations of the developed slagging indices the predicted values (liquidus temperature and SiO_2+Al_2O_3) are negative.

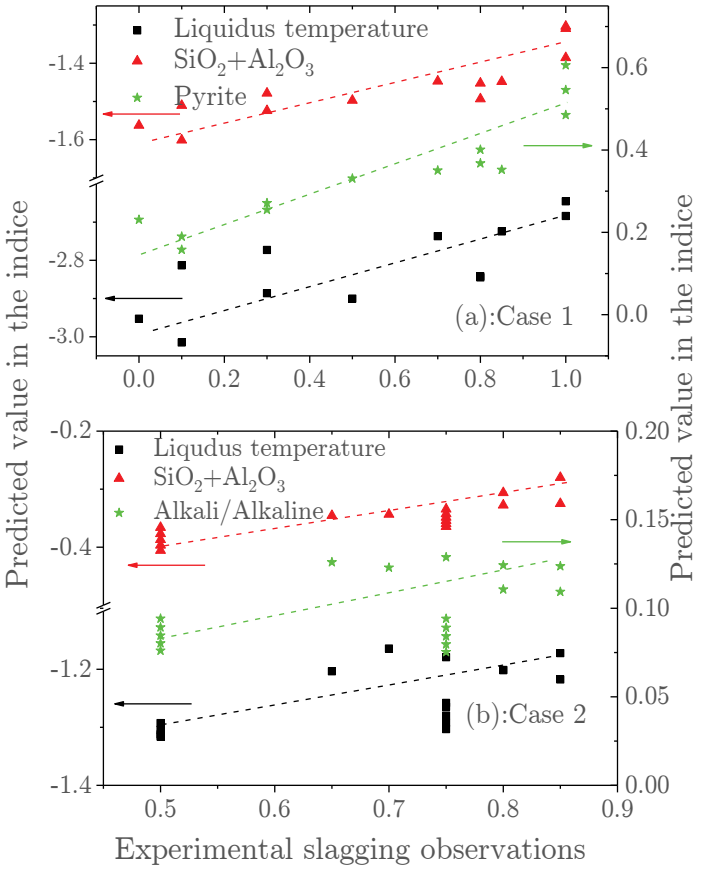

Figure 6-6 The predicted values in the proposed indice by the Liquidus temperature, SiO_2+Al_2O_3, pyrite for Case 1, and alkali+alkaline for Case 2 versus the field slagging observations.

6.3.3 Sensitivity of the method

Adding mineral additives is common practice in order to control the slagging and fouling problems in boilers. Therefore, the influence of adding acid components

to coals that show higher deposition potential was investigated by using the developed ash deposition indices in order to test the sensitivity of the developed method.

Either SiO_2 or Al_2O_3 was added as an additive to three easy slagging/fouling US coals and the predicted values of the indice are plotted against the added SiO_2 or Al_2O_3 content of the fuel and the ratio SiO_2/Al_2O_3 as shown in Figure 6-7. The sensitivity study indicates that by adding either SiO_2 or Al_2O_3 can reduce the predicted slagging potential. This is because the added acid components could reduce the melting potential due to the increase in the liquidus temperature. In addition, the acid components could capture the alkali/alkaline vapour phase to decrease the condensation potential. Also the analysis shows that the value of the predicted slagging potential decreases more rapidly by using Al_2O_3 than when adding SiO_2. Van Dyk et al. [106] and Li et al. [211] also found that Al_2O_3 is more effective than SiO_2 due to its higher ability to increase the ash fusion temperature than that of SiO_2. However, the analysis shown in the right section of Figure 6-8, indicates an opposite trend corresponding to the ratio SiO_2/Al_2O_3 when adding SiO_2 compared to adding Al_2O_3. It is noticed that Song et al. [209] found that ash fusion temperatures (AFTs) are increased with increasing the ratio SiO_2/Al_2O_3 from the fusion experiments and chemical equilibrium calculations. However, Liu et al. [46] found that AFTs are decreased with increasing the ratio SiO_2/Al_2O_3 from the fusion experiments. This is because, see Ref. [209], the SiO_2 was added into the ash with a relatively low CaO content (approximately 15%) and adding the SiO_2 can lead AFTs to move from the low temperature region into the high temperature region [209]; However, see [212], when the SiO_2 is added into the ash with relatively high CaO content (approximately 40%) the added SiO_2 can react with CaO to generate the low-melting anorthite and gehlenite and this leads the AFTs to move from a high temperature region to a low temperature region [212]. In this study, all the three coals with higher slagging propensity

have relatively low/medium CaO content (ranging from 2.9% to 21.8%) and adding either SiO_2 or Al_2O_3 could increase the liquidus temperature from the chemical equilibrium calculations.

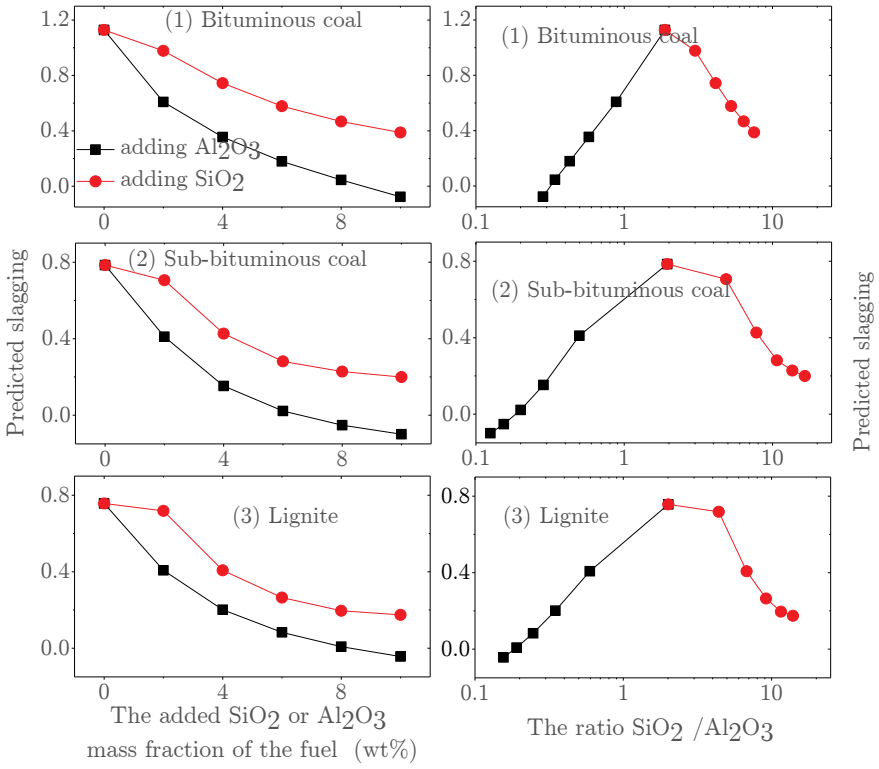

Figure 6-7 Values of the proposed indice as a function of the added SiO_2 or Al_2O_3 mass fraction of the fuel and as a function of the ratio SiO_2/Al_2O_3.

In addition, further calculations, using chemical equilibrium methods, were undertaken to investigate the influence of the ratio SiO_2/Al_2O_3 on the melting potential. In the calculations: (i) in addition to the three coals tested in this study, coal ashes from [209] and [212] were chosen; (ii) the ratio SiO_2/Al_2O_3 is considered by changing the individual amounts of SiO_2 and Al_2O_3 simultaneously, holding the total sum (SiO_2 + Al_2O_3) as constant. Figure 6-8 shows the effect of the ratio SiO_2/Al_2O_3 on the liquidus temperature. It can be observed that, basically, the liquidus temperature decreases with increasing the ratio SiO_2/Al_2O_3

for all coal ashes, which means that ash fusion and slagging potential are increased with an increase in the ratio SiO_2/Al_2O_3. This is because the Al_2O_3 content increases with a decrease in the ratio SiO_2/Al_2O_3 when the total amount of SiO_2 and Al_2O_3 is not changed and the melting temperature could increase more rapidly with higher content of Al_2O_3. Careful consideration of all scenarios is required when using the parameter (ratio SiO_2/Al_2O_3) to predict the melting behaviours and slagging potential. Both the ash composition of the original coal and the way in which the ratio SiO_2/Al_2O_3 changes can influence the effect of the ratio SiO_2/Al_2O_3 on the fusion and slagging potential.

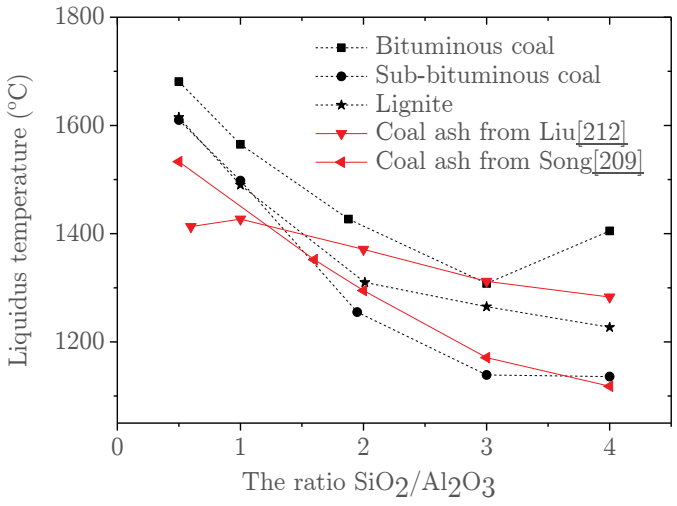

Figure 6-8 Effect of the ratio SiO_2/Al_2O_3 on the liquidus temperature.

6.3.4 Remarks on the implementation of the method

In this chapter, a new method is developed based on the ash chemistry, without considering the complex particle transport and rebounding mechanisms, to build an ash deposition indice for firing US coals and their blends in boilers. The predicted results of the developed indice and five other existing slagging indices have been compared with the slagging observations for the 30 US coals/blends with a history of ash deposition issues. The indice built by using the proposed method yields a higher success rate in classifying the overall slagging/fouling

potential in boilers than those existing slagging indices. It is postulated that this method has a potential to be used as an alternative tool to build an ash deposition indice for industrial use with a better prediction performance compared to existing slagging indices. In addition, an advantage of this method is that the newly developed indice based on the known slagging/fouling history from multiple boiler units makes it more suitable for different boiler configurations and coal types, although some of the aspects regarding the ash chemistry need to be further investigated in order to improve the accuracy and extend the application range of the proposed method. Without addressing the specific conditions in a boiler, the performance of a predictive method could be less accurate [23]. The index reported in this study does not consider the combustion conditions explicitly in its formulation and this may be limited to the conditions observed in the units used to validate the index. Incorporating changes in combustion conditions could be an ideal path moving ahead to further improve the accuracy of this index.

It should be noted that the initial slagging route caused by the pyrite is represented by the contents of Fe_2O_3 and sulphur for US coals since they are known to contain iron, predominantly in the form of pyrite [22]. The distribution of pyrite within the coal samples is important to predict the ash deposition behaviour. Excluded pyrite could generate molten phases under lower temperature and under a reducing atmosphere [13, 14, 21, 27]. High density and the spherical shape of the molten phases facilitate their arriving at the furnace wall surface [13]. The included pyrite may react with the clay or quartz minerals to generate the aluminosilicate slag [14, 22]. However, siderite may be the dominant iron-bearing mineral for many other coals, such as South African and Australian coals. Although some researchers considered that in addition to pyrite, its contribution to deposit formation [22, 68] needs further investigation. Furthermore, it should be noted that this study accounts for all of the

alkaline/alkali species as active contributors to condensation formation and this is primarily for low rank coals where the alkaline/alkali species are organically-bound [23, 27]. However, not all of the alkaline/alkali components are considered as active forms, except for those leachable by water and weak acids [23, 113, 210]. Taking into consideration these factors could increase the accuracy of predicting deposit formation from alkali condensation. Also, it should be noted that the ash loading, which can affect the deposit accumulation in boilers [50], is not considered in the proposed slagging indice because there is no significant difference in the ash loading for the tested US coals. However, if there exists a great difference in the ash loading, the parameter should be considered in the prediction model and this can be done by using the value of the ash compositions/ ash loading to replace the existing value of the ash compositions [50, 136].

6.4 Conclusions

A novel method to build an indice is developed and used for predicting the overall slagging/fouling potential of coal/blends combustion in boilers. The method couples the initial slagging route caused either by pyrite or by alkaline/alkali components and the sintered/slagging route. The initial slagging route is predicted based on the corresponding ash components and the sintered/slagging route is predicted based on the overall melting potential using the liquidus temperature calculated from chemical equilibrium methods. Utilizing the available slagging observation data from US coal fired boilers, PLSR coupled with the cross validation method was employed to develop the new ash deposition indice.

It should be noted that both SiO_2 and Al_2O_3 can reduce the slagging potential, but the drop in slagging propensity is more significant by adding Al_2O_3 compared to SiO_2 as confirmed by the chemical equilibrium calculations. Finally, using the

ratio SiO_2/Al_2O_3 alone to predict the melting behaviours and slagging potential of coals is inaccurate owing that the ratio SiO_2/Al_2O_3 alone cannot dictate the overall melting behaviour. The proposed method has been validated against the field performance of slagging observations on 30 sets of US coals/blends combusted in utility boilers. The results obtained indicate that the developed indice shows a much higher success rate for ranking the overall slagging potential in boilers than the other five conventional slagging indices.

Chapter 7: Conclusions and future work

In the first half of this century, pulverised coal-fired power generation technologies will play a significant role in satisfying the electricity demands worldwide, especially for the developing countries. Fuel flexibility (coal blending, co-combustion, new fuels, etc.) is one of the major factors in determining the operation of the power stations. However, changing fuels may lead to the change in the ash deposition behaviours. Ash deposit formation can reduce the heat transfer and it may even trigger the unscheduled shutdown of the combustion systems. Therefore, development of ash deposition prediction models is very significant and useful in order to maintain the fuel flexibility of the combustion systems and ensure an efficient operation and optimization of boilers. The work in this thesis has focused on developing models through using CFD methods and ash deposition indices in order to predict the ash deposit formation and its propensity. The summary of the conclusions is presented in Section 7.1 and the recommendations for future work are discussed in Section 7.2.

7.1 Conclusions

7.1.1 Steady CFD prediction of ash deposit formation

Predicting particle impaction and sticking behaviours is significant in order to accurately estimate the ash deposit formation in CFD methods. Accurate prediction of the particle impaction behaviour is a prerequisite step for predicting ash deposit formation and validating the accuracy of the particle sticking model. However, an extremely fine grid is needed to accurately predict the particle

impaction behaviour and this requirement is difficult to be satisfied in the simulation of an industrial boiler. In Chapter 4, a new ash deposition model has been developed which is based on the revised particle impaction model and particle sticking model.

Reasonably good agreement was obtained between the predicted results and the experimental data and it is demonstrated that the proposed particle impaction model, which takes account of both the effect of particle interception and errors in the particle impaction prediction when a coarse computational mesh is employed, can reduce the numerical related errors in the ash deposition prediction using a reasonable coarse computational mesh for the combustion process simulation. In addition, through using the revised particle impaction model, particles with small Stokes numbers (especially less than one) require a significant correction to the particle impaction efficiency when a reasonably coarse mesh is employed. The impact correction factor approaches unity for particles with larger Stokes number (greater than one) and therefore using a relatively coarse mesh could be acceptable.

The deposition rate is determined by both the particle impaction and sticking behaviours. With an increase in the co-firing ratio of the PKE, the deposition efficiency firstly increases in the co-firing ratio range 0% to 40% and then reduces at the co-firing ratio of 60%. This is because the overall impaction efficiency increases with increasing the co-firing ratio, whilst the overall stickiness efficiency reduces at the co-firing ratio of 60% because of the melting behaviours of the fuels.

7.1.2 Dynamic CFD prediction on ash deposit formation

Ash deposit formation behaviour on a cooled ash deposition probe is time-dependent. This is because the particle impaction and sticking behaviours are time-dependent during the ash deposit formation process. In addition, the

contribution of different ash deposition mechanisms on the deposit formation is dependent on the local thermal boundary conditions near the deposition surface. In Chapter 5, a dynamic ash deposition model has been developed. The developed dynamic ash deposition model is based on the inertia impaction, the thermophoresis and the direct alkali vapour condensation and incorporates the influence of the heat transfer rate.

By using the dynamic ash deposition model, as the deposition time increases, the particle impaction efficiency decreases and the sticking efficiency increases due to the thermophoresis and the local temperature conditions. This suggests that small particles are more difficult to impact on the deposition surface in the later stages than in the early stages and the impacting particles are easier to stick on the deposition surface in the later stages than in the early stages.

The main ash deposit formation is dictated by the inertia impaction and the thermophoresis under high furnace temperatures for the Zhundong lignite combustion while the deposition caused by the direct alkali vapour condensation is less significant. The heat flux through the deposition probe significantly decreases at first and then slowly decreases as the deposit builds up due to the variation of the deposit surface temperature and the deposit thermal conductivity. A higher furnace temperature can increase the deposition rate because of the higher particle sticking efficiency. In addition, the heat flux through the deposition probe is larger under a higher furnace temperature.

7.1.3 Slagging indice

The ash deposition indice provides a relatively simple and practical method to estimate the ash deposition propensities for engineers without much CFD knowledge. It can be very useful to develop a method to build the ash deposition indice based on the multi-slagging routes and the overall slagging observation data directly from the utility boilers. In Chapter 6, a new method has been

developed for the ash deposition indice to predict the overall slagging propensities for coals/blends combustion in utility boilers.

Based on the multi-slagging routes (the initial slagging routes and the sintered/slagging route), the developed indice yields a higher success rate in classifying the overall slagging/fouling potential in boilers than some of the typical slagging indices. Both SiO_2 and Al_2O_3 can reduce the slagging potential, but the drop in slagging propensity is more significant by adding Al_2O_3 compared to SiO_2. Using the ratio SiO_2/Al_2O_3 alone to predict the melting behaviours and slagging potential of coals is inaccurate, and this is due to the ratio SiO_2/Al_2O_3 alone not being able to dictate the overall melting behaviour.

7.2 Recommendations for future work

7.2.1 CFD methods

(i) Currently, the ash deposition models have been applied for the lab-scale and pilot-scale combustors. Due to the lack of utility boiler data (boiler design, operational conditions, etc.), CFD simulation of ash deposit formation in boilers has not been investigated in this thesis. Currently, although there are some publications on modelling ash deposit formation in boilers, most of the particle sticking models cannot consider the multi conditions in the boilers. The gas flow and temperature conditions and particle states are very different between the radiation and the convection sections. Therefore, a further development and validation of the ash deposition models for full-scale boilers is suggested.

(ii) Biomass, which is a sustainable fuel, unlike fossil fuels, is regarded as being CO_2-neurality. Therefore, the development of ash deposition models for biomass combustion is suggested. Biomass has significant different inorganic compositions than those in coal. Therefore, the biomass particle properties (particle size, ash composition, etc.) and the sticking process of biomass particles should be carefully

taken into consideration in order to develop the ash deposition model. Although the ash deposition model for co-combustion of South African coal (SAC) and palm kernel expeller and South African coal has been developed in the current studies, ash deposition models should be developed and validated for more biomass types. On the other hand, oxy-fuel combustion technology is regarded as a highly interesting option for CO_2 capture among the different carbon capture technologies. Uncertainties still exist in the ash deposit formation due to the difference in the combustion conditions in oxy-fuel combustion (temperature, velocity, and gas atmosphere, etc.). Therefore, the current ash deposition models should be further developed to include these factors for oxy-fuel combustion.

(iii) Currently, the dynamic ash deposition model neglects the shape of the deposit and its influence on the deposit boundary conditions. Also, the variance of the deposit shape may have an influence on the particle impaction and sticking behaviours. Therefore, the further development of the dynamic ash deposition model is suggested to include the change of deposit shape by using the dynamic meshing strategy.

(iv) Ash deposit formation is dictated by the gas temperature and velocity, particle properties (particle diameter, density, velocity, and ash composition), and deposit surface condition (surface temperature and deposit properties). It is very interesting to build a connection and relationship between (i) the fly ash properties and gas properties, and (ii) the deposit properties based on the experimental work and the modelling work. Ideally, it can be very practical and useful to only use the information of the fly ash properties and the gas properties to predict the ash deposition properties without undertaking complicated deposition experiments.

(v) Ash shedding is another significant physical phenomenon in the later stage of ash deposit formation. It can be caused by the liquid flow at the deposit surface,

erosion, gravity shedding, soot blowing, etc. It is very important to develop an ash shedding sub-model in the ash deposition model to determine the stable state of the ash deposit formation.

7.2.2 Ash deposition indice

Currently, the ash deposition indice uses the overall ash composition and divides coal ash into two ash types in order to assume the occurrence of different ash compositions in the coal. Therefore, it is suggested to apply the direct mineral composition in coal (to replace the overall ash composition) to better represent the multi-slagging routes. On the other hand, the combustion conditions in boilers is neglected as well in the current ash deposition indice, which may affect the accuracy of the current indice. Therefore, adding the combustion conditions of the utility boilers (furnace temperature, energy input/boiler size, flue gas composition, etc.) into the current ash deposition indice is suggested.

Appendix A

Table A-1 Coal ash properties and slagging observations (* represents coal blending).

data	Sulphur (*ar %*)	Ash (%)							Slagging data
		SiO_2	Al_2O_3	Fe_2O_3	CaO	MgO	K_2O	Na_2O	
1	0.87	55.91	28.36	6.16	1.43	0.95	2.52	0.28	0.1
2	0.44	55.48	24.02	6.47	3.94	0.67	1.22	1.28	0.1
3	1.4	50.12	28.68	11.28	2.35	0.94	2.28	0.57	0.5
4	1.25	53.14	23.01	13.06	2.25	1.01	2.6	1.13	0.7
5	2.69	52.46	20.46	16.78	2.34	0.89	2.31	0.7	1
6*	1.57	53.97	22.24	11.63	3.14	0.78	1.77	0.99	0.85
7	2.38	46.08	22.83	14.97	5.56	1.09	1.55	0.98	1
8	2.26	44.77	23.83	22.12	2.79	1	2.53	0.26	1
9*	0.97	55.22	27.02	7.88	1.64	0.97	2.54	0.49	0
10*	1.07	54.53	25.68	9.61	1.84	0.98	2.56	0.7	0.3
11*	0.85	54.31	23.51	9.77	3.1	0.84	1.91	1.2	0.3
12*	1.6	50.34	26.1	14.14	2.11	0.98	2.53	0.27	0.8
13*	1.78	54.19	24.41	11.47	1.89	0.92	2.42	0.49	0.8
14	0.35	36.05	8.32	5.46	15.42	3.99	0.73	7.16	0.85
15	0.31	34.31	17.6	5.56	16.97	3.92	0.52	6.7	0.8
16	0.38	36.53	18.24	5.59	16.73	3.74	0.42	7.26	0.65
17	0.28	32.17	16.36	4.03	21.92	6.47	0.51	0.98	0.8
18*	0.71	41.8	22.5	8.51	13.79	2.82	1.46	1.03	0.5
19*	0.48	38.19	19.83	7.28	18.39	3.7	1.06	1.24	0.5
20*	1.15	39.12	18.66	14.73	14.22	2.79	1.13	1.04	0.75
21*	0.7	36.63	17.65	10.69	18.73	3.7	0.87	1.26	0.75
22	0.36	35.88	17.14	5.27	18.55	3.92	0.46	6.61	0.75
23	0.38	37.69	16.74	5.43	17.67	4	0.3	6.34	0.7
24	0.25	34.4	17.1	5.9	21.8	5	0.5	1.6	0.85
25*	0.65	40.97	21.89	8.23	14.85	3.02	1.37	1.07	0.5
26*	0.59	40.1	21.24	7.93	15.96	3.23	1.27	1.13	0.5
27*	0.54	39.17	20.55	7.62	17.14	3.46	1.17	1.18	0.5
28*	1.03	38.54	18.43	13.79	15.27	3	1.07	1.09	0.75
29*	0.92	37.94	18.18	12.81	16.36	3.22	1.01	1.14	0.75
30*	0.81	37.3	17.92	11.77	17.51	3.46	0.94	1.2	0.75

Appendix A

Appendix B

This appendix outlines the algorithm of the dynamic ash deposition model used in the User Defined Functions. It contains the submodels to predict the deposition rate and deposit properties, which provides the guideline to reproduce the dynamic ash deposition model.

B1 Deposition rate

The deposition rate is calculated by the deposition by the inertia impaction, the thermophoretic force and the direct alkali vapour condensation. Therefore, the deposition rate is the summation of the deposition of these deposition mechanisms [125, 127]:

$$\frac{dR_{dep}}{dt} = A_{arrival}\eta_{stick} + I_v \tag{B-1}$$

where $A_{arrival}$ is the flow flux of the arrival ash particles due to the inertial impaction and thermophoretic force, η_{stick} is the sticking efficiency and I_v is the vapour condensation mass flux.

B1.1 Sticking efficiency

The sticking efficiency, η_{stick}, is determined by the melt fraction of the particles and the melt fraction of the deposit on the probe surface [91, 124]:

$$\eta_{stick} = \eta_p(T_p) + (1 - \eta_p(T_p))\eta_s(T_s) \tag{B-2}$$

where $\eta_p(T_p)$ is the melt fraction of the particles at the particle temperature (T_p), and $\eta_s(T_s)$ is the melt fraction of the deposit on the probe at the deposit surface temperature (T_s). The melt fraction is determined by the thermodynamic equilibrium calculations based on the minimization of the Gibbs free energy from

the system subject to the mass balance constraints [177, 178]. The thermodynamic software package FactSage 7.0 is employed to perform the thermodynamic equilibrium calculations.

The calculations were performed for a temperature range between 500 K and 1750 K at a temperature interval of 20 K and at atmospheric pressure. The ash composition determined by the mineral quantity analysis of the low temperature ash and the air composition were used as the reactants. Their amounts are dictated by the inlet air/fuel ratio. It should be noticed that, in order to calculate the melt fraction of the deposit, its ash composition may be different from that of the ash particles due to the direct condensation of the alkali phases. Therefore, the local ash composition of the deposit is determined by the deposit mass of the particle deposition and the direct alkali vapour condensation calculated from the CFD results. The possible products selected are the entire compound species (ideal gases and pure solids) from the ELEM, FToxid, FTsalt and FACTPS databases. The melt phases chosen in the calculations were the 'SLAGB' (covers liquid oxide solutions of SiO_2, Fe_2O_3, $Fe_2(SO_4)_3$ and, Na_2O, Na_2SO_4, CaO, and $CaSO_4$) and 'SALTB' (covers liquid salt solutions of NaCl, NaOH, $CaCl_2$, $Ca(OH)_2$, $FeCl_3$, $Fe(OH)_3$, etc.) with possible 2-phase immiscibility. An example of the prediction results of melt fraction for the original coal ash is shown in Figure B-1. The predicted results of the melting behaviours of ash particles and deposits are incorporated into the ash deposition model in order to predict the melting behavior of particles and deposit surface.

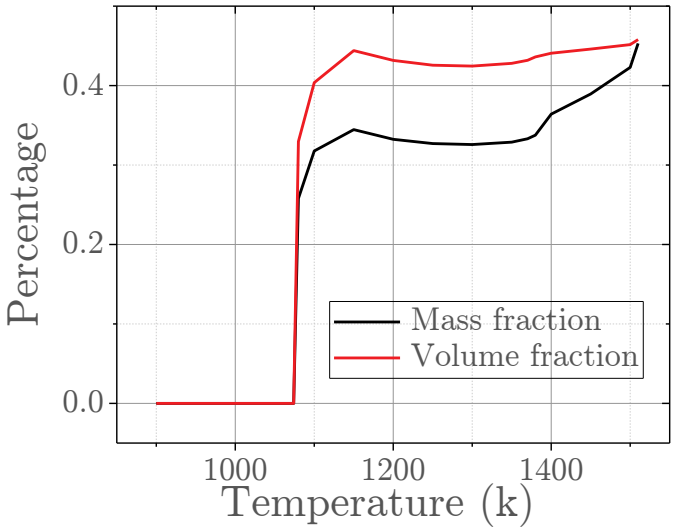

Figure B-1 Melt fraction curve of the original coal ash as a function of temperature.

B1.2 Condensation

Based on the assumption that the alkali phase reactions are chemical equilibrium reactions because the furnace temperature is high enough for equilibrium to be reached quickly [127]. The vapour condensation mass flux, I_v, can be determined by the following equations [127, 194, 213, 214]:

$$I_v = Sh(T_g)\frac{(D_v(T_g)D_v(T_s))^{1/2}}{D_h R_g}\left[\frac{p_v(T_g)}{T_g} - \frac{p_{v,s}(T_s)}{T_s}\right] \tag{B-3}$$

$$Sh(T_g) = 0.023 Re^{0.8} Sc(T_g)^{0.4} \tag{B-4}$$

$$Sc(T_g) = \mu_g/(\rho_g D_v(T_g)) \tag{B-5}$$

$$D_v(T) = 0.8 \times 1.781 \times 10^{-10} \times T^{1.88} \tag{B-6}$$

$$p_{v,s}(T_s) = 10^5 \times 10^{(3.56682 - \frac{5200.904}{T_s - 317.409})} \tag{B-7}$$

where $Sh(T_g)$ is the Sherwood number, $Sc(T_g)$ is the Schmidt number, Re is the Reynold number, $D_v(T)$ is the vapour diffusivity at the flue gas temperature (T_g)

or deposit surface temperature (T_s), $p_v(T_g)$ is the partial pressure of the alkali vapour, $p_{v,s}(T_s)$ is the saturation vapour pressure, D_h is the hydraulic diameter of the flow channel (0.35m, equal to the inner diameter of the furnace), and R_g (142.3 J/(kg*K)) is the specific gas constant. In this study, only the alkali vapour of sodium chloride (NaCl) is considered since NaCl is the major alkali vapour phase species of ZD lignite studied according to the chemical equilibrium calculation. HCl is considered in the gas species in order to predict the alkali vapour composition during the chemical equilibrium calculations.

B2 Deposition properties

The deposit properties (porosity, thermal conductivity, deposit thickness, deposition surface temperature, etc.) could change with the deposit growth.

A correlation based on the temperature and deposit composition is employed to calculate the deposit porosity as follows [65, 91, 94]:

$$\varepsilon_{deposit} = 1 - \left[(1-\varepsilon_0) + \frac{V_{liq}}{V_{solid}}(1-\varepsilon_0)\right] \tag{B-8}$$

where $\varepsilon_{deposit}$ is the deposit porosity, ε_0 with a value of 0.8 is the initial deposit porosity, V_{liq} is the volume of the liquid phase, and V_{solid} is the volume of the solid phase. Calculation of the volume fraction of the liquid phase and solid phase is performed by using chemical equilibrium methods and then estimating the density of the liquid phase as a function of the chemistry using the method described by Mills et al. [215].

For the initial layer, the thermal conductivity is given a value of 0.14 W/m-k [192, 193] and then the measured thermal conductivity from [148] is employed in this study, which shows that the thermal conductivity will increase with the deposit growth.

The deposit thickness, $L_{deposit}$, can be described as follows:

$$\frac{dL_{deposit}}{dt} = \frac{A_{arrival}\eta_{stick} + I_v}{\rho_p(1-\varepsilon_{deposit})} \tag{B-9}$$

The deposit surface temperature, T_{ds}, can be calculated based on the total heat flux to the wall (q_{total}) predicted from the CFD calculations, the deposit thickness $(L_{deposit})$ and the thermal resistance coefficient (R_{total}) are as follows [91, 95]:

$$T_{ds} = q_{total}R_{total} + T_{oil} \tag{B-10}$$

$$R_{total} = \frac{L_{deposit}}{k_{deposit}} + \frac{L_{steel}}{k_{steel}} + \frac{1}{h_{oil}} \tag{B-11}$$

where $k_{deposit}$ is the thermal conductivity of the deposit, T_{oil} with a value of 503 K is the temperature of the cooling oil, L_{steel} with a value of 0.0065 m and k_{steel} with a value of 48 W/(K*m) are the thickness and the thermal conductivity of the stainless steel probe, respectively, and h_{oil} with a value of 3590 W/(m^2*K) is the heat transfer coefficient of the cooling oil.

Appendix B

List of references

[1] BP. Statistical Review of World Energy 2013. http://www.bp.com-/content/dam/bp/pdf/statistical review/statistical review of world energy 2013.pdf (10 October, 2016).

[2] BP. Energy Outlook 2035. http://www.bp.com/en/global/corporate/about-bp/energy-economics/energy-outlook/outlook-to-2035.html (10 October, 2016).

[3] Chu S., Majumdar A. Opportunities and challenges for a sustainable energy future. Nature, 2012; 488: 294-303.

[4] Fei Y. Computational fluid dynamics and process co-simulation applied to carbon capture technologies [D]. Doctoral Thesis, The University of Sheffield, 2015.

[5] Administration U.S.E.I. International Energy Outlook 2016. http://www.eia.gov/fore-casts/ieo/index.cfm (10 October, 2016).

[6] IEA. World Energy Outlook 2016[R]. International Energy Agency, 2016.

[7] Aydin G. The application of trend analysis for coal demand modeling. Energy Sources, Part B: Economics, Planning, and Policy, 2015; 10: 183-191.

[8] Van Putten J.G. Integrated modelling for improving the design and operation of steam power plants: With a focus on increasing their efficiency[D]. Doctoral Thesis, Delft University of Technology, 2008.

[9] Raask E. Mineral impurities in coal combustion: behavior, problems, and remedial measures, Taylor & Francis, 1985.

[10] Ngô C., Natowitz J.B. Fossil fuels and greenhouse effect, in: Our Energy Future, John Wiley & Sons, Inc., 2008, pp. 90-120.

[11] Weber R., Mancini M., Schaffel-Mancini N., Kupka T. On predicting the ash behaviour using Computational Fluid Dynamics. Fuel Processing Technology, 2013; 105: 113-128.

[12] Płaza P.P. The development of a slagging and fouling predictive methodology for large scale pulverised boilers fired with coal/biomass blends[D]. Doctoral Thesis, Cardiff University, 2013.

[13] Borio R.W., Narciso J.R.R. The use of gravity fractionation techniques for assessing slagging and fouling potential of coal ash. Journal of Engineering for Power, 1979; 101: 500-505.

[14] Bryers R.W. Fireside slagging, fouling, and high-temperature corrosion of heat-transfer surface due to impurities in steam-raising fuels. Progress in Energy and Combustion Science, 1996; 22: 29-120.

[15] Frandsen F. What is coal ash [R]. IFRF Online Combustion Handbook CF38, 2002.

[16] Falcone S.K., Schobert H.H. Mineral transformations during ashing of selected low-rank coals, in: Mineral Matter and Ash in Coal, American Chemical Society, 1986, pp. 114-127.

[17] Gaus-Liu X. High-temperature chlorine corrosion during co-utilisation of coal with biomass or waste[D]. Doctoral Thesis, University of Stuttgart, 2007.

[18] Zhang D. Ash fouling, deposition and slagging in ultra-supercritical coal power plants, in: Ultra-Supercritical Coal Power Plants, Woodhead Publishing, 2013, pp. 133-183.

[19] Vuthaluru H.B. Remediation of ash problems in pulverised coal-fired boilers. Fuel, 1999; 78: 1789-1803.

[20] Xu L., Liu J., Kang Y., Miao Y., Ren W., Wang T. Safely burning high alkali coal with kaolin additive in a pulverized fuel boiler. Energy & Fuels, 2014; 28: 5640-5648.

[21] Huffman G.P., Huggins F.E., Shah N., Shah A. Behavior of basic elements during coal combustion. Progress in Energy and Combustion Science, 1990; 16: 243-251.

[22] McLennan A.R., Bryant G.W., Bailey C.W., Stanmore B.R., Wall T.F. Index for iron-based slagging for pulverized coal firing in oxidizing and reducing conditions. Energy & Fuels, 2000; 14: 349-354.

[23] Borio R.W., Levasseur A.A. Coal ash deposition in boilers, in: Mineral Matter and Ash in Coal, American Chemical Society, 1986, pp. 288-302.

[24] Baxter L.L. Ash deposit formation and deposit properties. A comprehensive summary of research conducted at Sandia's combustion research facility[R]. Sandia National Laboratories Report, SAND2000-8253, 2000.

[25] Garba M.U., Ingham D.B., Ma L., Degereji M.U., Pourkashanian M., Williams A. Modelling of deposit formation and sintering for the co-combustion of coal with biomass. Fuel, 2013; 113: 863-872.

[26] Huffman G.P., Huggins F.E. Analysis of the inorganic constituents in low-rank coals, in: The Chemistry of Low-Rank Coals, American Chemical Society, 1984, pp. 159-174.

[27] Wall T.F. Mineral matter transformations and ash deposition in pulverised coal combustion. Symposium (International) on Combustion, 1992; 24: 1119-1126.

[28] Wall T.F., Creelman R.A., Gupta R.P., Gupta S.K., Coin C., Lowe A. Coal ash fusion temperatures—New characterization techniques, and implications for slagging and fouling. Progress in Energy and Combustion Science, 1998; 24: 345-353.

[29] Huggins F.E., Kosmack D.A., Huffman G.P. Correlation between ash-fusion temperatures and ternary equilibrium phase diagrams. Fuel, 1981; 60: 577-584.

[30] Seggiani M. Empirical correlations of the ash fusion temperatures and temperature of critical viscosity for coal and biomass ashes. Fuel, 1999; 78: 1121-1125.

[31] Yin C., Luo Z., Ni M., Cen K. Predicting coal ash fusion temperature with a back-propagation neural network model. Fuel, 1998; 77: 1777-1782.

[32] ASTM International. Standard test method for fusibility of coal and coke ash[S]. ASTM D1857/D1857M-16 2016.

[33] Dong Y.Z. Study on the slagging characterisitcs of main components in coal ash[D]. Master Thesis, Zhejiang University, 2006.

[34] Yang X., Huang J., Fang Y., Wang Y. Slagging characteristics of fly ash from anthracite gasification in fluidized bed. Journal of Fuel Chemistry and Technology, 2013; 41: 1-8.

[35] Frenkel J. Viscous flow of crystalline bodies under the action of surface tension. Journal of Physics, 1945; 9: 7.

[36] Al-Otoom A.Y., Elliott L.K., Moghtaderi B., Wall T.F. The sintering temperature of ash, agglomeration, and defluidisation in a bench scale PFBC. Fuel, 2005; 84: 109-114.

[37] Jing N., Wang Q., Cheng L., Luo Z., Cen K. The sintering behavior of coal ash under pressurized conditions. Fuel, 2013; 103: 87-93.

[38] Jing N., Wang Q., Cheng L., Luo Z., Cen K., Zhang D. Effect of temperature and pressure on the mineralogical and fusion characteristics of Jincheng coal ash in simulated combustion and gasification environments. Fuel, 2013; 104: 647-655.

[39] Li J., Zhu M., Zhang Z., Zhang D. A new criterion for determination of coal ash sintering temperature using the pressure-drop technique and the effect of ash mineralogy and geochemistry. Fuel, 2016; 179: 71-78.

[40] Haiying Z., Youcai Z., Jingyu Q. Utilization of municipal solid waste incineration (MSWI) fly ash in ceramic brick: Product characterization and environmental toxicity. Waste Management, 2011; 31: 331-341.

[41] Haykiri-Acma H., Yaman S., Kucukbayrak S. Effect of biomass on temperatures of sintering and initial deformation of lignite ash. Fuel, 2010; 89: 3063-3068.

[42] Al-Otoom A.Y., Bryant G.W., Elliott L.K., Skrifvars B.J., Hupa M., Wall T.F. Experimental options for determining the temperature for the onset of sintering of coal ash. Energy & Fuels, 1999; 14: 227-233.

[43] Al-Otoom A.Y., Elliott L.K., Wall T.F., Moghtaderi B. Measurement of the sintering kinetics of coal ash. Energy & Fuels, 2000; 14: 994-1001.

[44] Nowok J.W. Viscosity and phase transformation in coal ash slags near and below the temperature of critical viscosity. Energy & Fuels, 1994; 8: 1324-1336.

[45] Song W. Fusibility, flow charaeteristies and rheologieal properties of coal ash in the ultra-high temperature gasifier[D]. Doctoral Thesis, East China University of Science and Technology, 2011.

[46] Walsh P.M., Sayre A.N., Loehden D.O., Monroe L.S., Beér J.M., Sarofim A.F. Deposition of bituminous coal ash on an isolated heat exchanger tube: Effects of coal properties on deposit growth. Progress in Energy and Combustion Science, 1990; 16: 327-345.

[47] Kondratiev A., Jak E. Predicting coal ash slag flow characteristics (viscosity model for the Al_2O_3–CaO–'FeO'–SiO_2 system). Fuel, 2001; 80: 1989-2000.

[48] Kong L., Bai J., Li W., Wen X., Li X., Bai Z., Guo Z., Li H. The internal and external factor on coal ash slag viscosity at high temperatures, Part 1: Effect of cooling rate on slag viscosity, measured continuously. Fuel, 2015; 158: 968-975.

[49] Arvelakis S., Frandsen F.J. Rheology of fly ashes from coal and biomass co-combustion. Fuel, 2010; 89: 3132-3140.

[50] Degereji M.U., Ingham D.B., Ma L., Pourkashanian M., Williams A. Prediction of ash slagging propensity in a pulverized coal combustion furnace. Fuel, 2012; 101: 171-178.

[51] Vargas S., Frandsen F.J., Dam-Johansen K. Rheological properties of high-temperature melts of coal ashes and other silicates. Progress in Energy and Combustion Science, 2001; 27: 237-429.

[52] Urbain G., Cambier F., Deletter M., Anseau M.R. Viscosity of silicate melts. Transactions & Journal of the British Ceramic Society, 1981; 80: 139-141.

[53] Song W., Sun Y., Wu Y., Zhu Z., Koyama S. Measurement and simulation of flow properties of coal ash slag in coal gasification. AIChE Journal, 2011; 57: 801-818.

[54] Song W., Tang L., Zhu X., Wu Y., Rong Y., Zhu Z., Koyama S. Fusibility and flow properties of coal ash and slag. Fuel, 2009; 88: 297-304.

[55] Song W., Tang L., Zhu X., Wu Y., Zhu Z., Koyama S. Flow properties and rheology of slag from coal gasification. Fuel, 2010; 89: 1709-1715.

[56] Sarofim A.F., Howard J.B., Padia A.S. The physical transformation of the mineral matter in pulverized coal under simulated combustion conditions. Combustion Science and Technology, 1977; 16: 187-204.

[57] Black A.J. Oxy-fuel combustion for carbon capture using computational fluid dynamics[D]. Doctoral Thesis, University of Leeds, 2014.

[58] Doshi V., Vuthaluru H.B., Korbee R., Kiel J.H.A. Development of a modeling approach to predict ash formation during co-firing of coal and biomass. Fuel Processing Technology, 2009; 90: 1148-1156.

[59] Zbogar A., Frandsen F., Jensen P.A., Glarborg P. Shedding of ash deposits. Progress in Energy and Combustion Science, 2009; 35: 31-56.

[60] Laursen K., Frandsen F., Larsen O.H. Ash deposition trials at three power stations in Denmark. Energy & Fuels, 1998; 12: 429-442.

[61] Baxter L.L. Ash deposition during biomass and coal combustion: A mechanistic approach. Biomass and Bioenergy, 1993; 4: 85-102.

[62] Taha T.J., Stam A.F., Stam K., Brem G. CFD modeling of ash deposition for co-combustion of MBM with coal in a tangentially fired utility boiler. Fuel Processing Technology, 2013; 114: 126-134.

[63] Li G., Li S., Huang Q., Yao Q. Fine particulate formation and ash deposition during pulverized coal combustion of high-sodium lignite in a down-fired furnace. Fuel, 2015; 143: 430-437.

[64] Osborn G.A. Review of sulphur and chlorine retention in coal-fired boiler deposits. Fuel, 1992; 71: 131-142.

[65] Wang H., Harb J.N. Modeling of ash deposition in large-scale combustion facilities burning pulverized coal. Progress in Energy and Combustion Science, 1997; 23: 267-282.

[66] Li S. Char-slag transition during pulverized coal gasification[D]. Doctoral Thesis, University of Utah, 2010.

[67] Shao Y. Investigation of ash deposition during co-firing biomass/peat with coal in a pilot-scale fluidized-bed reactor[D]. Doctoral Thesis, The University of Western Ontario, 2011.

[68] Gibb W.H. The UK collaborative research programme on slagging pulverised coal-fired boilers: Summary of findings, in: L. Baxter, R. DeSollar (Eds.) Applications of Advanced Technology to Ash-Related Problems in Boilers, Springer US, 1996, pp. 41-65.

[69] Li J., Zhu M., Zhang Z., Zhang K., Shen G., Zhang D. Characterisation of ash deposits on a probe at different temperatures during combustion of a Zhundong lignite in a drop tube furnace. Fuel Processing Technology, 2016; 144: 155-163.

[70] Ansys. 15.0 Ansys Fluent Theory Guide, 2013.

[71] Chen L. Computational fluid dynamics simulations of oxy-coal combustion for carbon capture at atmospheric and elevated pressures[D]. Doctoral Thesis, Massachusetts Institute of Technology, 2013.

[72] Li W. The numerical simulation of coal powder combustion process and slagging in utility boiler[D]. Doctoral Thesis, North China Electric Power University, 2002.

[73] Degereji M.U. Predictive modelling of ash particle deposition in a PF combustion furnace[D]. Doctoral Thesis, University of Leeds, 2011.

[74] Marino T.A. Numerical analysis to study the effects of solid fuel particle characteristics on ignition, burning, and radiative emission[D]. Doctoral Thesis, The George Washington University, 2008.

[75] Garba M.U. Prediction of ash deposition for biomass combustion and coal/biomass co-combustion[D]. Doctoral Thesis, University of Leeds, 2012.

[76] Clements A.G. Modelling mercury oxidation and radiative heat transfer in oxy-coal environments[D]. Doctoral Thesis, University of Leeds, 2016.

[77] Smith I.W. The combustion rates of coal chars: A review. Symposium (International) on Combustion, 1982; 19: 1045-1065.

[78] Magnussen B.F. On the structure of turbulence and a generalized eddy dissipation concept for chemical reaction in turbulent flow[A]. In: 19th AIAA Aerospace Meeting, St. Louis, USA[C], 1981.

[79] Magnussen B.F., Hjertager B.H. On mathematical modeling of turbulent combustion with special emphasis on soot formation and combustion. Symposium (International) on Combustion, 1977; 16: 719-729.

[80] Spalding D.B. Mixing and chemical reaction in steady confined turbulent flames. Symposium (International) on Combustion, 1971; 13: 649-657.

[81] Israel R., Rosner D.E. Use of a generalized stokes number to determine the aerodynamic capture efficiency of non-stokesian particles from a compressible gas flow. Aerosol Science and Technology, 1982; 2: 45-51.

[82] Huang L.Y., Norman J.S., Pourkashanian M., Williams A. Prediction of ash deposition on superheater tubes from pulverized coal combustion. Fuel, 1996; 75: 271-279.

[83] Lokare S.S., Dunaway J.D., Moulton D., Rogers D., Tree D.R., Baxter L.L. Investigation of ash deposition rates for a suite of biomass fuels and fuel blends. Energy & Fuels, 2006; 20: 1008-1014.

[84] Weber R., Schaffel-Mancini N., Mancini M., Kupka T. Fly ash deposition modelling: Requirements for accurate predictions of particle impaction on tubes using RANS-based computational fluid dynamics. Fuel, 2013; 108: 586-596.

[85] Wacławiak K., Kalisz S. A practical numerical approach for prediction of particulate fouling in PC boilers. Fuel, 2012; 97: 38-48.

[86] Wieland C., Kreutzkam B., Balan G., Spliethoff H. Evaluation, comparison and validation of deposition criteria for numerical simulation of slagging. Applied Energy, 2012; 93: 184-192.

[87] Srinivasachar S., Senior C.L., Helble J.J., Moore J.W. A fundamental approach to the prediction of coal ash deposit formation in combustion systems. Symposium (International) on Combustion, 1992; 24: 1179-1187.

[88] Rushdi A., Gupta R., Sharma A., Holcombe D. Mechanistic prediction of ash deposition in a pilot-scale test facility. Fuel, 2005; 84: 1246-1258.

[89] Ai W., Kuhlman J.M. Simulation of coal ash particle deposition experiments. Energy & Fuels, 2011; 25: 708-718.

[90] Brach R.M., Dunn P.F. A mathematical model of the impact and adhesion of microsphers. Aerosol Science and Technology, 1992; 16: 51-64.

[91] Kær S.K., Rosendahl L.A., Baxter L.L. Towards a CFD-based mechanistic deposit formation model for straw-fired boilers. Fuel, 2006; 85: 833-848.

[92] Mu L., Zhao L., Yin H. Modelling and measurements of the characteristics of ash deposition and distribution in a HRSG of wastewater incineration plant. Applied Thermal Engineering, 2012; 44: 57-68.

[93] Mueller C., Selenius M., Theis M., Skrifvars B.-J., Backman R., Hupa M., Tran H. Deposition behaviour of molten alkali-rich fly ashes—development of a submodel for CFD applications. Proceedings of the Combustion Institute, 2005; 30: 2991-2998.

[94] Richards G.H., Slater P.N., Harb J.N. Simulation of ash deposit growth in a pulverized coal-fired pilot scale reactor. Energy & Fuels, 1993; 7: 774-781.

[95] Li B., Brink A., Hupa M. CFD investigation of deposition in a heat recovery boiler: Part II – deposit growth modelling. Progress in Computational Fluid Dynamics, an International Journal, 2009; 9: 453-459.

[96] Li B., Brink A., Hupa M. CFD investigation of slagging on a super-heater tube in a kraft recovery boiler. Fuel Processing Technology, 2013; 105: 149-153.

[97] Winegartner E.C. Coal fouling and slagging parameters, ASME, USA, 1974.

[98] Winegartner E., Rhodes B. An empirical study of the relation of chemical properties to ash fusion temperatures. Journal of Engineering for Power, 1975; 97: 395.

[99] J. A., Y. Q., Q. Z., P. H. Investigation on assessing slagging index of coal ash both at home and abroad. Power System Engineering, 1994; 10: 18.

[100] Lawrence A., Kumar R., Nandakumar K., Narayanan K. A Novel tool for assessing slagging propensity of coals in PF boilers. Fuel, 2008; 87: 946-950.

[101] Qiu J., Zhang X., Liu H., Wang Q., Li F., Zeng H. Grey clustering prediction for slagging potential of coal blends combustion. Combustion Science and Technology, 2002; 174: 51-70.

[102] Barroso J., Ballester J., Pina A. Study of coal ash deposition in an entrained flow reactor: Assessment of traditional and alternative slagging indices. Fuel Processing Technology, 2007; 88: 865-876.

[103] Reinmöller M., Klinger M., Schreiner M., Gutte H. Relationship between ash fusion temperatures of ashes from hard coal, brown coal, and biomass and mineral phases under different atmospheres: A combined FactSage™ computational and network theoretical approach. Fuel, 2015; 151: 118-123.

[104] Wei Q. Study on the calculation of chemical and phase equilibrium in complex system [D]. Doctoral Thesis, Ocean University of China, 2007.

[105] Van Dyk J.C., Melzer S., Sobiecki A. Mineral matter transformation during Sasol-Lurgi fixed bed dry bottom gasification – utilization of HT-XRD and FactSage modelling. Minerals Engineering, 2006; 19: 1126-1135.

[106] Van Dyk J.C., Waanders F.B. Manipulation of gasification coal feed in order to increase the ash fusion temperature of the coal enabling the gasifiers to operate at higher temperatures. Fuel, 2007; 86: 2728-2735.

[107] Van Dyk J.C., Waanders F.B., Hack K. Behaviour of calcium-containing minerals in the mechanism towards in situ CO_2 capture during gasification. Fuel, 2008; 87: 2388-2393.

[108] Van Dyk J.C., Waanders F.B., Benson S.A., Laumb M.L., Hack K. Viscosity predictions of the slag composition of gasified coal, utilizing FactSage equilibrium modelling. Fuel, 2009; 88: 67-74.

[109] Gilbe C., Lindström E., Backman R., Samuelsson R., Burvall J., Öhman M. Predicting slagging tendencies for biomass pellets fired in residential appliances: A comparison of different prediction methods. Energy & Fuels, 2008; 22: 3680-3686.

[110] Öhman M., Boman C., Hedman H., Nordin A., Boström D. Slagging tendencies of wood pellet ash during combustion in residential pellet burners. Biomass and Bioenergy, 2004; 27: 585-596.

[111] Werkelin J., Skrifvars B.-J., Zevenhoven M., Holmbom B., Hupa M. Chemical forms of ash-forming elements in woody biomass fuels. Fuel, 2010; 89: 481-493.

[112] Stam A., Livingston W., Cremers M., Brem G. Review of models and tools for slagging and fouling prediction for biomass co-combustion. Review article for IEA, 2010; Task 32: 1-18.

[113] Nutalapati D., Gupta R., Moghtaderi B., Wall T.F. Assessing slagging and fouling during biomass combustion: A thermodynamic approach allowing for alkali/ash reactions. Fuel Processing Technology, 2007; 88: 1044-1052.

[114] Chen C., Li Y., Li D. Optimum design of firing equipment in a large pulverized coal-fired boiler. Boiler Manufacturing, 1992; 2: 1-41.

[115] Tang X. Study on deposition indices and numerical simulation of fly ash deposition in coal combustion[D]. Master Thesis, Huazhong University of Science and Technology, 2009.

[116] Barroso J., Ballester J., Ferrer L.M., Jiménez S. Study of coal ash deposition in an entrained flow reactor: Influence of coal type, blend composition and operating conditions. Fuel Processing Technology, 2006; 87: 737-752.

[117] Degereji M.U., Gubba S.R., Ingham D.B., Ma L., Pourkashanian M., Williams A., Williamson J. Predicting the slagging potential of co-fired coal with sewage sludge and wood biomass. Fuel, 2013; 108: 550-556.

[118] Lundmark D., Mueller C., Backman R., Zevenhoven M., Skrifvars B.-J., Hupa M. CFD based ash deposition prediction in a BFBC firing mixtures of peat and forest residue. Journal of Energy Resources Technology, 2010; 132: 031003-031003.

[119] Haugen N.E.L., Kragset S., Bugge M., Warnecke R., Weghaus M. MSWI super heater tube bundle: Particle impaction efficiency and size distribution. Fuel Processing Technology, 2013; 106: 416-422.

[120] Haugen N.E.L., Kragset S. Particle impaction on a cylinder in a crossflow as function of Stokes and Reynolds numbers. Journal of Fluid Mechanics, 2010; 661: 239-261.

[121] Johnson K.L., Kendall K., Roberts A.D. Surface energy and the contact of elastic solids. Proceedings of the Royal Society of London A: Mathematical, Physical and Engineering Sciences, 1971; 324: 301-313.

[122] Lee B.E., Fletcher C.A.J., Shin S.H., Kwon S.B. Computational study of fouling deposit due to surface-coated particles in coal-fired power utility boilers. Fuel, 2002; 81: 2001-2008.

[123] Strandström K., Mueller C., Hupa M. Development of an ash particle deposition model considering build-up and removal mechanisms. Fuel Process Technol, 2007; 88: 1053-1060.

[124] Losurdo M., Spliethoff H., Kiel J. Ash deposition modeling using a visco-elastic approach. Fuel, 2012; 102: 145-155.

[125] Beckmann A.M., Mancini M., Weber R., Seebold S., Müller M. Measurements and CFD modeling of a pulverized coal flame with emphasis on ash deposition. Fuel, 2016; 167: 168-179.

[126] Yang X., Ingham D., Ma L., Williams A., Pourkashanian M. Predicting ash deposition behaviour for co-combustion of palm kernel with coal based on CFD modelling of particle impaction and sticking. Fuel, 2016; 165: 41-49.

[127] Leppänen A., Tran H., Taipale R., Välimäki E., Oksanen A. Numerical modeling of fine particle and deposit formation in a recovery boiler. Fuel, 2014; 129: 45-53.

[128] Garba M.U., Ingham D.B., Ma L., Porter R.T.J., Pourkashnian M., Tan H.Z., Williams A. Prediction of potassium chloride sulfation and its effect on deposition in biomass-fired boilers. Energy & Fuels, 2012; 26: 6501-6508.

[129] Brink A., Lindberg D., Hupa M., de Tejada M.E., Paneru M., Maier J., Scheffknecht G., Pranzitelli A., Pourkashanian M. A temperature-history based model for the sticking probability of impacting pulverized coal ash particles. Fuel Process Technol, 2016; 141, Part 2: 210-215.

[130] Li B., Brink A., Hupa M. Simplified model for determining local heat flux boundary conditions for slagging wall. Energy & Fuels, 2009; 23: 3418-3422.

[131] Balakrishnan S., Nagarajan R., Karthick K. Mechanistic modeling, numerical simulation and validation of slag-layer growth in a coal-fired boiler. Energy, 2015; 81: 462-470.

[132] Tomeczek J., Wacławiak K. Two-dimensional modelling of deposits formation on platen superheaters in pulverized coal boilers. Fuel, 2009; 88: 1466-1471.

[133] García Pérez M., Vakkilainen E., Hyppänen T. 2D dynamic mesh model for deposit shape prediction in boiler banks of recovery boilers with different tube spacing arrangements. Fuel, 2015; 158: 139-151.

[134] Namkung H., Xu L.-H., Kang T.-J., Kim D.S., Kwon H.-B., Kim H.-T. Prediction of coal fouling using an alternative index under the gasification condition. Applied Energy, 2013; 102: 1246-1255.

[135] Degereji M.U., Ingham D.B., Ma L., Pourkashanian M., Williams A. Numerical assessment of coals/blends slagging potential in pulverized coal boilers. Fuel, 2012; 102: 345-353.

[136] Hatt R.M. Fireside deposits in coal-fired utility boilers. Progress in Energy and Combustion Science, 1990; 16: 235-241.

[137] Su S., Pohl J.H., Holcombe D., Hart J.A. Slagging propensities of blended coals. Fuel, 2001; 80: 1351-1360.

[138] Jak E. Prediction of coal ash fusion temperatures with the F∗A∗C∗T thermodynamic computer package. Fuel, 2002; 81: 1655-1668.

[139] Wigley F., Williamson J., Malmgren A., Riley G. Ash deposition at higher levels of coal replacement by biomass. Fuel Processing Technology, 2007; 88: 1148-1154.

[140] Hutchings I.S., West S.S., Williamson J. An assessment of coal-ash slagging propensity using an entrained flow reactor, in: L. Baxter, R. DeSollar (Eds.) Applications of Advanced Technology to Ash-Related Problems in Boilers, Springer US, 1996, pp. 201-222.

[141] Zhan Z., Bool L.E., Fry A., Fan W., Xu M., Yu D., Wendt J.O.L. Novel Temperature-Controlled Ash Deposition Probe System and Its Application to Oxy-coal Combustion with 50% Inlet O2. Energy & Fuels, 2014; 28: 146-154.

[142] Wang G., Pinto T., Costa M. Investigation on ash deposit formation during the co-firing of coal with agricultural residues in a large-scale laboratory furnace. Fuel, 2014; 117, Part A: 269-277.

[143] Niu Y., Du W., Tan H., Xu W., Liu Y., Xiong Y., Hui S. Further study on biomass ash characteristics at elevated ashing temperatures: The evolution of K, Cl, S and the ash fusion characteristics. Bioresource Technology, 2013; 129: 642-645.

[144] Niu Y., Zhu Y., Tan H., Hui S., Jing Z., Xu W. Investigations on biomass slagging in utility boiler: Criterion numbers and slagging growth mechanisms. Fuel Processing Technology, 2014; 128: 499-508.

[145] Wang X., Xu Z., Wei B., Zhang L., Tan H., Yang T., Mikulčić H., Duić N. The ash deposition mechanism in boilers burning Zhundong coal with high contents of sodium and calcium: A study from ash evaporating to condensing. Applied Thermal Engineering, 2015; 80: 150-159.

[146] Zhou H., Zhou B., Zhang H., Li L., Cen K. Investigation of slagging characteristics in a 300 kW test furnace: Effect of deposition surface temperature. Industrial & Engineering Chemistry Research, 2014; 53: 7233-7246.

[147] Zhou H., Zhou B., Li L., Zhang H. Investigation of the influence of the furnace temperature on slagging deposit characteristics using a digital image technique. Energy & Fuels, 2014; 28: 5756-5765.

[148] Zhou H., Zhou B., Li L., Zhang H. Experimental measurement of the effective thermal conductivity of ash deposit for high sodium coal (zhun dong coal) in a 300 kW test furnace. Energy & Fuels, 2013; 27: 7008-7022.

[149] Zhou H., Zhou B., Dong K., Ding J., Cen K. Research on the slagging characteristics of easy to slagging coal in a pilot scale furnace. Fuel, 2013; 109: 608-615.

[150] Gubba S.R., Ma L., Pourkashanian M., Williams A. Influence of particle shape and internal thermal gradients of biomass particles on pulverised coal/biomass co-fired flames. Fuel Processing Technology, 2011; 92: 2185-2195.

[151] Lu G., Yan Y., Cornwell S., Whitehouse M., Riley G. Impact of co-firing coal and biomass on flame characteristics and stability. Fuel, 2008; 87: 1133-1140.

[152] Smart J.P., O'Nions P., Riley G.S. Radiation and convective heat transfer, and burnout in oxy-coal combustion. Fuel, 2010; 89: 2468-2476.

[153] Lindström E., Sandström M., Boström D., Öhman M. Slagging characteristics during combustion of cereal grains rich in phosphorus. Energy & Fuels, 2007; 21: 710-717.

[154] Grimm A. Experimental studies of ash transformation processes in combustion of phosphorus-rich biomass fuels[D]. Doctoral Thesis, Luleå University of Technology, 2012.

[155] Baptiste F. Numerical and experimental characterization of drop tube furnace and ash deposition analysis [D]. Master Thesis, RWTH Aachen University, 2013.

[156] Xu M., Yu D., Yao H., Liu X., Qiao Y. Coal combustion-generated aerosols: Formation and properties. Proceedings of the Combustion Institute, 2011; 33: 1681-1697.

[157] Wang Y., Tan H., Wang X., Cao R., Wei B. The condensation and thermodynamic characteristics of alkali compound vapors on wall during wheat straw combustion. Fuel, 2017; 187: 33-42.

[158] U.S. Kleinhans, M. Barnerboi, S. Babat, C. Wieland, Spliethoff H. The role of thermophoresis during deposit build-up on a superheater tube[A]. In: M.R. Malayeri, H. Muller-Steinhagen, A.P. Watkinson, Proceedings of international conference on heat exchanger fouling and cleaning[C], Enfield (Dublin), Ireland, 2015; 119-127.

[159] Pike S., Dewison M.G., Spears D.A. Sources of error in low temperature plasma ashing procedures for quantitative mineral analysis of coal ash. Fuel, 1989; 68: 664-668.

[160] Black S., Szuhánszki J., Pranzitelli A., Ma L., Stanger P.J., Ingham D.B., Pourkashanian M. Effects of firing coal and biomass under oxy-fuel conditions in a power plant boiler using CFD modelling. Fuel, 2013; 113: 780-786.

[161] Rubiera F., Pis J.J., Pevida C. Raw materials, selection, preparation and characterization, in: L. Puigjaner (Ed.) Syngas from Waste: Emerging Technologies, Springer London, London, 2011, pp. 11-22.

[162] Akbar S. Numerical simulation of deposit formation in coal-fired utility boilers with biomass co-combustion [D]. Doctoral Thesis, University of Stuttgart, 2011.

[163] Ma L., Pourkashanian M., Williams A., Jones J. A numerical model for predicting biomass particle depositions in a PF furnace[A]. In: ASME Turbo Expo 2006: Power for Land, Sea, and Air[C], 2006; 333-342.

[164] Kær S.K., Rosendahl L.A., Baxter L.L. Extending the capability of cfd codes to assess ash related problems in biomass fired boilers. Prepr. Pap.-Am. Chem. Soc., Div. Fuel Chem, 2004; 49: 97.

[165] Lee F.C.C., Lockwood F.C. Modelling ash deposition in pulverized coal-fired applications. Progress in Energy and Combustion Science, 1999; 25: 117-132.

[166] Ma L., Pourkashanian M., Williams A., Jones J. A numerical model for predicting biomass particle depositions in a pf furnace[A]. In: Proc ASME Turbo Expo 2006[C], Barcelona, Spain, 2006; 333-342.

[167] Mueller C., Skrifvars B.-J., Backman R., Hupa M. Ash deposition prediction in biomass fired fluidised bed boilers ? combination of CFD and advanced fuel analysis. Progress in Computational Fluid Dynamics, an International Journal, 2003; 3: 112-120.

[168] Badzioch S., Hawksley P.G.W. Kinetics of thermal decomposition of pulverized coal particles. Industrial & Engineering Chemistry Process Design and Development, 1970; 9: 521-530.

[169] Backreedy R.I., Fletcher L.M., Ma L., Pourkashanian M., Williams A. Modelling pulverised coal combustion using a detailed coal combustion model. Combustion Science and Technology, 2006; 178: 763-787.

[170] Ma L., Jones J.M., Pourkashanian M., Williams A. Modelling the combustion of pulverized biomass in an industrial combustion test furnace. Fuel, 2007; 86: 1959-1965.

[171] Ma L., Gharebaghi M., Porter R., Pourkashanian M., Jones J.M., Williams A. Modelling methods for co-fired pulverised fuel furnaces. Fuel, 2009; 88: 2448-2454.

[172] Chen L., Ghoniem A.F. Development of a three-dimensional computational slag flow model for coal combustion and gasification. Fuel, 2013; 113: 357-366.

[173] Chen H.C., Patel V.C. Near-wall turbulence models for complex flows including separation. AIAA Journal, 1988; 26: 641-648.

[174] Kader B.A. Temperature and concentration profiles in fully turbulent boundary layers. International Journal of Heat and Mass Transfer, 1981; 24: 1541-1544.

[175] Barker B., Casaday B., Shankara P., Ameri A., Bons J.P. Coal ash deposition on nozzle guide vanes—part ii: Computational modeling. Journal of Turbomachinery, 2012; 135: 011015-011015.

[176] Bouhairie S., Chu V.H. Two-dimensional simulation of unsteady heat transfer from a circular cylinder in crossflow. Journal of Fluid Mechanics, 2007; 570: 177-215.

[177] Fryda L., Sobrino C., Cieplik M., van de Kamp W.L. Study on ash deposition under oxyfuel combustion of coal/biomass blends. Fuel, 2010; 89: 1889-1902.

[178] Bale C.W., Bélisle E., Chartrand P., Decterov S.A., Eriksson G., Hack K., Jung I.H., Kang Y.B., Melançon J., Pelton A.D., Robelin C., Petersen S. FactSage thermochemical software and databases — recent developments. Calphad, 2009; 33: 295-311.

[179] Aho M., Ferrer E. Importance of coal ash composition in protecting the boiler against chlorine deposition during combustion of chlorine-rich biomass. Fuel, 2005; 84: 201-212.

[180] Tortosa Masiá A.A., Buhre B.J.P., Gupta R.P., Wall T.F. Characterising ash of biomass and waste. Fuel Processing Technology, 2007; 88: 1071-1081.

[181] Plaza P., Griffiths A.J., Syred N., Rees-Gralton T. Use of a predictive model for the impact of cofiring coal/biomass blends on slagging and fouling propensity. Energy & Fuels, 2009; 23: 3437-3445.

[182] Tortosa Masiá A.A. Characterisation and prediction of deposits in biomass co-combustion [D]. Doctoral Thesis, Delft University of Technology, 2010.

[183] Zhang L., Ninomiya Y. Transformation of phosphorus during combustion of coal and sewage sludge and its contributions to PM10. Proceedings of the Combustion Institute, 2007; 31: 2847-2854.

[184] Yakaboylu O., Harinck J., Gerton Smit K.G., de Jong W. Supercritical water gasification of manure: A thermodynamic equilibrium modeling approach. Biomass and Bioenergy, 2013; 59: 253-263.

[185] Mao T., Kuhn D.C.S., Tran H. Spread and rebound of liquid droplets upon impact on flat surfaces. AIChE Journal, 1997; 43: 2169-2179.

[186] Zhang Z., Kleinstreuer C., Hyun S. Size-change and deposition of conventional and composite cigarette smoke particles during inhalation in a subject-specific airway model. Journal of Aerosol Science, 2012; 46: 34-52.

[187] Wigley F., Williamson J., Riley G. The effect of mineral additions on coal ash deposition. Fuel Processing Technology, 2007; 88: 1010-1016.

[188] Xu J., Yu D., Fan B., Zeng X., Lv W., Chen J. Characterization of ash particles from co-combustion with a zhundong coal for understanding ash deposition behavior. Energy & Fuels, 2014; 28: 678-684.

[189] Wu X., Zhang X., Yan K., Chen N., Zhang J., Xu X., Dai B., Zhang J., Zhang L. Ash deposition and slagging behavior of Chinese Xinjiang high-alkali coal in 3 MWth pilot-scale combustion test. Fuel, 191: 1191-1202.

[190] Zhou H., Zhou B., Zhang H., Li L. Behavior of fouling deposits formed on a probe with different surface temperatures. Energy & Fuels, 2014; 28: 7701-7711.

[191] Talbot L., Cheng R.K., Schefer R.W., Willis D.R. Thermophoresis of particles in a heated boundary layer. Journal of Fluid Mechanics, 1980; 101: 737-758.

[192] Brink A., Laurén T., Yrjas P., Hupa M., Friesenbichler J. Development and evaluation of a long-term deposit probe for on-line monitoring of deposit growth. Fuel Processing Technology, 2007; 88: 1129-1135.

[193] Robinson A.L., Buckley S.G., Baxter L.L. Experimental measurements of the thermal conductivity of ash deposits: Part 1. Measurement technique. Energy & Fuels, 2001; 15: 66-74.

[194] Jokiniemi J.K., Pyykönen J., Lyyränen J., Mikkanen P., Kauppinen E.I. Modelling ash deposition during the combustion of low grade fuels[A]. In: L. Baxter, R. DeSollar, Applications of Advanced Technology to Ash-Related Problems in Boilers[C], Boston, MA, 1996; 591-615.

[195] Bilirgen H. Slagging in PC boilers and developing mitigation strategies. Fuel, 2014; 115: 618-624.

[196] Sondreal E.A., Tufte P.H., Beckering W. Ash fouling in the combustion of low rank western u.S. Coals. Combustion Science and Technology, 1977; 16: 95-110.

[197] Hurley J.P., Benson S.A. Ash deposition at low temperatures in boilers burning high-calcium coals 1. Problem definition. Energy & Fuels, 1995; 9: 775-781.

[198] Dai B.-Q., Wu X., De Girolamo A., Zhang L. Inhibition of lignite ash slagging and fouling upon the use of a silica-based additive in an industrial pulverised coal-fired boiler. Part 1. Changes on the properties of ash deposits along the furnace. Fuel, 2015; 139: 720-732.

[199] Dai B.-Q., Wu X., De Girolamo A., Cashion J., Zhang L. Inhibition of lignite ash slagging and fouling upon the use of a silica-based additive in an industrial pulverised coal-fired boiler: Part 2. Speciation of iron in ash deposits and separation of magnetite and ferrite. Fuel, 2015; 139: 733-745.

[200] Benson S.A., Hurley J.P., Zygarlicke C.J., Steadman E.N., Erickson T.A. Predicting ash behavior in utility boilers. Energy & Fuels, 1993; 7: 746-754.

[201] Zhang M., Mu H., Li G., Ning Y. Forecasting the transport energy demand based on PLSR method in China. Energy, 2009; 34: 1396-1400.

[202] McLennan A.R., Bryant G.W., Stanmore B.R., Wall T.F. Ash formation mechanisms during pf combustion in reducing conditions. Energy & Fuels, 2000; 14: 150-159.

[203] Wang H. Partial least-squares regression-method and applications, National Defense Industry Press, Beijing, China, 1999.

[204] Abdi H. Partial least square regression (PLS regression). Encyclopedia for research methods for the social sciences, 2003; 792-795.

[205] Seggiani M., Pannocchia G. Prediction of coal ash thermal properties using partial least-squares regression. Industrial & Engineering Chemistry Research, 2003; 42: 4919-4926.

[206] Wold S., Sjöström M., Eriksson L. PLS-regression: a basic tool of chemometrics. Chemometrics and Intelligent Laboratory Systems, 2001; 58: 109-130.

[207] Wen X. Predicting the regularity of the fouling characteristics of heat exchanger equipments[D]. Doctoral Thesis, North China Electric Power University, 2013.

[208] Lorber A., Wangen L.E., Kowalski B.R. A theoretical foundation for the PLS algorithm. Journal of Chemometrics, 1987; 1: 19-31.

[209] Song W.J., Tang L.H., Zhu X.D., Wu Y.Q., Zhu Z.B., Koyama S. Effect of coal ash composition on ash fusion temperatures. Energy & Fuels, 2010; 24: 182-189.

[210] Niu Y., Zhu Y., Tan H., Wang X., Hui S.e., Du W. Experimental study on the coexistent dual slagging in biomass-fired furnaces: Alkali- and silicate melt-induced slagging. Proceedings of the Combustion Institute, 2015; 35: 2405-2413.

[211] Li Q.H., Zhang Y.G., Meng A.H., Li L., Li G.X. Study on ash fusion temperature using original and simulated biomass ashes. Fuel Processing Technology, 2013; 107: 107-112.

[212] Liu B., He Q., Jiang Z., Xu R., Hu B. Relationship between coal ash composition and ash fusion temperatures. Fuel, 2013; 105: 293-300.

[213] Jensen J.R., Nielsen L.B., Schultz-Møller C., Wedel S., Livbjerg H. The nucleation of aerosols in flue gases with a high content of alkali - a laboratory study. Aerosol Science and Technology, 2000; 33: 490-509.

[214] Ewing C.T., Stern K.H. Equilibrium vaporization rates and vapor pressures of solid and liquid sodium chloride, potassium chloride, potassium bromide, cesium iodide, and lithium fluoride. The Journal of Physical Chemistry, 1974; 78: 1998-2005.

[215] Mills K.C., Keene B.J. Physical properties of BOS slags. International Materials Reviews, 1987; 32: 1-120.